UNIVERSITY OF CALIFORNIA

SANTA CRUZ

PREPARATION OF AMPHIPHILIC JANUS NANOPARTICLES IN STUDYING THEIR UNIQUE CHIROPTICAL PROPERTIES AND ENANTIOMERIC SELECTIVITY

A dissertation submitted in partial satisfaction

of the requirements for the degree of

DOCTOR OF PHILOSOPHY

in

CHEMISTRY

by

Jia Lu

September 2019

The dissertation of Jia Lu

is approved:

_____

Professor Shaowei Chen, Chair

_____

Professor Ilan Benjamin

_____

Professor Yat Li

_____

Quentin Williams

Vice Provost and Dean of Graduate Studies

Table of Contents

LIST OF FIGURES

Chapter 2

Chapter 3

Figure 3.7. CD absorption spectra of D-Cys, L-Cys, and D,L-Cys at varied concentrations in water. The bottom panel is the zoom in of the data highlighted by the dark red box in the top panel within the range of 200 to 250 nm.

Figure 3.8. (top panel) CD spectra of cysteine aqueous solutions at the concentration of 10 mM but at different enantiomeric excess. Dark green curve is the spectrum for the cysteine solution (10 mM) after ligand exchange with JNPC6-MPD in $CHCl_3$ (1 mg/mL) for 24 h at equal volume (Figure 3.1). (bottom panel) Variation of the corresponding CD intensity at 206 nm with the percent excess of L-Cys. Circle symbols are data for the standard solutions, and dark green star is for the cysteine solution after ligand exchange with JNPC6-MPD in $CHCl_3$ for 24 h where the L-Cys excess is estimated to be ca. 10.2%.

Figure 3.9. TGA curve of AuC6 nanoparticles. The C6 ligand content is estimated to be 9.4 wt%. In conjunction with results from the ^1H NMR measurements (Figure 3.1), the amount of D-Cys incorporated onto the nanoparticle surface after ligand exchange reaction for 24 h accounts for about 6.7% of cysteine in the original racemic mixture of D,L-cysteine in water.

Chapter 4

Figure 4.1. TEM images and diameter distributions for (a) AuC6 and (b) AuPEG nanoparticles.

Chapter 5

LIST OF TABLES

Chapter 3

PREPARATION OF AMPHIPHILIC JANUS NANOPARTICLES IN STUDYING THEIR UNIQUE CHIROPTICAL PROPERTIES AND ENANTIOMERIC SELECTIVITY

Jia Lu

ABSTRACT

Janus nanoparticles have been an interesting topic due to their dual functionality by the segregation of surface ligands, whereas chiral nanostructures have been attracting extensive interest in recent years primarily because of the unique materials properties that can be exploited for diverse applications. My research focus was based on chirality originated from the structural asymmetry of Janus nanoparticles and study the enantiomeric selectivity of these nanoparticles.

Gold Janus nanoparticles functionalized with hexanethiolates and 3-mercapto-1,2-propanediol segregated on the two hemispheres, self-assembled into vesicle-like, hollow nanostructures in both water or organic media, and exhibited apparent plasmonic circular dichroism (PCD) absorption in the visible range. The PCD signals were found to become intensified with increasing coverage of the 3-mercapto-1,2-propanediol ligands on the nanoparticle surface, which was attributed to the dipolar property of the structurally asymmetrical Janus nanoparticles. Theoretical simulations based on first principles calculations showed that when the nanoparticle dipoles self-assembled onto the surface of a hollow sphere, a vertex was formed which gave rise to

the unique chiral characteristics. The resulting chiral nanoparticle vesicles could be exploited for the separation of optical enantiomers, as manifested in the selective identification and separation of D-alanine from the L-isomer.

The enantiomeric selectivity of Janus nanoparticles protected by hexanethiolates and 3-mercapto-1,2-propanediol was further studied using D,L-cysteine as the molecular probe. Experimental results demonstrate that D-cysteine was the preferred enantiomers entrapped within the nanoparticle emulsions, where the ensuing ligand exchange reaction was initially confined to the hydrophilic face of the Janus nanoparticles. This suggests that with a deliberate control of the reaction time, chiral Janus nanoparticles could be readily prepared by ligand exchange reactions even with a racemic mixture of ligands.

In a different study, gold Janus nanoparticles functionalized with poly(ethylene glycol) (PEG) ligands hexanethiolates was synthesized. Due to specific interaction of PEG with alkali metal ions, the Janus nanoparticles exhibited marked conformational changes forming organized ensembles in the presence of Na^+ and K^+, as manifested in dynamic light scattering, UV-vis absorption and TEM measurements, whereas no apparent variation was observed with bulk-exchange nanoparticles where the two types of capping ligands were homogeneously mixed on the nanoparticle surface or nanoparticles capped with the PEG ligands alone. The ion complexation was further probed in NMR measurements. Results from this study indicate that select doping of alkali metal ions into PEG-functionalized nanoparticles may be used for controlled assembly of the Janus nanoparticles.

In addition to Janus nanoparticles with segregated ligands, Janus $Cu_{1.75}S$-Au nanostructure was synthesized using Langmuir-Blodgett method at room temperature through ion exchange of gold atoms onto $Cu_{1.75}S$ nanoparticles. Positive chiroptical response arose around 600 nm closed to gold SPR absorption region, whereas the $Cu_{1.75}S$ nanoparticles shown no chiroptical response. Upon etching away the $Cu_{1.75}S$, the deposited gold nanostructure shown weak positive chiroptical response at the same region, indicating chiral origin was due to the asymmetric deposition of gold atoms. In addition, the chiroptical signal of asymmetric gold nanostructure was enhanced upon the formation of $Cu_{1.75}S$-Au hybrid nanostructure.

DEDICATION

Dedicated

To

My Family

ACKNOWLEDGEMENTS

I would like to thank my graduate advisor, Professor Shaowei Chen, for his patience and guidance throughout my Ph. D. career. During the past six years working in Professor Chen's laboratory, I learned plenty of experimental and characterization techniques, as well as data analysis and scientific writing skills. Professor Chen is such a knowledgeable chemist that I really benefitted greatly from his guidance and suggestions for being in the field of material science. Without his support, I would not be able to finish my research projects on time. More importantly, Professor Chen gave me good advice for my future career.

I would also like to thank Professor Ilan Benjamin and Professor Yat Li for serving as my dissertation committees and offer guidance on my research. I would also like to express my appreciation to Professor Jin Zhang for his help and advice for the past six years. I want to say thank you to Professor Chad Saltikov for being my committee member in my third-year qualifying exam.

In addition, I would like to give special thanks to my colleagues for their help on my research:

Dr. Yang Song and Dr. Limei Chen for teaching me how to use the Langmuir-Blodgett trough for the synthesis of Janus nanoparticle and operate the atomic force microscope (AFM) for the characterization of nanoparticle size.

Dr. Chris Deming for his patience in teaching me how to operate the X-ray photoelectron spectroscope (XPS) and transmission electron microscope (TEM), as well as the data analysis.

Dr. Yi Peng for his artistical help on the graphics.

Dr. Eefei Chen for her guidance and advices on taking circular dichroism (CD) measurements and data analysis.

Dr. Hsiau-Wei Lee, for his help with nuclear magnetic resonance (NMR) measurements.

Mr. Jesse Hauser for running the X-ray diffraction (XRD) measurements.

Ms Longbo Li for her help in synthesizing organic ligands.

Mr. Chengyu Song at the National Center for Electron Microscopy (NCEM) in Lawrence Berkeley National Laboratory (LBNL) for his generous help and technical support in operating the TEM microscope and TEM imaging.

Dr. Virginia Altoe at the Molecular Foundry in LBNL for her help and technical support in operating the XPS spectrometer.

I want to thank my labmates, Dr. Ke Liu, Dr. Bruce Phebus, Dr. Peiguang Hu, Dr. Mauricio Rojas-Andrade, Dr. Samantha Sweeney, Mr. David Ricci, Mr. John Diniz, Mr. Bingzhang Lu, Mr. Rene Mercado, Mr. Gustavo Chata, Mr. Forrest Nichols, Mr. Qiming Liu, Prof. Yan Guo, Prof. Xiaohua Fan, Prof. Fanli Lu, Prof. Tizhuang Wang, Prof. Yinghui Ren, Prof. Fen Ran, Dr. Xiaoqing Niu, Prof. Weihua Yang, Prof.

Guoxing Zhu, Prof. Yuanjun Liu, Prof. Junli Liu, Prof. Xiufang Wang, Prof. Yueming Tan, Dr. Wenfang Deng, Dr. Zenghui Qiu, Prof. Lin Guo, Prof. Dangge Gao, Prof. Qiuping Zhao, Prof. Cheng Peng, Dr. Wei Yang, Prof. Ahmad Shaabani, Dr. Wenli Wei, Prof. Yuchuan Zheng, Prof. Lizhuang Chen, Prof. Chenzhong Yao, Prof. Qiaoxia Li, Prof. Wen Yuan, Prof. Yulin Zhang, Dr. Yongtao Tan, Ms. Siraprapha Deebansok, Ms. Ting He, and Ms. Carolin Wahl, for their helpful discussions and companies.

In addition, I want to thank friends from the neighboring labs: Dr. Hanyu Wang, Dr. Yi Yang, Dr. Tianyu Liu, Mr. Tianyi Kou, Mr. Bin Yao, Mr. Shanwen Wang, Mr. Mingpeng Chen, Mr. Dun Lin, Dr. Teng Zhai, Ms. Huarong Peng from the Li Lab; Prof. Binbin Luo, Dr. Staci Adams, Dr. Sarah Lindley, Ms. Sara Bonabi, Mr. Evan Vickers, Mr. A'Lester Allen, Ms. Ke Xu, and Mr. Longshi Rao from the Zhang Lab; Dr. Vicent Duong, Dr. Michael Roders, Dr. Carmen Segura, Dr. Will Hollingsworth from the Ayzner lab; Dr. Chie Funatogawa and Ms Pamela Schleissner from the Kliger lab; Dr. Chad Higa from the Braslau lab; Dr. Eaindar Soe, Dr. Ian Colinas, Dr. Susan Citrak, Ms Ana Kareh from the Oliver lab; Dr. Indranil Chakraborty, Dr. Jorge Jimenez, Mr. Miguel Pinto from the Mascharak lab.

I would like to give special thanks to my undergraduate advisors Professor Daniel Straus and Professor Roger Terrill for them showing me how interesting chemistry can be, which motivated me for pursuing a doctoral degree in Chemistry. Aside from the research, they also give me great suggestions for both career and life.

At last but not the least, I would like to thank my friends and family who are always by my side. I would like to give a special thanks for my friend, Francesca Limanto, for her and her roommates provided me place to rest whenever I go to LBNL for analysis. I also would like to give my special thanks to my parents, uncles and aunts, and my cousins, for their understanding, supports and encouragements throughout my Ph. D. career.

The text of this dissertation includes reprints from the following previously published materials:

Chapter 2: Jia En Lu, Chou-Hsun Yang, Haobin Wang, ChiYung Yam, Zhi-Gang Yu and Shaowei Chen, "Plasmonic circular dichroism of vesicle-like nanostructures by template-less self-assembly of achiral Janus nanoparticles", *Nanoscale*, 2018, *398*, 201.

Chapter 3: Jia En Lu, Yi Peng and Shaowei Chen, "Janus Nanoparticle Emulsions as Chiral Nanoreactors for Enantiomerically Selective Ligand Exchange", *Part. Part. Sys. Char.*, 2019, 1800564.

Chapter 1

Introduction

1.1 Noble Metal Nanoparticles and their Optical Properties

Noble metal nanoparticles have been studied extensively due to their unique optical and catalytical properties in comparison to the bulk form [1,2]. In typical, their unique optical properties can be applied to applications such as biopharmaceutics, electronics and sensing [3-5]. Under light radiation, the conduction band electron on metal nanoparticle surface oscillate under resonant conditions, resulting in a surface charge distribution. The oscillation frequency of electron cloud is characterized by the restoring forces between positive and negative charges through Coulombic attraction, which is also known as surface plasmon resonance (SPR). For spherical metal nanoparticles with a diameter much smaller (~10-100nm) than the wavelength of incident light, the absorption cross-section of nanoparticle can be calculated as [6]

$$C_{abs}(\lambda) = \frac{18\pi f \varepsilon_m^{3/2}}{\lambda} \frac{\varepsilon_2}{(2\varepsilon_m+\varepsilon_1)^2+\varepsilon_2^2} \quad (1)$$

where *f* is the volume-filling fraction of metal, ε_m is the surrounding medium dielectric constant, and ε_1 (real) and ε_2 (imaginary) are the complex dielectric constant of nanoparticle. For nanoparticles with small ε_2, the absorption coefficient is at maximum when $\varepsilon_1 = -2\varepsilon_m$. Due to their strong SPR absorption of noble metal nanoparticles in the visible region (e.g. 400 nm for Ag and 520 nm for Au) [7], the presence of noble metal nanoparticles can readily be detected by UV-vis measurements.

In addition, depending on the size and shape of nanoparticles, the SPR absorption can be easily tuned [8,9]. In classical approaches, the resonance of a metal nanoparticle with

a small diameter in comparison to the wavelength of light, its dielectric function can be predicted as

$$\varepsilon = \varepsilon_m \left(1 - \frac{1}{L_j}\right) \quad (2)$$

where ε_m is the dielectric function of the surrounding medium and L_j is the geometrical depolarization factor along axis j. For non-spherical nanoparticles with $L_1 = L_2 < L_3$, a second absorption peak arose due to the different oscillations along and perpendicular to the long axis of nanoparticle, which induces the splitting dipole resonances into longitudinal and transverse absorption modes. As the aspect ratio of the prepared nanoparticles increases, the longitudinal resonance absorption red shifts (towards the longer wavelength). For example, there are three different plasmonic modes (e.g. dipolar, quadrupolar and sextupolar) can be excited for a gold nanorod (l = 500 nm and d = 40 nm) upon interaction with different wavelength (e.g. 2060 nm, 1030 nm and 734 nm, respectively) of light [10].

In addition to varying the size and shape of a nanoparticle for tuning its SPR absorption, the SPR absorption of a nanoparticle can also be tuned by having multiple components within a nanoparticle, such as the formation of alloy [11-14] and core-shell structures [15-17]. In general, the SPR absorption of an alloy nanoparticle shifts between the SPR absorption of the two components. For example, gold and silver alloy nanoparticles have been studied extensively due to their spontaneous formation of alloy / core-shell structures and their strong SPR absorption in the visible range, and it is found that the

SPR of the alloy nanoparticle shifts between 400 nm (Ag SPR absorption) and 520 nm (Au SPR absorption, depending on the composition of gold and silver component [11-13].

In forming an uniform core-shell nanostructure, there are three general criteria [18]: a) the atomic radius of the core element is larger or equal to the shell element, b) the bond dissociation energy $E_{core\text{-}core}$ is higher than $E_{shell\text{-}shell}$, and c) the Paulings electronegativity of the core is higher than the shell. For example, the adsorption of metal ion also depends on the lattice spacing of each element [18,19]. Habas and co-workers [19] found 4.08% lattice-mismatch occurs at the Au-Pt interface and 0.7% lattice mismatch at the Pd-Pt interface, which led to anisotropic growth of Pt@Au (core@shell) nanostructures. Thus, Fan and co-workers [18] concluded that the formation of Au@Ag and Au@Pd followed the Frank-van der Merwe (layer-by-layer) growth mechanism, while the formation of Au@Pt followed the Volmer-Weber (colonies) growth mechanism.

In addition, the deposition of atom can be affected by the injection rate and concentration of different ingredients. In general, silver ions deposit preferably on gold {100} facet without the presence of surface ligands [20]. At the early stage of deposition, $AgNO_3$ forms double layer around Au seed, with positive Ag^+ cations and NO_3^- anions. With low ascorbic acid concentration with slow addition rate, the growth of Ag layer propagates towards the solution on top of the deposited Ag surface. After the deposition of the first atom, the Au surface becomes positively charged and attracts the double layer closer to the Au surface, which inhibits the nucleation of Ag on other Au {100} facets. In contrast, while injecting ascorbic acid rapidly, the pH of solution was

decreased rapidly, which enables simultaneous Ag nucleation at multiple sites on Au seed surface. Thus, with fast injection of ascorbic acid at low concentration, the Ag grows in colonies on the {100} facets, while a homogenous shell formed with fast injection of ascorbic acid solution at high concentration.

Interestingly, the morphology and facet of nanoparticles can also be tuned using surface ligands, such as cetyltrimethylammonium bromide (CTAB) [21,22]. In typical, the presence of CTAB slows down the reduction speed of gold ion by forming gold-CTAB complex [22], thus the resulting $AuRu_3$ alloy will have an hcp structure while the alloy forms an fcc structure in the absence of CTAB. In addition, the presence of surface ligand can also affect the facets [23,24] and surface morphology of core-shell nanoparticles [21], since the shell growth depends on both the atomic deposition rate and the surface diffusion rate. When the surface diffusion rate is higher than the atomic deposition, the deposited atoms re-orientate and form uniform shell layers [21]. In contrast, when the atomic deposition rate is faster than the surface diffusion, the shell has a higher growth rate at the deposition site forming structures with pointy sharp corners [25,26]. This type of nanoparticles is often referred to as high index facets nanoparticles [27-29], which shown unique optical properties, such as SPR "hot-spot" at the tip of nanoparticles [30].

In addition to hot-spot generation by pointy corners on nanoparticle surfaces, SPR hot-spots can be generated by directed assembly of individual nanoparticles. Some of the common methods for directing nanoparticles assembly are the employment of an external electromagnetic field or light irradiation. For example, magnetic nanoparticles are useful in water purification because they are easy to be collected by applying an

external magnetic field after interacting with the pollutant of interest [31,32]. Furthermore, the directed assembly of metal nanoparticles can also be achieved by nanoparticle surface functionalization with different ligands [33]. For example, one of the common ways for directing nanoparticles assembly is to functionalize two batches of nanoparticles, one with donor molecules and the other with receptor molecules, for light-triggered cross-coupling reactions upon laser irradiation [34].

While directed nanoparticle assembly often involves the change of chemical state (e.g. conformation and / or chemical bonding) of surface ligands in responding to the environment change, self-assembly of nanoparticles is mainly governed by the chemical interactions between ligands with solvent medium or ligands on the neighboring nanoparticles. One of the simple ways to self-assemble metal nanoparticles is done by solvent evaporation. In typical, the nanoparticle solution is first deposited on a substrate surface; followed by solvent evaporation, the nanoparticles will self-assemble into a monolayer film after evaporation of solvent [35,36]. For example, Yi and co-workers also found that gold nanoparticles protected by amphiphilic block copolymers (e.g. polystyrene and polyethylene oxide) self-ensembled into hollow vesicles upon dehydration [36], where the morphology of resulting structure depended upon the root-mean-square end-to-end distance of polystyrene block to the diameter of the gold nanoparticles. After the formation of a monolayer film, the SPR absorption of the resulting monolayer redshifts in comparison to individual nanoparticles, indicating coupling between neighboring nanoparticles [37].

In typical, the coupling of neighboring nanoparticles occurs when the center-to-center interparticle distance is smaller than five times of the nanoparticle radius and causing a splitting of the original nanoparticle resonance [38], and the SPR absorption can be red-shifted by up to 300 nm in comparison to the individual nanoparticles. In addition, the redshift of SPR absorption can be controlled by the chain length and conformation of surface ligands [39], which longer and more stretched chain length give rises to longer interparticle distance and resulting in weaker SPR coupling.

One other common way to self-assemble metal nanoparticles is by the synthesis of amphiphilic Janus nanoparticles, which will be discussed in detail in the next section. In spontaneous formation of superstructure within a solvent system with mixed solvent polarity, the self-assembled structure of this type of nanoparticle show high tunability and stability, which is highly suitable for applications such as biosensing and drug delivery.

1.2 Janus Nanoparticles: Preparation and Self-assembly

Among the different types of nanoparticles, Janus nanoparticles (JNPs) refers to nanoparticles composed of two different components on the opposite side of the nanostructure. JNPs inherit their names from the Romans God Janus, which refers to nanoparticles that are composed of either different surface ligands or different material on opposite hemisphere of the same nanoparticle [40,41]. The resulting bifunctional Janus nanoparticles have shown unique chemical [42] and optical [43,44] properties.

One simple and inexpensive way to synthesize JNPs in large quantity is through the adsorption of nanoparticles onto wax surface at the liquid-liquid interface of water and wax [45-47]. In typical, the as-prepared hydrophobic nanoparticles are first dissolved in hot wax and mixed with hot water under stirring. As the mixture is cooled down, the hydrophobic nanoparticles will then adsorb onto the solidified was surface at the liquid-liquid interface of molten wax and water. The large particulates of solidified wax with nanoparticles are then filtered from the mixture and re-dispersed into a different solvent for nanoparticle functionalization at the wax-solvent interface. After the functionalization, the resulting JNPs are desorbed from the wax surface in chloroform. This method can produce JNP in a simple fashion with large quantity, while the only limitation for this method is that it can only be applied to relatively large nanoparticles [45].

Similar to the emulsion method using wax and water, JNPs can be prepared using the masking technique by covering part of the nanoparticle by a thin polymer film [48]. In this method, a monolayer of nanoparticles will first be deposit onto a flat substrate, followed by the deposition of a thin polymer layer (e.g., PMMA) by spin casting. Part of the polymer layer will then be removed to expose part of the nanoparticle surface for functionalization. Finally, the resulting JNPs can be released by the removal of polymer film. Even though this method involves more steps, it enables the functionalization of JNPs with ligands that are similar in their chemical and physical properties (e.g. hydrophilicity). In addition, this method is often used for the functionalization with polymers onto nanoparticle surfaces. When functionalizing

nanoparticles with long chain polymers, the methods are usually referred to as "grafting from" and "grafting to" methods [49-51]. By definition, the "grafting from" method starts with the attachment of a monomer initiator followed by the growth of a polymer chain on the nanoparticle surface, while the "grafting to" method refers to the attachment of the as-prepared long chain polymer. Grafting from gives higher polymer density while grafting to gives more uniform distribution of polymer since the polymer is pre-modified before attached onto nanoparticles [51].

The grafting density of gold nanoparticle-poly(ethylene glycol) conjugates can be measured by techniques such as thermogravimetric analysis (TGA), analytical ultracentrifugation analysis (AUC) and total organic carbon analysis (TOC). While TGA measures the weight difference before and after ligand decomposition, AUC measures the change in density induced by polymer ligands in comparison with the highly dense gold core, and the TOC measures the non-purgeable organic carbon concentration in ppm (mg/L). The mathematical representation for each technique can be calculated as [52]

$$\sigma_{TGA} = \frac{\left(\left(\frac{wt\%_{shell}}{wt\%_{core}}\right)\rho_{core}\frac{4}{3}\pi r_{core}^3 N_A\right)}{MW 4\pi r_{core}^2} \quad (3)$$

$$\sigma_{AUC} = \frac{m_{shell}}{MW 4\pi r_{core}^2 N_A} \quad (4)$$

$$\sigma_{TOC} = \frac{[C]}{2n[NP]4\pi r_{core}^2} \quad (5)$$

where the gold core density (ρ_{core}) is 19.6 g/cm^3, N_A is the Avogadro's number, [C] is the non-purgeable organic carbon concentration and [53] is the nanoparticle concentration in solution.

One other common way for preparing amphiphilic JNP is by interfacial ligand exchange on a Langmuir-Blodgett trough [54]. In typical, the hydrophobic nanoparticles in organic solution are first deposited on a water subsurface, then a mechanical pressure will be applied after the evaporation of organic solvent until the interparticle distance is about 1 – 2 extended ligand length. Finally, the interfacial ligand exchange will happen at the water-air interface after the injection of a hydrophilic ligand. After the ligand exchange reaction, the functionalized JNPs will be collected and re-disperse in a solvent of interest.

Recently, new methods such as in-situ photo-simulation [55] and nanoparticle welding [56] have been developed for the preparation of asymmetric JNPs. For example, Kossak and coworkers reported a solution phase synthesis of anisotropic and multicomponent nanostructures through in-situ photo-simulation and reduction of metal-halide intermediates [55]. In addition, Huang and coworkers reported a welding-induced one pot room temperature synthesis of asymmetric Janus Au-Ag2S nanoparticles first through electrostatic attraction of ligands to bring nanoparticles close to each other, followed by the desorption of surface ligand (e.g. (2,2,6,6-tetramethylpiperidin-1-yl)oxyl, also known as TEMPO) [56].

Upon functionalizing JNP with different components, they can be used in applications such as cancer therapy, catalysis and sensing. For example, when JNP is functionalized with surface ligands with different polarity, the permeability of JNP passing through membranes can be changed [5], thus selectively targeting different organs and / or tumor sites [57,58]. In addition, when depositing catalysts on one hemisphere of JNP, it can give rise to active motion of JNP in response to the local concentration change of chemical environment by having catalytic reaction on one side on the nanoparticle [42], which is also known as "chemical nanomotors" [59,60]. The catalytic reaction can be irradiated by either UV [61] or near infrared (NIR) [62] light depending on the structural morphology, and with or without the presence of a fuel source (e.g., H_2O_2) [61]. Among different types of metals, precious metal ions show high activity ($Pt^{2+} > Ag^{+} > Pd^{2+} > Au^{3+}$) with H_2O_2 in comparison to magnesium [63]. In addition, the direction of catalytic JNP movement was shown highly directed by self-thermophoresis from the catalytic activity guiding the nanoparticle to travel in the direction of the chemically inert side, in comparison to nanoparticles that are fully protected by catalyst move in random direction by Brownian motion [64].

In contrast to individual JNPs, unique chemical and optical properties can also arise from self-assembly of JNP into superstructures [65-67]. Among different types of Janus nanoparticles, amphiphilic Janus nanoparticles were studied extensively due to their self-assembly property, which can be used in drug delivery [68], phase transfer catalysis [65] and sensing [43] applications. In addition, studies also showed that the self-assembly structure of JNP can be tuned by the structural geometry, solution type, pH, temperature

and JNP concentration [69]. For example, upon synthesizing JNP composed of poly(tert-butyl acrylate) and poly(3-(triethoxysilyl)propyl methacrylate) with different ratio [70], researchers found that JNPs with larger size difference between the two hemisphere result in smaller self-assembly structure with higher curvature, whereas JNPs with smaller size difference between the two hemisphere tend to form larger multi-layer structures.

The self-assembly of Janus nanoparticles can be directed by applying an external magnetic field [35,71-73], changing of solvent system [74] and temperature, tuning the nanoparticle amphiphilicity and concentration and size, etc. Among different self-assembled structures, hollow-micelle-like structures were studied extensively, due to their reversibility of capturing and releasing the molecule of interest within the assembled structure in different solvent systems [74]. Recently, studies have also shown that JNP protected by achiral ligands self-assembly into micelle-like structures give rise to chiroptical response, which results in high enantiomeric selectivity [66,67]. In comparison to nanoparticles with chiral components, the study of chirality of achiral nanoparticles self-assembly is more attractive, since it does not require an enantiomerically pure starting material or chiral template. In addition, the chiroptical response can be tuned by the resulting structure built.

1.3 Chiral nanoparticles and their Origin of Chirality

Among different areas in studying noble metal nanoparticles, the study of chiral metal nanoparticles is interesting due to its high enantiomeric selectivity in catalysis and sensing [75,76]. In addition, chiral molecules are important biological building blocks (e.g. DNA, RNA and peptides), the high enantiomeric selectivity of chiral nanoparticles can play an important role in biopharmaceutics [76].

The chirality of plasmonic nanostructure was first observed upon the interaction between gold nanoclusters and glutathione molecules [77], which was attributed to the delocalization of conduction band electrons of intrinsically chiral small gold cluster (4-8kDa, <40 Au atoms) structures. DFT calculations further supports that the strong interaction between metal nanoclusters and thiolate ligands (e.g. SCH_3) can influence the surface electronic properties and even distortion of cluster geometry, thus resulting in either enhanced intrinsic chirality (e.g. Au_{28} and Au_{55}) [78] or induced chirality by dramatic geometry distortion of achiral gold cluster (e.g. Au_{38}) [79-82].

In general, the interaction between light and material can be described in terms of refractive index and extinction coefficient of the material. Refractive index of a material is a measure of the reduction of light speed when passing through the material in comparison to the speed of light in vacuum, where the extinction coefficient measures the amount of electromagnetic radiation such material scatters and absorbs which affects the amplitude of the electric field of light [83].

In studying the optical property of chiral structures, the circularly polarized incident light (CPL) is usually used instead of linearly polarized light. Upon the interaction with achiral structures, the change in velocity (refractive index) and amplitude (extinction coefficient) of light is the same for left and right CPL due to structural symmetry. However, when incident light passes through a chiral structure over time, the change in velocity and / or amplitude of L- and R-CPL are / is different, depending on the morphology of material. When the incident light interacts differently with a material's refractive index, the polarization vector of L- and R-CPL rotates to different position over time, thus it gives rise to optical rotation which is also known as optical rotatory dispersion (ORD). The angle between this new vector position and its original position, ϕ, can be expressed as:

$$\phi = \frac{\pi(n^{+} - n^{-})l}{\lambda} \tag{3}$$

where l is the path length of the material, and λ is the wavelength of light. Depending on which of the two CPL is absorbed stronger at a specific wavelength, the CD absorption band can lead to a positive or negative response. In general, chiral material with difference in refractive index leads to weak chiroptical effects (10^{-6}).

On the other hand, if the interaction between incident light and material alters the change in the amplitude of incident light electric field, the CPL becomes ellipsely polarized and gives rise to circular dichroism (CD). The ellipticity of a material can be measured as

$$\epsilon = \frac{|\sigma^+| - |\sigma^-|}{|\sigma^+| + |\sigma^-|} \quad (4)$$

And

$$\epsilon = \frac{(A^- + A^+) ln10}{4} \quad (5)$$

where A^- and A^+ are the amplitudes of R-CPL and L-CPL. The magnitude of chiroptical effects originates from extinction coefficient are typically about 0.1% in organic molecules.

Depending on the type of materials, the optical rotation can either be positive (rotating to the right) or negative (rotating to the left). The variation of the absolute amplitude of the optical rotation of a given material as a function of incident light wavelength can be defined as Cotton effect. If the amplitude of optical rotation for a material is positive at longer wavelength and negative at shorter wavelength, the material possesses a positive Cotton effect and gives rise to positive CD signal. If the amplitude of optical rotation of a material is negative at longer wavelength and positive at shorter wavelength, the material possesses a negative Cotton effect and gives rise to negative CD signal. The direction and angle of the optical rotation are dependent of the incident light wavelength.

In organic molecules, chiroptical effects can arise from either intrinsic effect (chiral center) or secondary chiral effect (e.g. protein or DNA folding) upon inter- and intra-molecular interactions. For plasmonic metal nanoparticles, the origin of chirality can be divided into four categories [75]:

i. Intrinsic chirality arose from asymmetric inorganic core shape (e.g. helical structure)

ii. Intrinsic chirality arose from asymmetries of inorganic core surface (e.g. chiral ligand)

iii. Extrinsic chirality of individual particle due to its chiral stabilizer shell (e.g. chiral molecules in close position with particle)

iv. Extrinsic chirality arose from chiral field effect due to the material's high polarizability (e.g. chiral assembly)

Upon interaction with CPL, the electron cloud around a spherical nanoparticle turns into a spiral, which gives rise to an electric current on the nanoparticle surface as the propagating electric field of light pushes away the charge [84]. This resulting helical electric current can be referred to as a counter-propagating "plasmonic helix". Since spherical nanoparticles are achiral, the plasmonic helix generated upon interaction with L-CPL and R-CPL will be equal amplitude with opposite sign, and thus cancels out with each other. For nanoparticles with asymmetric core geometry, the retardation effect of electron cloud on nanoparticle surface is different in different directions, which results in different interaction (e.g. hindered or favored) with L- and R-CPL [85-89]. In specific, upon interaction between CPL and helical coil, CPL with the same handedness as the helical coil was blocked when propagating along the helix axis, which CPL with opposite handedness was transmitted [90].

In preparation of nanostructures with intrinsic chirality (e.g. chiral metal core), a chiral template or enantiomerically pure chiral molecule is often used, where the chirality of resulting nanostructure is inherited from the chiral template or molecule used [91-95]. Recently, Lee and coworkers [95] reported that the relative location of the amine group with respect to the thiol group on a cysteine molecule was the determining factor for synthesizing a chiral helicoid nanostructure by studying the growth mechanism using HR-TEM. In typical, the relative position of amine and thiol group on L-cysteine results in a preferential interaction with the {321} planes in the R regions, thus blocking the growth in the vertical direction on the R regions and leading to a R-S boundary shift to the S region with asymmetric overgrowth [96-98]. The resulting nanoparticle with chiral surface morphology exhibit high enantiomeric selectivity due to binding preference by chiral molecules, which can lead to potential application such as enantiomeric selective catalysis [91-93].

Aside from intrinsically chiral nanostructures, chirality of nanostructures can be induced by the presence of chiral organic molecules in close contact ($r \ll \lambda$) [99-101]. For CD signal of chiral molecules that is enhanced by plasmonic material with $\lambda_{plasmon} < \lambda_{mol}$ (e.g. Al), the plasmon-induced CD band will be negative and strongest when $\mu_{12} \parallel \hat{z}$ (normal dipole orientation) and positive with relative weak signal when $\mu_{12} \perp \hat{z}$, while CD band will be opposite for material possess $\lambda_{plasmon} > \lambda_{mol}$ (e.g. Au and Ag) [101].

In addition, depending on the concentration and arrangement of the chiral molecule that is adsorbed on the plasmonic molecule surface, the chiroptical response of the hybrid system can be different [92,102-107]. At low molecule concentration, the chiroptical signal is dominated by the energy dissipation within the nanoparticle and give rise to CD response at the SPR region of the nanoparticle, while CD response is dominated by the ORD response from the chiral molecule and give rise to enhanced CD signal of the chiral molecule at its absorption region at high molecule concentration [103]. At an intermediate adsorbed molecule concentration, CD spectrum shows a combination of signals. The chiroptical signal enhancement effect by plasmonic nanostructures enables the detection of chiral molecules at a much lower concentration [105,108,109].

Since chirality is a macroscopic phenomenon that describes the optical response of a system, the chiroptical response can be arose by the assembly of a collection of achiral nanoparticles [110-115]. The achiral nano-building blocks within the ensemble can be composed of either different material [114] or same material with different size [113] and shape [112]. For identical achiral nano-building blocks, chiroptical response can be arose when they are assembled into a chiral superstructure [110,111,115]. Upon the assembly of two identical C-shape nanostructures (< 500nm) [111], near field CD response was shown when the interparticle distance is < 350nm, which the chiroptical response was attributed to the positive maximum signal arose upon the merging of two C-shape nanostructures in the center of the S-shape structure with two negative signals at each end of the structure. In addition, identical nanoparticles can also be linked together

through chiral linkers (e.g. DNA and peptide), forming chiral networks inheriting chirality from the chiral linkers [116-124].

For chiroptical signal arising from self-assembled and aggregated structures, the chiroptical response is usually broadened and shifted from its SPR absorption, which is known as a phenomenon called Duysens flattening [125-127]. This flattening effect results from the inhomogeneous size distribution of particulate species in solution with slight difference in each individual maximum absorption [125]. The degree of flattening of CD is different from the flattening in its corresponding absorption spectrum [126]

$$Abs^{(susp)} = Abs^{(sol)} - (2.303a^2l^2 < (\partial c)^2 > /2) \quad (6)$$

The amount of flattening is proportional to the square of extinction coefficient (a), and the absorption is reduced proportionally relative to a homogeneous solution to the mean quadratic fluctuation of the local concentration of the absorbing species (∂c).

The flattening is usually represented by the flattening coefficient,

$$K_f^{(abs)} = \frac{Abs^{(susp)}}{Abs^{(sol)}} = 1 - \left(\frac{2.303a}{2k\lambda^2}\right)\left(1 - \frac{WN_a r}{M_w}\right) \quad (7)$$

And the degree of flattening of a spectrum (β) decreases as the amount of absorbing material (M_W) increases, which can be represented as

$$\beta^{(abs)} = 1 - K_f^{(abs)} = \frac{2.303a}{2k\lambda^2}\left[1 - \left(\frac{WN_a r}{M_W}\right)\right] \quad (8)$$

1.4 References

(1) Zang, W.; Li, G.; Wang, L.; Zhang, X. Catalytic hydrogenation by noble-metal nanocrystals with well-defined facets: a review. *Catalysis Science & Technology* **2015**, *5*, 2532-2553.

(2) Reddy, N. L.; Rao, V. N.; Vijayakumar, M.; Santhosh, R.; Anandan, S.; Karthik, M.; Shankar, M. V.; Reddy, K. R.; Shetti, N. P.; Nadagouda, M. N.; Aminabhavi, T. M. A review on frontiers in plasmonic nano-photocatalysts for hydrogen production. *Int J Hydrogen Energ* **2019**, *44*, 10453-10472.

(3) Cathcart, N.; Murshid, N.; Campbell, P.; Kitaev, V. Selective Plasmonic Sensing and Highly Ordered Metallodielectrics via Encapsulation of Plasmonic Metal Nanoparticles with Metal Oxides. *ACS Applied Nano Materials* **2018**, *1*, 6514-6524.

(4) Jiang, L. Biomedical diagnostics for all: Democratization and personalization. *Digital Medicine* **2018**, *4*, 106-108.

(5) Mosquera, J.; Henriksen-Lacey, M.; García, I.; Martínez-Calvo, M.; Rodríguez, J.; Mascareñas, J. L.; Liz-Marzán, L. M. Cellular Uptake of Gold Nanoparticles Triggered by Host–Guest Interactions. *J Am Chem Soc* **2018**, *140*, 4469-4472.

(6) Halperin, W. P. Quantum size effects in metal particles. *Reviews of Modern Physics* **1986**, *58*, 533-606.

(7) Creighton, J. A.; Eadon, D. G. Ultraviolet–visible absorption spectra of the colloidal metallic elements. *Journal of the Chemical Society, Faraday Transactions* **1991**, *87*, 3881-3891.

(8) Zhang, J. Z.; Noguez, C. Plasmonic Optical Properties and Applications of Metal Nanostructures. *Plasmonics* **2008**, *3*, 127-150.

(9) Kanelidis, I.; Kraus, T. The role of ligands in coinage-metal nanoparticles for electronics. *Beilstein J Nanotechnol* **2017**, *8*, 2625-2639.

(10) Yong, Z.; Lei, D. Y.; Lam, C. H.; Wang, Y. Ultrahigh refractive index sensing performance of plasmonic quadrupole resonances in gold nanoparticles. *Nanoscale Res Lett* **2014**, *9*, 187.

(11) Link, S.; Wang, Z. L.; El-Sayed, M. A. Alloy Formation of Gold−Silver Nanoparticles and the Dependence of the Plasmon Absorption on Their Composition. *The Journal of Physical Chemistry B* **1999**, *103*, 3529-3533.

(12) Mallin, M. P.; Murphy, C. J. Solution-Phase Synthesis of Sub-10 nm Au−Ag Alloy Nanoparticles. *Nano Lett* **2002**, *2*, 1235-1237.

(13) Raveendran, P.; Fu, J.; Wallen, S. L. A simple and "green" method for the synthesis of Au, Ag, and Au–Ag alloy nanoparticles. *Green Chem* **2006**, *8*, 34-38.

(14) Ferrando, R.; Jellinek, J.; Johnston, R. L. Nanoalloys: From Theory to Applications of Alloy Clusters and Nanoparticles. *Chemical Reviews* **2008**, *108*, 845-910.

(15) Ghosh Chaudhuri, R.; Paria, S. Core/Shell Nanoparticles: Classes, Properties, Synthesis Mechanisms, Characterization, and Applications. *Chemical Reviews* **2012**, *112*, 2373-2433.

(16) Hou, P.; Liu, H.; Li, J.; Yang, J. One-pot synthesis of noble metal nanoparticles with a core–shell construction. *Crystengcomm* **2015**, *17*, 1826-1832.

(17) El-Toni, A. M.; Habila, M. A.; Labis, J. P.; Alothman, Z. A.; Alhoshan, M.; Elzatahry, A. A.; Zhang, F. Design, synthesis and applications of core–shell, hollow core, and nanorattle multifunctional nanostructures. *Nanoscale* **2016**, *8*, 2510-2531.

(18) Fan, F.-R.; Liu, D.-Y.; Wu, Y.-F.; Duan, S.; Xie, Z.-X.; Jiang, Z.-Y.; Tian, Z.-Q. Epitaxial Growth of Heterogeneous Metal Nanocrystals: From Gold Nano-octahedra to Palladium and Silver Nanocubes. *J Am Chem Soc* **2008**, *130*, 6949-6951.

(19) Habas, S. E.; Lee, H.; Radmilovic, V.; Somorjai, G. A.; Yang, P. Shaping binary metal nanocrystals through epitaxial seeded growth. *Nat Mater* **2007**, *6*, 692.

(20) Gilroy, K. D.; Hughes, R. A.; Neretina, S. Kinetically Controlled Nucleation of Silver on Surfactant-Free Gold Seeds. *J Am Chem Soc* **2014**, *136*, 15337-15345.

(21) Tan, S. F.; Chee, S. W.; Lin, G.; Bosman, M.; Lin, M.; Mirsaidov, U.; Nijhuis, C. A. Real-Time Imaging of the Formation of Au–Ag Core–Shell Nanoparticles. *J Am Chem Soc* **2016**, *138*, 5190-5193.

(22) Zhang, Q.; Kusada, K.; Wu, D.; Yamamoto, T.; Toriyama, T.; Matsumura, S.; Kawaguchi, S.; Kubota, Y.; Kitagawa, H. Selective control of fcc and hcp crystal structures in Au–Ru solid-solution alloy nanoparticles. *Nat Commun* **2018**, *9*, 510.

(23) Tsuji, M.; Matsuo, R.; Jiang, P.; Miyamae, N.; Ueyama, D.; Nishio, M.; Hikino, S.; Kumagae, H.; Kamarudin, K. S. N.; Tang, X.-L. Shape-Dependent

Evolution of Au@Ag Core−Shell Nanocrystals by PVP-Assisted N,N-Dimethylformamide Reduction. *Cryst Growth Des* **2008**, *8*, 2528-2536.

(24) Qi, X.; Balankura, T.; Zhou, Y.; Fichthorn, K. A. How Structure-Directing Agents Control Nanocrystal Shape: Polyvinylpyrrolidone-Mediated Growth of Ag Nanocubes. *Nano Lett* **2015**, *15*, 7711-7717.

(25) Wu, X.-F.; Song, H.-Y.; Yoon, J.-M.; Yu, Y.-T.; Chen, Y.-F. Synthesis of Core−Shell Au@TiO2 Nanoparticles with Truncated Wedge-Shaped Morphology and Their Photocatalytic Properties. *Langmuir* **2009**, *25*, 6438-6447.

(26) Zhang, F. Z.; Zhang, Y.; Yue, C. L.; Zhang, R.; Yang, Y. M. Facile Fabrication of Spherical Architecture of Ni/Al Layered Double Hydroxide Based on In Situ Transformation Mechanism. *Aiche J* **2014**, *60*, 4027-4036.

(27) Ma, Y.; Kuang, Q.; Jiang, Z.; Xie, Z.; Huang, R.; Zheng, L. Synthesis of Trisoctahedral Gold Nanocrystals with Exposed High-Index Facets by a Facile Chemical Method. *Angewandte Chemie International Edition* **2008**, *47*, 8901-8904.

(28) Zhang, J.; Langille, M. R.; Personick, M. L.; Zhang, K.; Li, S.; Mirkin, C. A. Concave Cubic Gold Nanocrystals with High-Index Facets. *J Am Chem Soc* **2010**, *132*, 14012-14014.

(29) Jing, H.; Zhang, Q.; Large, N.; Yu, C.; Blom, D. A.; Nordlander, P.; Wang, H. Tunable Plasmonic Nanoparticles with Catalytically Active High-Index Facets. *Nano Lett* **2014**, *14*, 3674-3682.

(30) Amendola, V.; Pilot, R.; Frasconi, M.; Marago, O. M.; Iati, M. A. Surface plasmon resonance in gold nanoparticles: a review. *J Phys-Condens Mat* **2017**, *29*.

(31) Gutierrez, A. M.; Dziubla, T. D.; Hilt, J. Z. Recent advances on iron oxide magnetic nanoparticles as sorbents of organic pollutants in water and wastewater treatment. *Rev Environ Health* **2017**, *32*, 111-117.

(32) Martinez-Boubeta, C.; Simeonidis, K. Magnetic Nanoparticles for Water Purification. *Micro Nano Technol* **2019**, 521-552.

(33) Kosif, I.; Kratz, K.; You, S. S.; Bera, M. K.; Kim, K.; Leahy, B.; Emrick, T.; Lee, K. Y. C.; Lin, B. Robust Gold Nanoparticle Sheets by Ligand Cross-Linking at the Air–Water Interface. *ACS Nano* **2017**, *11*, 1292-1300.

(34) Xia, H.; Gao, Y.; Yin, L.; Cheng, X.; Wang, A.; Zhao, M.; Ding, J.; Shi, H. Light-Triggered Covalent Coupling of Gold Nanoparticles for Photothermal Cancer Therapy. *ChemBioChem* **2019**, *20*, 667-671.

(35) Isojima, T.; Suh, S. K.; Vander Sande, J. B.; Hatton, T. A. Controlled Assembly of Nanoparticle Structures: Spherical and Toroidal Superlattices and Nanoparticle-Coated Polymeric Beads. *Langmuir* **2009**, *25*, 8292-8298.

(36) Yi, C.; Zhang, S.; Webb, K. T.; Nie, Z. Anisotropic Self-Assembly of Hairy Inorganic Nanoparticles. *Accounts Chem Res* **2017**, *50*, 12-21.

(37) Yang, G.; Hu, L. Q.; Keiper, T. D.; Xiong, P.; Hallinan, D. T. Gold Nanoparticle Monolayers with Tunable Optical and Electrical Properties. *Langmuir* **2016**, *32*, 4022-4033.

(38) Ghosh, S. K.; Pal, T. Interparticle coupling effect on the surface plasmon resonance of gold nanoparticles: from theory to applications. *Chem Rev* **2007**, *107*, 4797-4862.

(39) Yang, G.; Hallinan, D. T. Gold Nanoparticle Monolayers from Sequential Interfacial Ligand Exchange and Migration in a Three-Phase System. *Sci Rep-Uk* **2016**, *6*, 35339.

(40) Walther, A.; Muller, A. H. E. Janus Particles: Synthesis, Self-Assembly, Physical Properties, and Applications. *Chemical Reviews* **2013**, *113*, 5194-5261.

(41) Song, Y.; Chen, S. W. Janus Nanoparticles: Preparation, Characterization, and Applications. *Chem-Asian J* **2014**, *9*, 418-430.

(42) Popescu, M. N.; Uspal, W. E.; Bechinger, C.; Fischer, P. Chemotaxis of Active Janus Nanoparticles. *Nano Lett* **2018**, *18*, 5345-5349.

(43) Du, Y.; Wei, W.; Zhang, X.; Li, Y. Tuning Metamaterials Nanostructure of Janus Gold Nanoparticle Film for Surface-Enhanced Raman Scattering. *The Journal of Physical Chemistry C* **2018**, *122*, 7997-8002.

(44) Yu, X.; Xuan, Y. Solar absorption properties of embellished GZO/Cu Janus nanoparticles. *Energy Procedia* **2019**, *158*, 345-350.

(45) Hong, L.; Jiang, S.; Granick, S. Simple Method to Produce Janus Colloidal Particles in Large Quantity. *Langmuir* **2006**, *22*, 9495-9499.

(46) Jiang, S.; Schultz, M. J.; Chen, Q.; Moore, J. S.; Granick, S. Solvent-Free Synthesis of Janus Colloidal Particles. *Langmuir* **2008**, *24*, 10073-10077.

(47) Perro, A.; Meunier, F.; Schmitt, V.; Ravaine, S. Production of large quantities of “Janus” nanoparticles using wax-in-water emulsions. *Colloids and Surfaces A: Physicochemical and Engineering Aspects* **2009**, *332*, 57-62.

(48) Ling, X. Y.; Phang, I. Y.; Acikgoz, C.; Yilmaz, M. D.; Hempenius, M. A.; Vancso, G. J.; Huskens, J. Janus Particles with Controllable Patchiness and Their Chemical Functionalization and Supramolecular Assembly. *Angewandte Chemie International Edition* **2009**, *48*, 7677-7682.

(49) Tsubokawa, N. Surface Grafting of Polymers onto Nanoparticles in a Solvent-Free Dry-System and Applications of Polymer-grafted Nanoparticles as Novel Functional Hybrid Materials. *Polymer Journal* **2007**, *39*, 983.

(50) Gann, J. P.; Yan, M. A Versatile Method for Grafting Polymers on Nanoparticles. *Langmuir* **2008**, *24*, 5319-5323.

(51) Asai, M.; Zhao, D.; Kumar, S. K. Role of Grafting Mechanism on the Polymer Coverage and Self-Assembly of Hairy Nanoparticles. *ACS Nano* **2017**, *11*, 7028-7035.

(52) Benoit, D. N.; Zhu, H.; Lilierose, M. H.; Verm, R. A.; Ali, N.; Morrison, A. N.; Fortner, J. D.; Avendano, C.; Colvin, V. L. Measuring the Grafting Density of Nanoparticles in Solution by Analytical Ultracentrifugation and Total Organic Carbon Analysis. *Anal Chem* **2012**, *84*, 9238-9245.

(53) Gatemala, H.; Pienpinijtham, P.; Thammacharoen, C.; Ekgasit, S. Rapid fabrication of silver microplates under an oxidative etching environment consisting of O-2/Cl-, NH4OH/H2O2, and H2O2. *Crystengcomm* **2015**, *17*, 5530-5537.

(54) Pradhan, S.; Xu, L. P.; Chen, S. W. Janus nanoparticles by interfacial engineering. *Adv Funct Mater* **2007**, *17*, 2385-2392.

(55) Kossak, A. E.; Stephens, B. O.; Tian, Y.; Liu, P.; Chen, M.; Kempa, T. J. Anisotropic and Multicomponent Nanostructures by Controlled Symmetry Breaking of Metal Halide Intermediates. *Nano Lett* **2018**, *18*, 2324-2328.

(56) Huang, Z.; Zhao, Z.-J.; Zhang, Q.; Han, L.; Jiang, X.; Li, C.; Cardenas, M. T. P.; Huang, P.; Yin, J.-J.; Luo, J.; Gong, J.; Nie, Z. A welding phenomenon of dissimilar nanoparticles in dispersion. *Nat Commun* **2019**, *10*, 219.

(57) Sánchez, A.; Ovejero Paredes, K.; Ruiz-Cabello, J.; Martínez-Ruíz, P.; Pingarrón, J. M.; Villalonga, R.; Filice, M. Hybrid Decorated Core@Shell Janus Nanoparticles as a Flexible Platform for Targeted Multimodal Molecular Bioimaging of Cancer. *Acs Appl Mater Inter* **2018**, *10*, 31032-31043.

(58) Zhang, L.; Li, S.; Chen, X.; Wang, T.; Li, L.; Su, Z.; Wang, C. Tailored Surfaces on 2D Material: UFO-Like Cyclodextrin-Pd Nanosheet/Metal Organic Framework Janus Nanoparticles for Synergistic Cancer Therapy. *Adv Funct Mater* **2018**, *28*, 1803815.

(59) Archer, R. J.; Parnell, A. J.; Campbell, A. I.; Howse, J. R.; Ebbens, S. J. A Pickering Emulsion Route to Swimming Active Janus Colloids. *Advanced Science* **2018**, *5*, 1700528.

(60) Ying, Y.; Pumera, M. Micro/Nanomotors for Water Purification. *Chemistry – A European Journal* **2019**, *25*, 106-121.

(61) Aguilar, M.; Ali Cavasonza, L.; Alpat, B.; Ambrosi, G.; Arruda, L.; Attig, N.; Aupetit, S.; Azzarello, P.; Bachlechner, A.; Barao, F.; Barrau, A.; Barrin, L.; Bartoloni, A.; Basara, L.; Basegmez-du Pree, S.; Battarbee, M.; Battiston, R.; Bazo, J.; Becker, U.; Behlmann, M.; Beischer, B.; Berdugo, J.; Bertucci, B.; Bindi, V.; Boella, G.; de Boer, W.; Bollweg, K.; Bonnivard, V.; Borgia, B.; Boschini, M. J.; Bourquin, M.; Bueno, E. F.; Burger, J.; Cadoux, F.; Cai, X. D.; Capell, M.; Caroff, S.; Casaus, J.; Castellini, G.; Cernuda, I.; Cervelli, F.; Chae, M. J.; Chang, Y. H.; Chen, A. I.; Chen, G. M.; Chen, H. S.; Cheng, L.; Chou, H. Y.; Choumilov, E.; Choutko, V.; Chung, C. H.; Clark, C.; Clavero, R.; Coignet, G.; Consolandi, C.; Contin, A.; Corti, C.; Coste, B.; Creus, W.; Crispoltoni, M.; Cui, Z.; Dai, Y. M.; Delgado, C.; Della Torre, S.; Demirkoz, M. B.; Derome, L.; Di Falco, S.; Dimiccoli, F.; Diaz, C.; von Doetinchem, P.; Dong, F.; Donnini, F.; Duranti, M.; D'Urso, D.; Egorov, A.; Eline, A.; Eronen, T.; Feng, J.; Fiandrini, E.; Finch, E.; Fisher, P.; Formato, V.; Galaktionov, Y.; Gallucci, G.; Garcia, B.; Garcia-Lopez, R. J.; Gargiulo, C.; Gast, H.; Gebauer, I.; Gervasi, M.; Ghelfi, A.; Giovacchini, F.; Goglov, P.; Gomez-Coral, D. M.; Gong, J.; Goy, C.; Grabski, V.; Grandi, D.; Graziani, M.; Guerri, I. Antiproton Flux, Antiproton-to-Proton Flux Ratio, and Properties of Elementary Particle Fluxes in Primary Cosmic Rays Measured with the Alpha Magnetic Spectrometer on the International Space Station. *Phys Rev Lett* **2016**, *117*, 091103.

(62) Xuan, M.; Wu, Z.; Shao, J.; Dai, L.; Si, T.; He, Q. Near Infrared Light-Powered Janus Mesoporous Silica Nanoparticle Motors. *J Am Chem Soc* **2016**, *138*, 6492-6497.

(63) Zhang, D.; Wang, D.; Li, J.; Xu, X.; Zhang, H.; Duan, R.; Song, B.; Zhang, D.; Dong, B. One-step synthesis of PCL/Mg Janus micromotor for precious metal ion sensing, removal and recycling. *J Mater Sci* **2019**, *54*, 7322-7332.

(64) Qin, W.; Peng, T.; Gao, Y.; Wang, F.; Hu, X.; Wang, K.; Shi, J.; Li, D.; Ren, J.; Fan, C. Catalysis-Driven Self-Thermophoresis of Janus Plasmonic Nanomotors. *Angewandte Chemie International Edition* **2017**, *56*, 515-518.

(65) Song, Y.; Chen, S. W. Janus Nanoparticles as Versatile Phase-Transfer Reagents. *Langmuir* **2014**, *30*, 6389-6397.

(66) Lu, J. E.; Yang, C. H.; Wang, H.; Yam, C. Y.; Yu, Z. G.; Chen, S. W. Plasmonic circular dichroism of vesicle-like nanostructures by template-less self-assembly of achiral Janus nanoparticles. *Nanoscale* **2018**, *10*, 14586-14593.

(67) Lu, J. E., Peng, Y., Chen, S. Janus Nanoparticle Emulsions as Chiral Nanoreactors for Enantiomerically Selective Ligand Exchange. *Part. Part. Sys. Char.* **2019**, *1800564*, 1-5.

(68) Khoee, S.; Nouri, A.: Chapter 4 - Preparation of Janus nanoparticles and its application in drug delivery. In *Design and Development of New Nanocarriers*; Grumezescu, A. M., Ed.; William Andrew Publishing, 2018; pp 145-180.

(69) Kang, C.; Honciuc, A. Self-Assembly of Janus Nanoparticles into Transformable Suprastructures. *The Journal of Physical Chemistry Letters* **2018**, *9*, 1415-1421.

(70) Kang, C.; Honciuc, A. Influence of Geometries on the Assembly of Snowman-Shaped Janus Nanoparticles. *ACS Nano* **2018**, *12*, 3741-3750.

(71) Ren, B.; Ruditskiy, A.; Song, J. H.; Kretzschmar, I. Assembly Behavior of Iron Oxide-Capped Janus Particles in a Magnetic Field. *Langmuir* **2012**, *28*, 1149-1156.

(72) Ruditskiy, A.; Ren, B.; Kretzschmar, I. Behaviour of iron oxide (Fe3O4) Janus particles in overlapping external AC electric and static magnetic fields. *Soft Matter* **2013**, *9*, 9174-9181.

(73) Xie, Q.; Davies, G. B.; Harting, J. Direct Assembly of Magnetic Janus Particles at a Droplet Interface. *ACS Nano* **2017**, *11*, 11232-11239.

(74) Hu, H.; Ji, F.; Xu, Y.; Yu, J.; Liu, Q.; Chen, L.; Chen, Q.; Wen, P.; Lifshitz, Y.; Wang, Y.; Zhang, Q.; Lee, S.-T. Reversible and Precise Self-Assembly of Janus Metal-Organosilica Nanoparticles through a Linker-Free Approach. *ACS Nano* **2016**, *10*, 7323-7330.

(75) Ma, W.; Xu, L.; de Moura, A. F.; Wu, X.; Kuang, H.; Xu, C.; Kotov, N. A. Chiral Inorganic Nanostructures. *Chem Rev* **2017**, *117*, 8041-8093.

(76) Yoo, S.; Park, Q. H.: Metamaterials and chiral sensing: a review of fundamentals and applications. In *Nanophotonics*, 2019; Vol. 8; pp 249.

(77) Schaaff, T. G.; Whetten, R. L. Giant gold-glutathione cluster compounds: Intense optical activity in metal-based transitions. *J Phys Chem B* **2000**, *104*, 2630-2641.

(78) Garzon, I. L.; Reyes-Nava, J. A.; Rodriguez-Hernandez, J. I.; Sigal, I.; Beltran, M. R.; Michaelian, K. Chirality in bare and passivated gold nanoclusters. *Phys Rev B* **2002**, *66*.

(79) Garzon. Do Thiols Merely Passivate Gold Nanoclusters? *Phys. Rev. Lett.* **2000**, *85*, 5250-5251.

(80) Garzon, I. L.; Artacho, E.; Beltran, M. R.; Garcia, A.; Junquera, J.; Michaelian, K.; Ordejon, P.; Rovira, C.; Sanchez-Portal, D.; Soler, J. M. Hybrid DNA-gold nanostructured materials: an ab initio approach. *Nanotechnology* **2001**, *12*, 126-131.

(81) Noguez, C.; Garzon, I. L. Optically active metal nanoparticles. *Chem Soc Rev* **2009**, *38*, 757-771.

(82) Noguez, C.; Sanchez-Castillo, A.; Hidalgo, F. Role of Morphology in the Enhanced Optical Activity of Ligand-Protected Metal Nanoparticles. *J Phys Chem Lett* **2011**, *2*, 1038-1044.

(83) inoue: *Chiral Photochemistry. Molecular and Supramolecular Photochemistry*; 11 ed.; CRC Press: New York, 2004.

(84) Valev, V. K.; Baumberg, J. J.; Sibilia, C.; Verbiest, T. Chirality and Chiroptical Effects in Plasmonic Nanostructures: Fundamentals, Recent Progress, and Outlook. *Adv Mater* **2013**, *25*, 2517-2534.

(85) Reichelt, M.; Koch, S. W.; Krasavin, A. V.; Moloney, J. V.; Schwanecke, A. S.; Stroucken, T.; Wright, E. M.; Zheludev, N. I. Broken enantiomeric symmetry for electromagnetic waves interacting with planar chiral nanostructures. *Appl Phys B-Lasers O* **2006**, *84*, 97-101.

(86) Valev, V. K.; Smisdom, N.; Silhanek, A. V.; De Clercq, B.; Gillijns, W.; Ameloot, M.; Moshchalkov, V. V.; Verbiest, T. Plasmonic Ratchet Wheels: Switching Circular Dichroism by Arranging Chiral Nanostructures. *Nano Lett* **2009**, *9*, 3945-3948.

(87) Fan, Z. Y.; Govorov, A. O. Chiral Nanocrystals: Plasmonic Spectra and Circular Dichroism. *Nano Lett* **2012**, *12*, 3283-3289.

(88) Schaferling, M.; Dregely, D.; Hentschel, M.; Giessen, H. Tailoring Enhanced Optical Chirality: Design Principles for Chiral Plasmonic Nanostructures. *Phys Rev X* **2012**, *2*.

(89) Frank, B.; Yin, X. H.; Schaferling, M.; Zhao, J.; Hein, S. M.; Braun, P. V.; Giessen, H. Large-Area 3D Chiral Plasmonic Structures. *Acs Nano* **2013**, *7*, 6321-6329.

(90) Gansel, J. K.; Thiel, M.; Rill, M. S.; Decker, M.; Bade, K.; Saile, V.; von Freymann, G.; Linden, S.; Wegener, M. Gold Helix Photonic Metamaterial as Broadband Circular Polarizer. *Science* **2009**, *325*, 1513-1515.

(91) Humblot, V.; Haq, S.; Muryn, C.; Hofer, W. A.; Raval, R. From local adsorption stresses to chiral surfaces: (R,R)-tartaric acid on Ni(110). *J Am Chem Soc* **2002**, *124*, 503-510.

(92) Gellman, A. J.; Huang, Y.; Feng, X.; Pushkarev, V. V.; Holsclaw, B.; Mhatre, B. S. Superenantioselective Chiral Surface Explosions. *J Am Chem Soc* **2013**, *135*, 19208-19214.

(93) Wattanakit, C.; Come, Y. B.; Lapeyre, V.; Bopp, P. A.; Heim, M.; Yadnum, S.; Nokbin, S.; Warakulwit, C.; Limtrakul, J.; Kuhn, A. Enantioselective recognition at mesoporous chiral metal surfaces. *Nat Commun* **2014**, *5*, 3325.

(94) Wang, P. P.; Yu, S. J.; Govorov, A. O.; Ouyang, M. Cooperative expression of atomic chirality in inorganic nanostructures. *Nat Commun* **2017**, *8*, 14312.

(95) Lee, H. E.; Ahn, H. Y.; Mun, J.; Lee, Y. Y.; Kim, M.; Cho, N. H.; Chang, K.; Kim, W. S.; Rho, J.; Nam, K. T. Amino-acid- and peptide-directed synthesis of chiral plasmonic gold nanoparticles. *Nature* **2018**, *556*, 360-365.

(96) Greber, T.; Šljivančanin, Ž.; Schillinger, R.; Wider, J.; Hammer, B. Chiral Recognition of Organic Molecules by Atomic Kinks on Surfaces. *Phys Rev Lett* **2006**, *96*, 056103.

(97) Kühnle, A.; Linderoth, T. R.; Besenbacher, F. Enantiospecific Adsorption of Cysteine at Chiral Kink Sites on Au(110)-(1×2). *J Am Chem Soc* **2006**, *128*, 1076-1077.

(98) Schillinger, R.; Šljivančanin, Ž.; Hammer, B.; Greber, T. Probing Enantioselectivity with X-Ray Photoelectron Spectroscopy and Density Functional Theory. *Phys Rev Lett* **2007**, *98*, 136102.

(99) Knoppe, S.; Dharmaratne, A. C.; Schreiner, E.; Dass, A.; Burgi, T. Ligand Exchange Reactions on Au-38 and Au-40 Clusters: A Combined Circular Dichroism and Mass Spectrometry Study. *J Am Chem Soc* **2010**, *132*, 16783-16789.

(100) Slocik, J. M.; Govorov, A. O.; Naik, R. R. Plasmonic Circular Dichroism of Peptide-Functionalized Gold Nanoparticles. *Nano Lett* **2011**, *11*, 701-705.

(101) Besteiro, L. V.; Zhang, H.; Plain, J.; Markovich, G.; Wang, Z. M.; Govorov, A. O. Aluminum Nanoparticles with Hot Spots for Plasmon-Induced Circular Dichroism of Chiral Molecules in the UV Spectral Interval. *Adv Opt Mater* **2017**, *5*.

(102) Wang, R. Y.; Wang, H. L.; Wu, X. C.; Ji, Y. L.; Wang, P.; Qu, Y.; Chung, T. S. Chiral assembly of gold nanorods with collective plasmonic circular dichroism response. *Soft Matter* **2011**, *7*, 8370-8375.

(103) Maoz, B. M.; van der Weegen, R.; Fan, Z. Y.; Govorov, A. O.; Ellestad, G.; Berova, N.; Meijer, E. W.; Markovich, G. Plasmonic Chiroptical Response of Silver Nanoparticles Interacting with Chiral Supramolecular Assemblies. *J Am Chem Soc* **2012**, *134*, 17807-17813.

(104) Azizi, A.; Ranjbar, B.; Moghadam, T. T.; Bagheri, Z.; Baglou, S. R. Surface plasmon resonance coupled circular dichroism of DNA-gold nanorods assembly. *J Phys D Appl Phys* **2014**, *47*.

(105) Zhu, F.; Li, X. Y.; Li, Y. C.; Yan, M.; Liu, S. Q. Enantioselective Circular Dichroism Sensing of Cysteine and Glutathione with Gold Nanorods. *Anal Chem* **2015**, *87*, 357-361.

(106) Raghavendra, A. J.; Alsaleh, N.; Brown, J. M.; Podila, R. Charge-transfer interactions induce surface dependent conformational changes in apolipoprotein biocorona. *Biointerphases* **2017**, *12*, 02D402.

(107) Shen, Y. X.; Tian, G.; Huang, H.; He, Y. W.; Xie, Q. L.; Song, F.; Lu, Y. H.; Wang, P. S.; Gao, Y. L. Chiral Self-Assembly of Nonplanar 10,10 '-Dibromo-9,9 '-bianthryl Molecules on Ag(111). *Langmuir* **2017**, *33*, 2993-2999.

(108) Hendry, E.; Carpy, T.; Johnston, J.; Popland, M.; Mikhaylovskiy, R. V.; Lapthorn, A. J.; Kelly, S. M.; Barron, L. D.; Gadegaard, N.; Kadodwala, M. Ultrasensitive detection and characterization of biomolecules using superchiral fields. *Nat Nanotechnol* **2010**, *5*, 783-787.

(109) Xu, Z.; Xu, L. G.; Liz-Marzan, L. M.; Ma, W.; Kotov, N. A.; Wang, L. B.; Kuang, H.; Xu, C. L. Sensitive Detection of Silver Ions Based on Chiroplasmonic Assemblies of Nanoparticles. *Adv Opt Mater* **2013**, *1*, 626-630.

(110) Droulias, S.; Yannopapas, V. Broad-Band Giant Circular Dichroism in Metamaterials of Twisted Chains of Metallic Nanoparticles. *J Phys Chem C* **2013**, *117*, 1130-1135.

(111) Narushima, T.; Hashiyada, S.; Okamoto, H. Nanoscopic Study on Developing Optical Activity with Increasing Chirality for Two-Dimensional Metal Nanostructures. *Acs Photonics* **2014**, *1*, 732-738.

(112) Ogier, R.; Fang, Y. R.; Svedendahl, M.; Johansson, P.; Kall, M. Macroscopic Layers of Chiral Plasmonic Nanoparticle Oligomers from Colloidal Lithography. *Acs Photonics* **2014**, *1*, 1074-1081.

(113) Biswas, S.; Liu, X. Y.; Jarrett, J. W.; Brown, D.; Pustovit, V.; Urbas, A.; Knappenberger, K. L.; Nealey, P. F.; Vaia, R. A. Nonlinear Chiro-Optical Amplification by Plasmonic Nanolens Arrays Formed via Directed Assembly of Gold Nanoparticles. *Nano Lett* **2015**, *15*, 1836-1842.

(114) Banzer, P.; Wozniak, P.; Mick, U.; De Leon, I.; Boyd, R. W. Chiral optical response of planar and symmetric nanotrimers enabled by heteromaterial selection. *Nat Commun* **2016**, *7*.

(115) Najafabadi, A. F.; Pakizeh, T. Analytical Chiroptics of 2D and 3D Nanoantennas. *Acs Photonics* **2017**, *4*, 1447-1452.

(116) Chen, W.; Bian, A.; Agarwal, A.; Liu, L. Q.; Shen, H. B.; Wang, L. B.; Xu, C. L.; Kotov, N. A. Nanoparticle Superstructures Made by Polymerase Chain Reaction: Collective Interactions of Nanoparticles and a New Principle for Chiral Materials. *Nano Lett* **2009**, *9*, 2153-2159.

(117) Kuzyk, A.; Schreiber, R.; Fan, Z. Y.; Pardatscher, G.; Roller, E. M.; Hogele, A.; Simmel, F. C.; Govorov, A. O.; Liedl, T. DNA-based self-assembly of chiral plasmonic nanostructures with tailored optical response. *Nature* **2012**, *483*, 311-314.

(118) Lan, X.; Chen, Z.; Dai, G. L.; Lu, X. X.; Ni, W. H.; Wang, Q. B. Bifacial DNA Origami-Directed Discrete, Three-Dimensional, Anisotropic Plasmonic Nanoarchitectures with Tailored Optical Chirality. *J Am Chem Soc* **2013**, *135*, 11441-11444.

(119) Shen, X. B.; Asenjo-Garcia, A.; Liu, Q.; Jiang, Q.; de Abajo, F. J. G.; Liu, N.; Ding, B. Q. Three-Dimensional Plasmonic Chiral Tetramers Assembled by DNA Origami. *Nano Lett* **2013**, *13*, 2128-2133.

(120) Wu, X. L.; Xu, L. G.; Liu, L. Q.; Ma, W.; Yin, H. H.; Kuang, H.; Wang, L. B.; Xu, C. L.; Kotov, N. A. Unexpected Chirality of Nanoparticle Dimers and Ultrasensitive Chiroplasmonic Bioanalysis. *J Am Chem Soc* **2013**, *135*, 18629-18636.

(121) Lan, X.; Lu, X. X.; Shen, C. Q.; Ke, Y. G.; Ni, W. H.; Wang, Q. B. Au Nanorod Helical Superstructures with Designed Chirality. *J Am Chem Soc* **2015**, *137*, 457-462.

(122) Li, S.; Xu, L. G.; Ma, W.; Wu, X. L.; Sun, M. Z.; Kuang, H.; Wang, L. B.; Kotov, N. A.; Xu, C. L. Dual-Mode Ultrasensitive Quantification of MicroRNA in Living Cells by Chiroplasmonic Nanopyramids Self-Assembled from Gold and Upconversion Nanoparticles. *J Am Chem Soc* **2016**, *138*, 306-312.

(123) Urban, M. J.; Dutta, P. K.; Wang, P. F.; Duan, X. Y.; Shen, X. B.; Ding, B. Q.; Ke, Y. G.; Liu, N. Plasmonic Toroidal Metamolecules Assembled by DNA Origami. *J Am Chem Soc* **2016**, *138*, 5495-5498.

(124) Wu, X. L.; Xu, L. G.; Ma, W.; Liu, L. Q.; Kuang, H.; Kotov, N. A.; Xu, C. L. Propeller-Like Nanorod-Upconversion Nanoparticle Assemblies with Intense Chiroptical Activity and Luminescence Enhancement in Aqueous Phase. *Adv Mater* **2016**, *28*, 5907-+.

(125) Duyens, L. N. M. The flattering of the absorption spectrum of suspensions, as compared to that of solutions. *Biochimica et Biophysica Acta* **1956**, *19*, 1-12.

(126) Bustamante, C.; Maestre, M. F. Statistical effects in the absorption and optical activity of particulate suspensions. *Proceedings of the National Academy of Sciences* **1988**, *85*, 8482.

(127) Castiglioni, E.; Abbate, S.; Longhi, G.; Gangemi, R. Wavelength shifts in solid-state circular dichroism spectra: A possible explanation. *Chirality* **2007**, *19*, 491-496.

Chapter 2

Plasmonic circular dichroism of vesicle-like nanostructures by the template-less self-assembly of achiral Janus nanoparticles

2.1 Abstract

Chiral nanostructures have been attracting extensive interest in recent years primarily because of the unique materials properties that can be exploited for diverse applications. In this study, gold Janus nanoparticles, with hexanethiolates and 3-mercapto-1,2-propanediol segregated on the two hemispheres of the metal cores (dia. 2.7 ± 0.4 nm), self-assembled into vesicle-like, hollow nanostructures in both water and organic media, and exhibited apparent plasmonic circular dichroism (PCD) absorption in the visible range. This was in contrast to individual Janus nanoparticles, bulk-exchange nanoparticles where the two ligands were homogeneously mixed on the nanoparticle surface, or nanoparticles capped with only one kind of ligand. The PCD signals were found to become intensified with increasing coverage of the 3-mercapto-1,2-propanediol ligands on the nanoparticle surface. This was accounted for by the dipolar property of the structurally asymmetrical Janus nanoparticles, and theoretical simulations based on first principles calculations showed that when the nanoparticle dipoles self-assembled onto the surface of a hollow sphere, a vertex was formed which gave rise to the unique chiral characteristics. The resulting chiral nanoparticle vesicles could be exploited for the separation of optical enantiomers, as manifested in the selective identification and separation of D-alanine from the L-isomer.

2.2 Introduction

In recent years, plasmonic metal nanoparticles have been found to exhibit unique chiroptical properties, and the nanoscale chirality may be exploited for enantiomeric sensing and catalysis, as well as development of next-generation optoelectronic devices.[1-3] Unlike conventional chiral molecules (e.g., peptides, proteins, and DNA) that typically exhibit circular dichroism (CD) absorption in the far ultraviolet (UV, 140 – 250 nm) region,[4,5] plasmonic circular dichroism (PCD) is generally observed in the visible range and can be readily manipulated by the chemical nature and morphology of the plasmonic nanoparticles.[2] This may be due to the formation of intrinsically chiral nanoparticle cores, capping with chiral organic ligands, as well as arrangements of achiral nanoparticles into chiral organized ensembles. In the first strategy, chiral templates are generally used to assist the growth of nanoparticles, where chirality is imprinted onto the nanoparticle core during the growth process, resulting in the formation of chiral nanoparticles.[6] For instance, Shemer et al.[7] demonstrated that chirality could be inherited by silver nanoparticles using DNA as templates during nanoparticle formation, whereas silver nanoparticles that were prepared by $NaBH_4$ reduction and then underwent ligand exchange reactions with the same DNA ligands did not show any CD signal in the same wavelength region. The intrinsic chirality of plasmonic nanoparticles can also arise from a chiral core shape, such as helical/spiral structures and/or the formation of chiral microfacets on the nanoparticle surfaces.[8-12] For achiral plasmonic nanoparticles, PCD can also be produced by using chiral capping ligands, due to strong dipole (and higher-order)

interactions between the ligand and nanoparticle core electrons. Upon interactions with the chiral ligands, the symmetry of the electronic property on the nanoparticle surface is distorted, leading to different extinction coefficients between the left- and right-handed circularly polarized light.[13-15] For instance, L-glutathione-capped gold nanoparticles[16] and silver nanocubes[17] have been found to exhibit well-defined PCD signals that coincide with the surface plasmon resonance (SPR) absorption of the nanoparticles. PCD has also been observed with chiral molecules entrapped at the core-shell interface of Au@Ag nanorods.[18]

Nanoscale chirality can also be induced by controlled assembly of nanoparticles into chiral superstructures.[19] For instance, PCD has been observed with gold nanoparticle networks formed by using (chiral) DNA or peptides as interparticle linkers,[20,21] arrangements of gold nanoparticles onto helical nanofiber templates,[22-24] and layer-by-layer deposition of gold nanoparticles into twisted chains.[25] Plasmonic chiroptical properties have also been found with heterodimers of two gold nanoparticles of different sizes (50 nm and 150 nm) due to the interference between the higher-order and dipolar modes in the heterodimer pair,[26] as well as three-dimensional oligomers of gold nanorods.[27-29]

In the present study, we demonstrated that gold Janus nanoparticles (JNPs), with hydrophobic hexanethiolates (C6) and hydrophilic 3-mercapto-1,2-propanediol (MPD) ligands segregated on the two hemispheres of the metal

cores, self-assembled into vesicle-like, hollow nanostructures without the assistance of any chiral templates/scaffolds, and exhibited apparent PCD absorption in the visible range. This was accounted for by the dipolar property of the structurally asymmetrical JNPs arranged on a hollow sphere forming a vertex, as manifested in theoretical simulations based on first principles calculations, in sharp contrast with the achiral response observed with individual JNPs, bulk-exchange nanoparticles with the two ligands homogeneously mixed on the nanoparticle surface, or nanoparticles capped with only one kind of the ligands. The unique chiral characteristics of the JNP vesicles can be exploited for selective binding and phase transfer of optical enantiomers, as manifested in the effective identification and separation of D-alanine from the L-isomer.

2.3 Results and Discussion

As described previously (and detailed in the Experimental Section),[30-32] the JNPs were prepared by interfacial ligand exchange reactions of hexanethiolate-capped gold (AuC6, 2.7 ± 0.4 nm in diameter, **Figure 2.1**) nanoparticles with (racemic) MPD at the air|water interface, exhibiting hydrophobic C6 ligands on one face and hydrophilic MPD on the other (inset to **Figure 2.2A**).[33] The surface concentration of MPD was varied by reaction time (1, 4, and 10 h), and quantitatively evaluated by ^{1}H NMR measurements at 17.5 % for JNP1, 28.3 % for JNP4, and 61.4 % for JNP10, based on the integrated peak areas of the terminal methyl protons of the C6 ligands and the methoxy protons of the MPD

ligands (**Figure 2.3**).[30] For the control sample where the ligand exchange reaction was carried out by simply mixing AuC6 and MPD in THF (BE nanoparticles, inset to **Figure 2.2C**), the MPD surface coverage was estimated to be ca. 66.0%. That is, the JNP10 and BE nanoparticles are akin to structural isomers with a similar core-ligand composition but a different surface distribution of the capping ligands. The incorporation of MPD ligands onto the nanoparticle surfaces was also manifested in FTIR measurements (**Figure 2.4**), where the O–H stretch can be found at 3300 – 3200 cm^{-1} and the C–O vibration at 1030 cm^{-1}.[30]

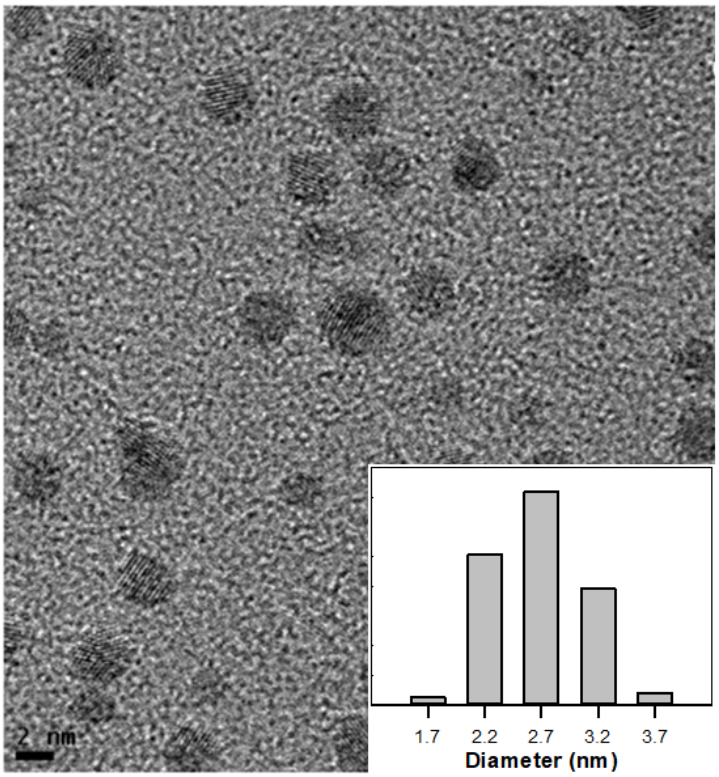

Figure 2.1 Representative TEM image of AuC6 nanoparticles. Scale bar 2 nm. Inset is the core size histogram.

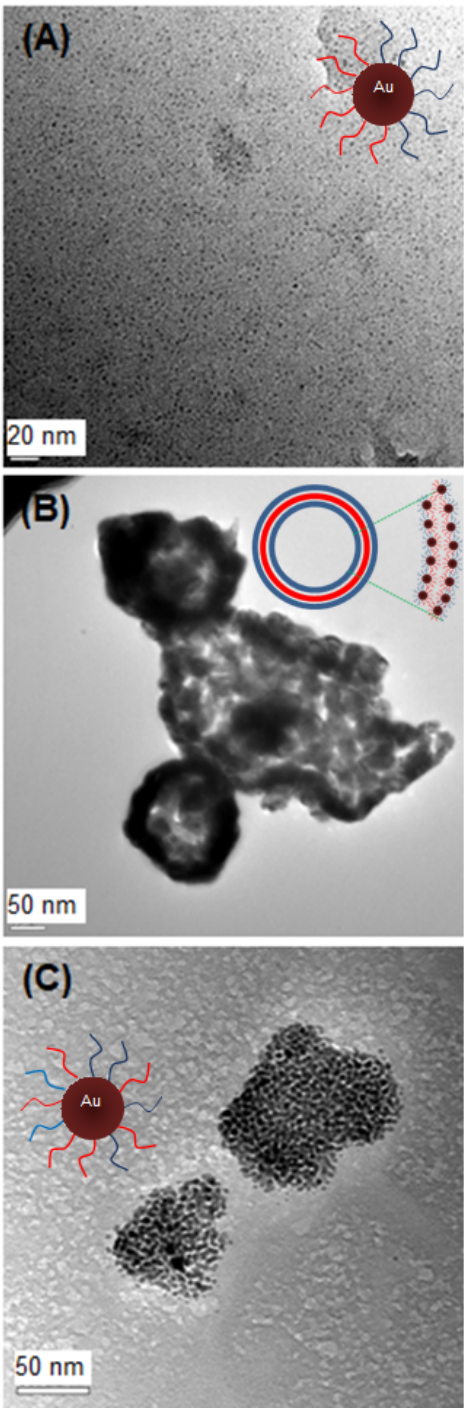

Figure 2.2 TEM images of JNP10 at a concentration of (A) 0.01 mg mL^{-1} and (B) 0.15 mg mL^{-1} in water. (C) BE nanoparticles at 0.15 mg mL^{-1} in water. Scale bars are 20 nm in panel (A), and 50 nm in panels (B) and (C). The insets are the schematic illustrations of (A) JNP, (B) JNP assembly, and (C) BE nanoparticles.

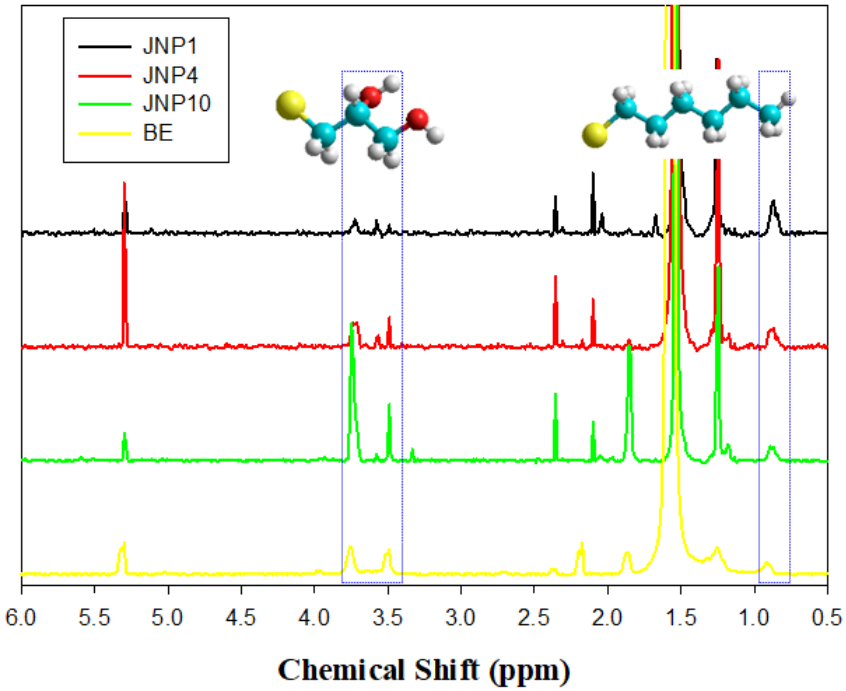

Figure 2.3 ^{1}H NMR spectra of AuC6-MPD JNP and BE nanoparticles in CD_2Cl_2. Based on the ratio of the integrated peak areas of the terminal C**H**$_3$ and -C**H**OH-C**H**$_2$OH protons (dotted boxes, as highlighted in figure insets), the MPD surface coverage was estimated to be 17.5 % for JNP1, 28.3 % for JNP4, 61.4 % for JNP10, and 66.0 % for BE nanoparticles.

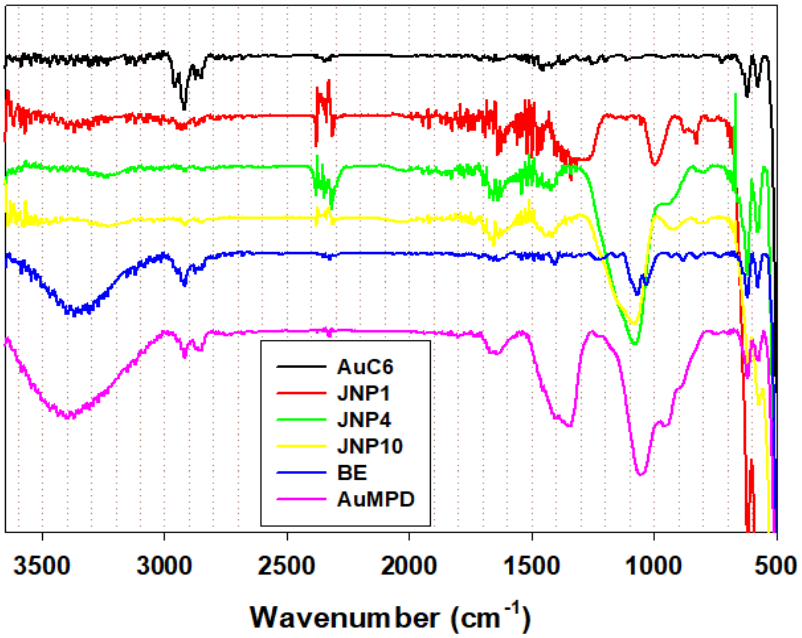

Figure 2.4 FTIR spectra of AuC6, AuC6-MPD JNP, BE and AuMPD nanoparticles.

JNPs have been known to behave analogously to amphiphilic surfactant molecules, and can self-assemble into organized vesicle-like superstructures both in water and apolar organic solvents such as THF and $CHCl_3$.[32,34] In fact, in an earlier study,[34] the critical micelle concentration (CMC) of JNPs was found to be at least three orders of magnitude lower than that of Triton X-100. Such concentration dependence of the formation of nanoparticle ensembles can be visually evidenced in TEM measurements. From **Figure 2.2A**, one can see that at the concentration of 0.01 mg/mL in water, JNP10 nanoparticles were well dispersed as individual particles without apparent agglomeration. Yet when the concentration was increased to 0.15 mg/mL, the nanoparticles can be seen to form vesicle-like, hollow organized assemblies with lateral dimensions in the

range of 50 to 200 nm (**Figure 2.2B** and inset, **2.5A**).[32] The variation of the nanoparticle morphologies can also be manifested in AFM topographic measurements (**Figure 2.5**). One may notice that whereas BE nanoparticles also formed ensemble structures of similar dimensions (**Figure 2.2C and 2.5B**), the nanoparticle superstructures are solid rather than hollow. This may be due to the segregated distribution of the (hydrophobic) C6 and (hydrophilic) MPD ligands on the JNP surface that rendered it possible for the nanoparticles to arrange into vesicle-like structures, whereas for the BE nanoparticles, the random mix of the C6 and MPD ligands made it difficult for the nanoparticles to find an orientation with a minimal surface energy.

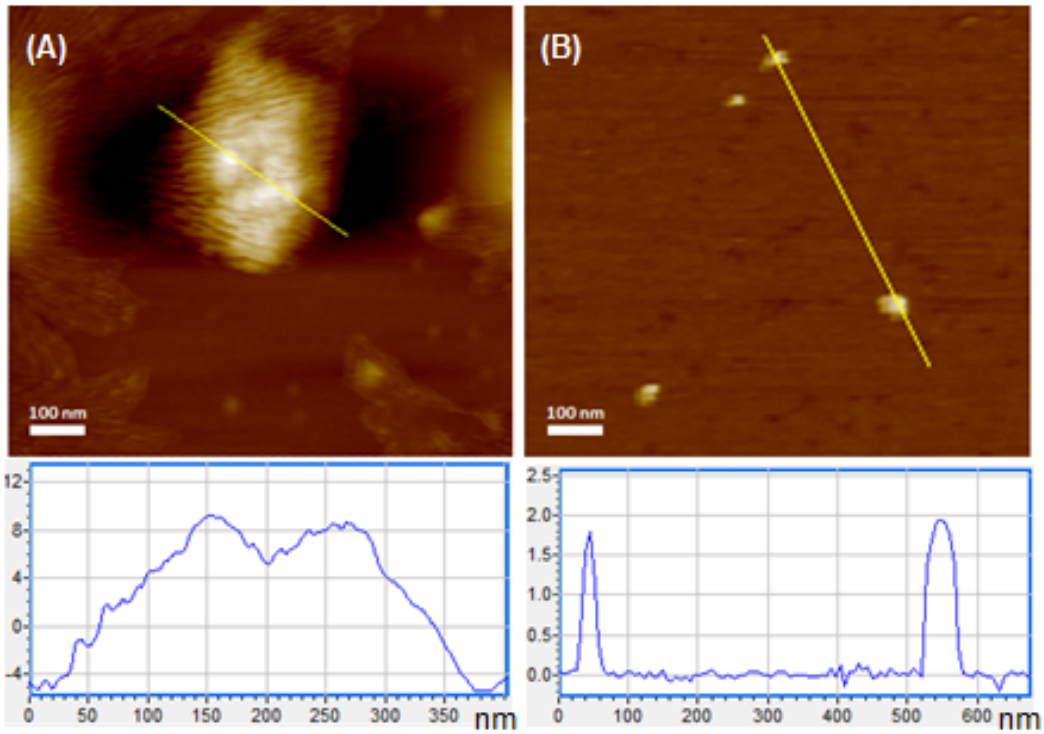

Figure 2.5 Representative AFM topographs of JNP10 nanoparticles at the concentrations of (a) 0.15 mg/mL and (b) 0.01 mg/mL in water. The bottom panels are the corresponding height profiles of the line scans in the top panels.

The optical properties of the nanoparticles were then examined by UV-vis absorption measurements. **Figure 2.6A** depicts the UV-vis spectra of the series of JNP and BE nanoparticles in water at the concentration of 0.15 mg/mL. One can see that at this concentration, both JNP (black, red, and green curves) and BE nanoparticles (yellow curve) showed a broad absorption peak at ca. 610 nm, a marked red-shift of ca. 100 nm as compared to the SPR of the original AuC6 nanoparticles in $CHCl_3$ (**Figure 2.7**) and AuMPD nanoparticles (blue curve) that were readily dispersed in water, due to strong interparticle electronic interactions as a result of the formation of nanoparticle ensembles (**Figure 2.2B**).[35,36]

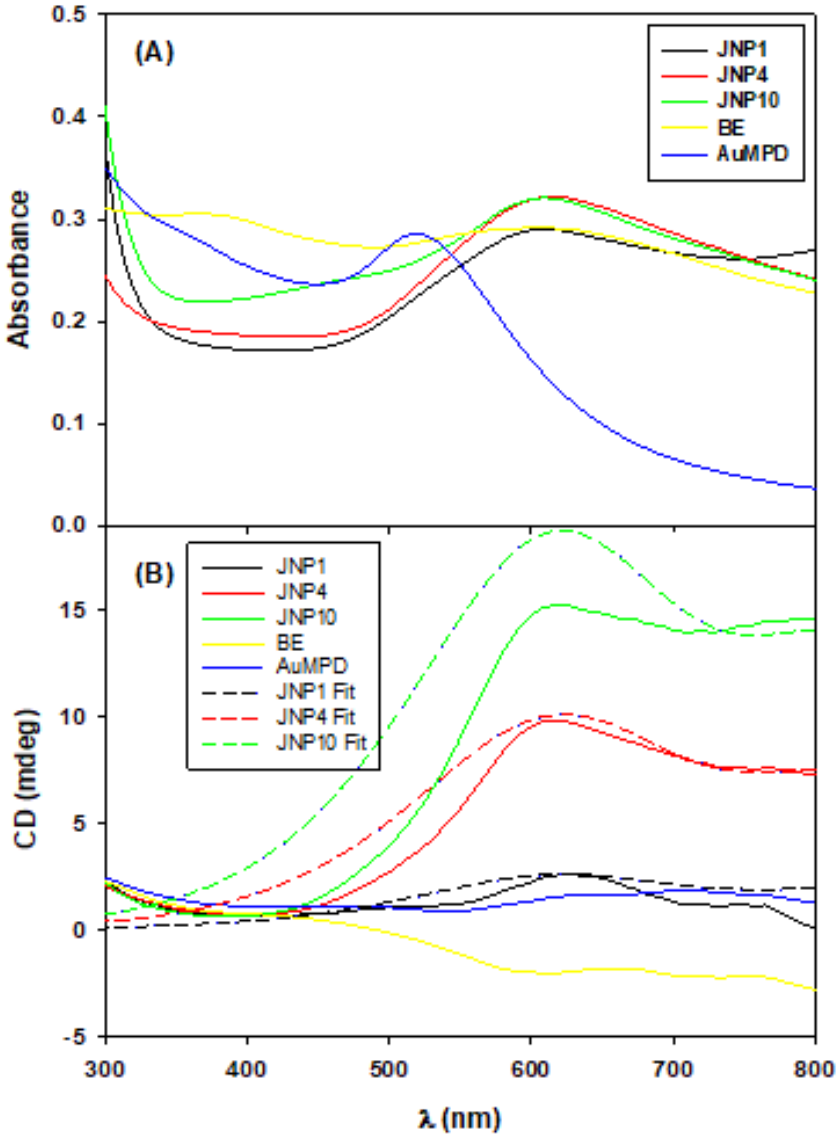

Figure 2.6 (A) UV-vis and (B) CD spectra of JNP, BE and AuMPD nanoparticles at a concentration of 0.15 mg mL^{-1} in water. The dashed curves in (B) are the fitting CD spectra of a hollow sphere (dia. 50 nm) consisting of Janus nanoparticles (core dia. 1.6 nm) by eqn (17).

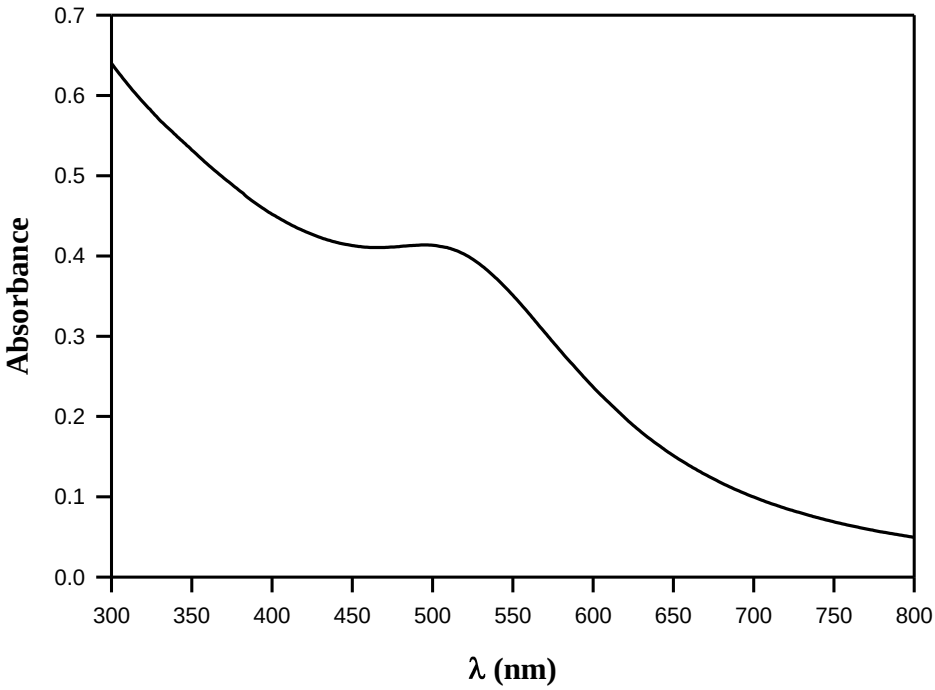

Figure 2.7 UV-vis absorption spectrum of AuC6 nanoparticles in $CHCl_3$.

Interestingly, the three JNP ensembles all exhibited apparent PCD signals at wavelength greater than 500 nm (**Figure 2.6B**), with the intensity maxima matching the corresponding SPR peaks (Figure 2A), and the PCD intensity increased with increasing MPD coverage on the nanoparticle surface, +2.6 mdeg for JNP1, +9.9 mdeg for JNP4 and +15.2 mdeg for JNP10. This result indicates that increasing dissymmetry of the distribution of surface capping ligands facilitates the formation of vesicle-like, hollow nanostructures that are PCD-active. By contrast, BE nanoparticles, exhibited only a weak PCD signal (ca. –2.05 mdeg), despite a ligand composition and SPR absorption similar to that of JNP10, suggesting that solid ensembles of the nanoparticles were PCD-inactive. This also suggests minimal contributions from the (racemic) MPD ligands to the

PCD signals of the JNPs, as control experiment with AuMPD nanoparticles exhibited virtually no PCD signals.

Furthermore, one can see that the PCD intensity of the JNP samples varied with nanoparticle concentration. As noted earlier, formation of nanoparticle ensembles occurs only when the JNP concentration reaches a minimum threshold (i.e., CMC).[34] **Figure 2.8** shows the CD spectra of the JNP10 nanoparticles at varied concentrations in water. It can be seen that at concentrations below 0.025 mg/mL (yellow, blue and magenta curves), the nanoparticles exhibited virtually no PCD absorption, most likely because in these dilute solutions, no nanoparticle ensembles were formed (Figure 1A), and individual nanoparticles were largely PCD-inactive because of plane symmetry. Yet at concentrations higher than 0.05 mg/mL, apparent PCD signals started to emerge and the intensity increased with nanoparticle concentration, indicating that the nanoparticle concentration was sufficiently high for the formation of organized assemblies and the ensembles were optically chiral. For instance, JNP10 nanoparticles showed a broad PCD absorption at 610 nm of +6.1 mdeg at 0.05 mg/mL (green curve), +7.1 mdeg at 0.075 mg/mL (red curve), and +15.2 mdeg at 0.15 mg/mL (black curve).[13] Notably, the PCD intensity observed here with the JNP10 ensembles was ca. 20 times stronger than that of simple nanoparticle dimers, trimers and tetramers reported in earlier studies.[37,38] This further confirms that the PCD effects were primarily due to the formation of vesicle-like nanostructures by JNP self-assembly. Furthermore, based on the

variation of the PCD intensity with nanoparticle concentration, the CMC of the JNP10 nanoparticles can be estimated to be ca. 0.05 mg/mL (0.86 μM), very close to that determined previously by Raman measurements.[34]

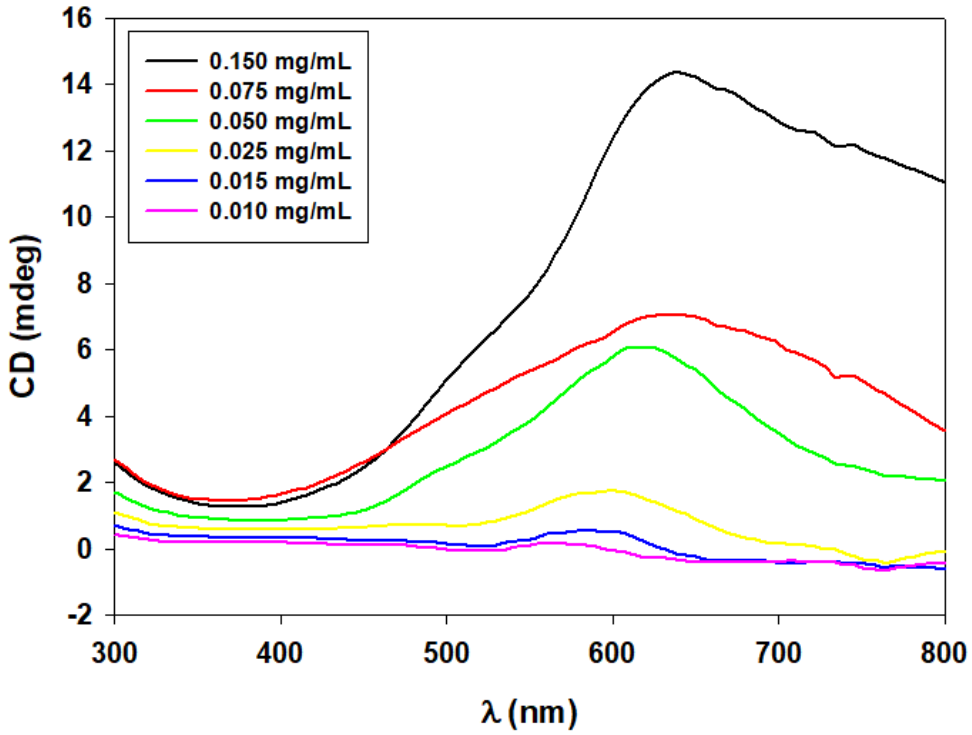

Figure 2.8 CD spectra of JNP10 nanoparticles at various concentrations in water.

To the best of our knowledge, this is the first ever observation of PCD with hollow nanoparticle ensembles formed by template-less self-assembly. To unravel the microscopic origin of PCD, we carried out first principles calculations of a gold JNP capped with C6 and MPD. Because of asymmetrical distribution of the hydrophobic (C6) and hydrophilic (MPD) ligands, the JNP is anticipated to exhibit a nonzero dipole. Linear response time-dependent density functional theory (TD-DFT) simulations of a Au_{20} cluster capped with either one

or two ligands indeed show a clear ligand-to-metal cluster transition by photoexcitations (**Figures 2.9-2.12**), consistent with results reported previously.[39] This suggests that the segregated distribution of organic capping ligands introduces directionality in the transition dipole moment of the cluster.

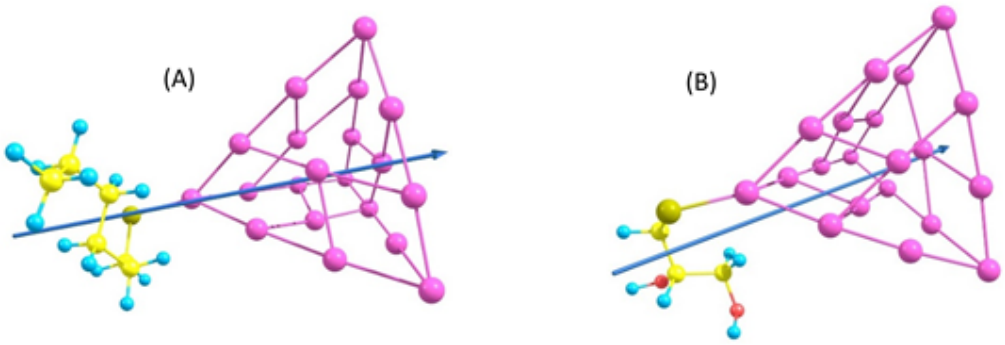

Figure 2.9 Transition dipole in an Au_{20} cluster capped with (A) C6 and (B) MPD. The excitation energies are 776 and 836 nm, respectively. It can be seen that adding ligands introduces directionality for the transition dipole moments.

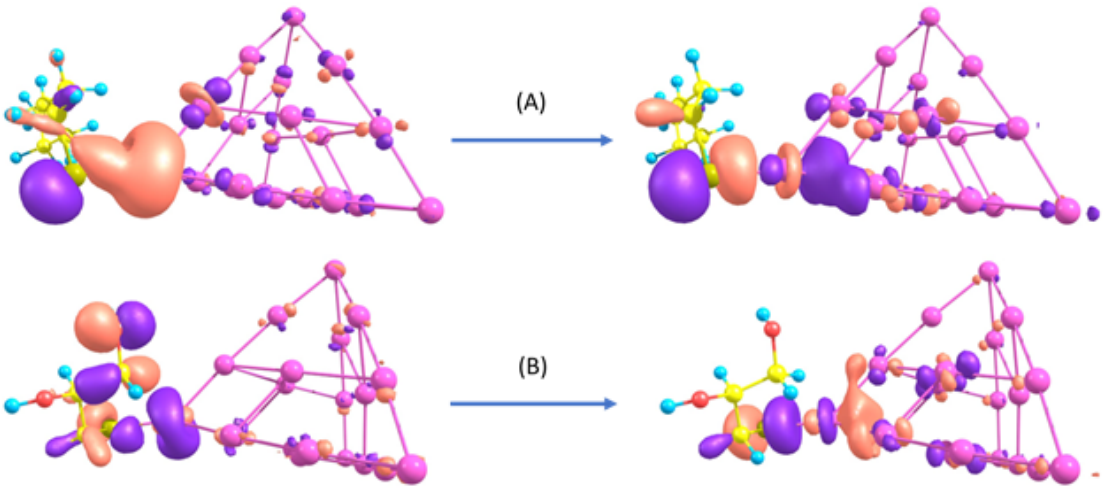

Figure 2.10 Transition of excited state in an Au_{20} cluster capped with (A) C6 and (B) MPD. The excited state transitions are visualized from molecular orbitals for the gold cluster linked with (A) one C6 and (B) one MPD, respectively. Both show that transitions occur approximately from ligand to gold cluster.

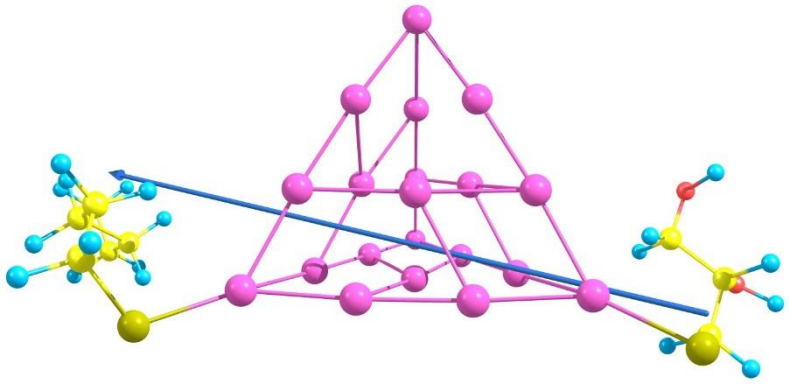

Figure 2.11 Transition dipole moment in an Au_{20} Janus cluster capped with C6 and MPD.

Figure 2.12 Transition of excited state in an Au_{20} Janus cluster capped with C6 and MPD.

We then investigated a more realistic model of the experimental JNPs, as illustrated in **Scheme 1**, where an Au_{147} cluster (dia. 1.6 nm)[40] was capped with 11 C6 and 11 MPD ligands. Since many more ligands and excited states are involved here, we are interested in a more averaged description for the absorption process. Real time time-dependent density functional tight-binding (TD-DFTB) simulations were carried out. Fourier transforms of the linear response function give the absorption spectra for all excitation transitions of interest. The results (**Figure 2.13**) show that the absorbance along the *x*-axis was an order of

magnitude higher than those along the y- and z-axes. This clearly indicates the average orientation of the transition dipole moment in this range of the spectra (**Scheme 1**).

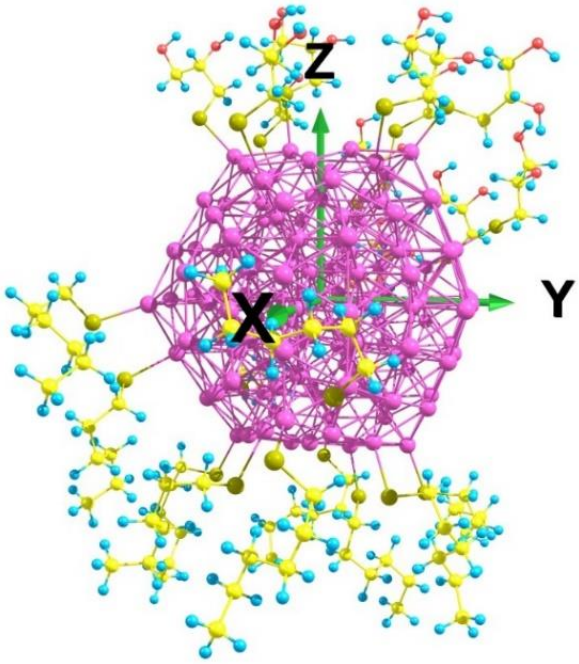

Scheme 1. Ground-state geometry of a JNP optimized by DFTB calculations, where an Au_{147} core is capped with 11 C6 and 11 MPD ligands on the two opposite hemispheres.

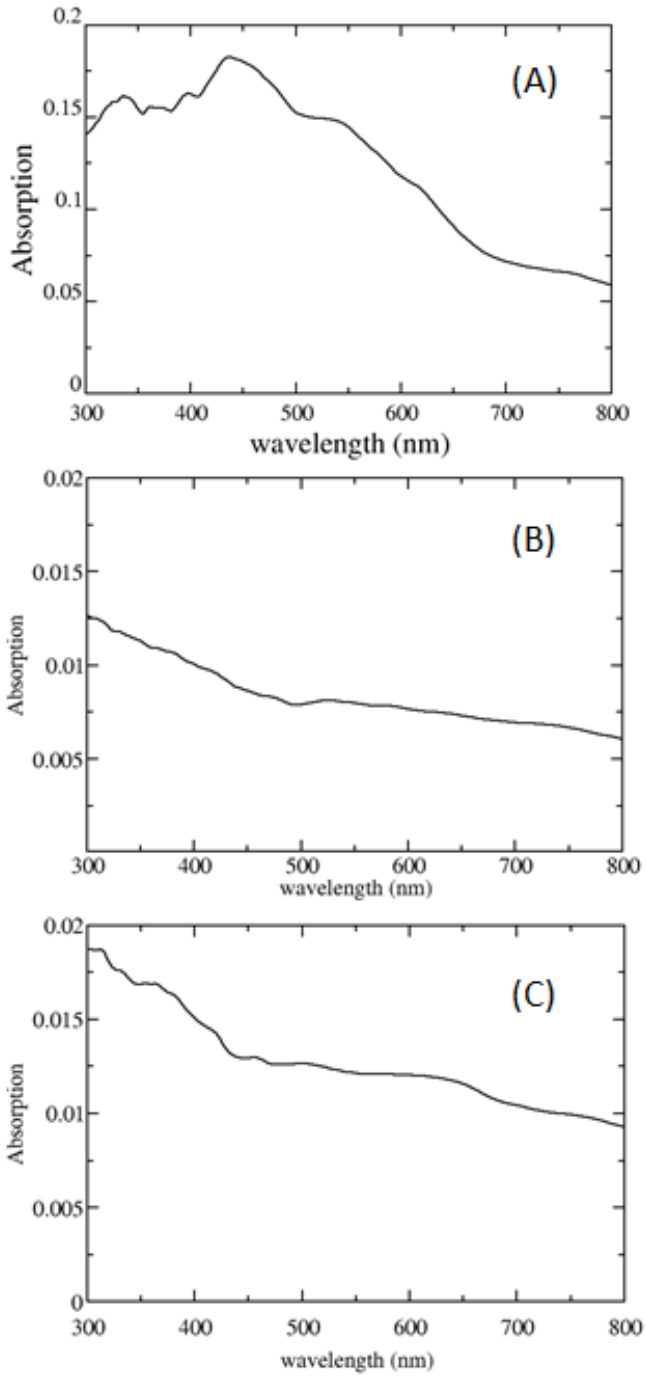

Figure 2.13 Absorption spectra with external field applied along the (A) x-axis, (B) y-axis, and (C) z-axis. From the calculations one can see that the absorbance is higher by an order of magnitude when the external field is applied along the x-axis (Scheme 1).

Thus, the response of a JNP in the visible range can be modelled by an electric (transition) dipole $\boldsymbol{d}_m$. For a hollow sphere covered by JNPs, the interaction between any two JNP dipoles is

$$V_{nm} = \frac{1}{\varepsilon r_{nm}^5}[r_{nm}^2(\boldsymbol{d}_n \cdot \boldsymbol{d}_m) - 3(\boldsymbol{r}_{nm} \cdot \boldsymbol{d}_n)(\boldsymbol{r}_{nm} \cdot \boldsymbol{d}_m)] \quad (1)$$

where $\boldsymbol{r}_{nm}$ is the displacement between particles n and m. The Hamiltonian, $H = E\delta_{mn} + V_{mn}$, can be readily diagonalized, and the eigen states can be expressed in terms of the linear combination of ψn for an isolated dipole,

$$\Psi_\mu = \sum_{n=1}^{N} c_{\mu n}\psi_n. \quad (2)$$

The CD strength (R_μ) for the μ[th] state can be calculated from

$$R_\mu \propto Re < \Psi_g|\boldsymbol{p}|\Psi_g > \cdot < \Psi_\mu|\boldsymbol{r} \times \boldsymbol{p}|\Psi_g > \quad (3)$$

where Ψ_g and Ψ_μ represent the ground state and excited states, respectively. Note that as $\langle \Psi_g|\boldsymbol{p}|\psi_n\rangle \propto \boldsymbol{d}_n$, we can express the CD strength as[41]

$$R_\mu \propto \sum_{mn} c_{\mu m}c_{\mu n}(\boldsymbol{d}_n \cdot [\boldsymbol{r}_m \times \boldsymbol{d}_m]) \propto \sum_{mn}(\boldsymbol{d}_n \cdot [\boldsymbol{r_m} \times \boldsymbol{d}_m]). \quad (4)$$

Based on the experimental data (**Figure 2.2B**), we consider a hollow sphere with JNPs homogeneously distributed on the surface (**Scheme 2A**). Each Janus particle is considered as a dipole, and the location of the m^{th} dipole is

$$\boldsymbol{r}_m = (sin\theta_m cos\varphi_m, sin\theta_m sin\varphi_m, cos\theta_m)^T. \quad (5)$$

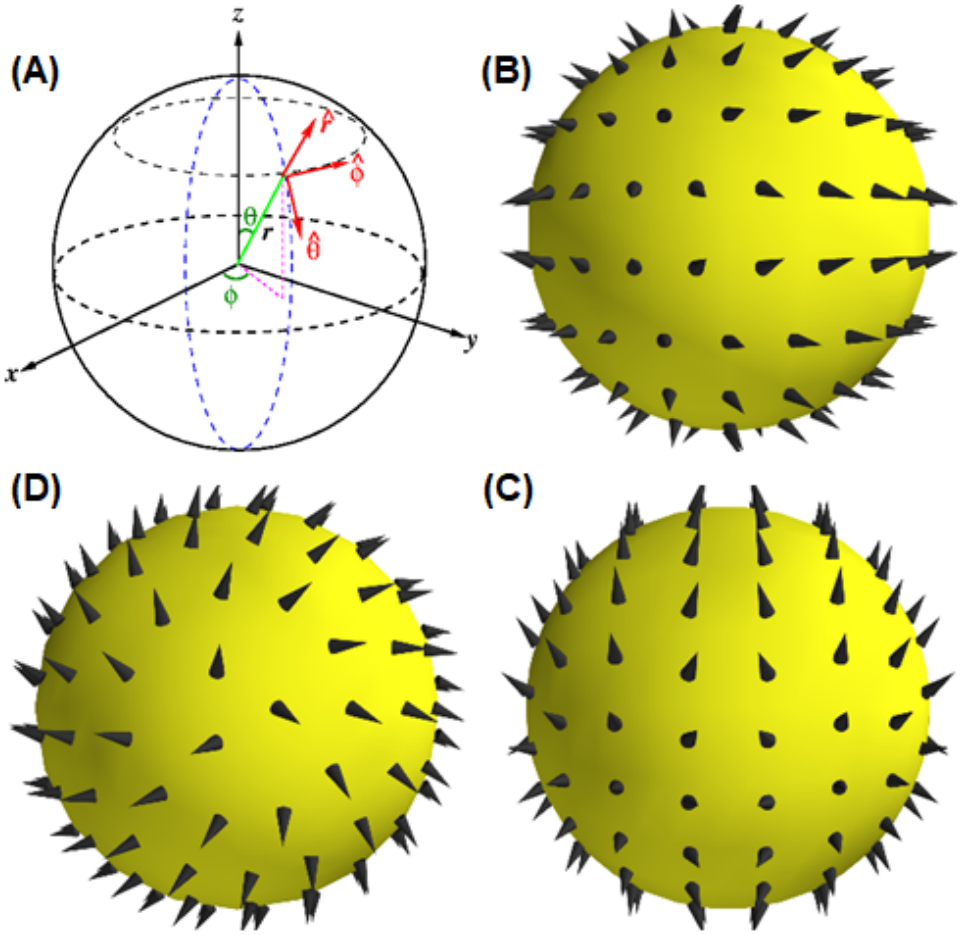

Scheme 2. Schematic of (A) JNPs on a hollow sphere surface, and the arrangements of JNP dipoles (represented by black thorns) along the (B) x, (C) y, and (D) z directions.

At this point, the three orthogonal unit vectors (**Scheme 2A**) are

$$\hat{\boldsymbol{r}}_m = \begin{pmatrix} sin\theta_m cos\varphi_m \\ sin\theta_m sin\varphi_m \\ cos\theta_m \end{pmatrix}, \hat{\boldsymbol{\theta}}_m = \begin{pmatrix} cos\theta_m cos\varphi_m \\ cos\theta_m sin\varphi_m \\ -sin\theta_m \end{pmatrix}, \hat{\boldsymbol{\varphi}}_m = \begin{pmatrix} -sin\varphi_m \\ cos\varphi_m \\ 0 \end{pmatrix} \quad (6)$$

and the dipole $\boldsymbol{d}_m$ can be expressed as a linear combination of these vectors,

$$\boldsymbol{d_m} = \alpha_m \hat{\boldsymbol{r}}_m + \beta_m \hat{\boldsymbol{\theta}}_m + \gamma_m \hat{\boldsymbol{\varphi}}_m. \quad (7)$$

Since the dipoles are uniformly distributed, it is reasonable to assume that the dipoles exist at both $\boldsymbol{r}_m$ and its inversion site, $-\boldsymbol{r}_m$. For $-\boldsymbol{r}_m$, its polar and azimuthal angles are $\pi - \theta_m$ and $\pi + \varphi_m$, respectively. Therefore, at $-\boldsymbol{r}_m$, the local unit vectors are

$$\hat{\boldsymbol{r}}'_m = -\hat{\boldsymbol{r}}_m,\ \widehat{\boldsymbol{\theta}}'_m = \widehat{\boldsymbol{\theta}}_m,\ \widehat{\boldsymbol{\varphi}}'_m = -\widehat{\boldsymbol{\varphi}}_m \tag{8}$$

and the dipole at $-\boldsymbol{r}_m$ is

$$d'_m\ = -\alpha'_m\hat{\boldsymbol{r}}_m + \beta'_m\widehat{\boldsymbol{\theta}}_m - \gamma'_m\widehat{\boldsymbol{\varphi}}_m. \tag{9}$$

Now we examine the summation in eqn (4) and separate the points on a half sphere from their inversions,

$$\begin{aligned} R_\mu \propto \textstyle\sum'_{nm}[\boldsymbol{r}_m \cdot (\boldsymbol{d_m} \times \boldsymbol{d}_n) - \boldsymbol{r}_m \cdot (\boldsymbol{d}'_m \times \boldsymbol{d}_n) + \boldsymbol{r}_m \cdot (\boldsymbol{d}_m \times \boldsymbol{d}'_n) - \boldsymbol{r}_m \cdot (\boldsymbol{d}'_m \times \boldsymbol{d}'_n) \\ = \textstyle\sum'_{nm}\{[\boldsymbol{r}_m \times (\boldsymbol{d_m} - \boldsymbol{d}'_m)] \cdot (\boldsymbol{d}_n + \boldsymbol{d}'_n)\} \end{aligned} \tag{10}$$

where the summation over m and n is limited to the half sphere. Using the relations

$$\hat{\boldsymbol{r}}_m \times \widehat{\boldsymbol{\theta}}_m \mathrel{\widehat{=}} \widehat{\boldsymbol{\varphi}}_m,\ \ \hat{\boldsymbol{r}}_m \times \widehat{\boldsymbol{\varphi}}_m \mathrel{\widehat{=}} -\widehat{\boldsymbol{\theta}}_m \tag{11}$$

we have

$$\begin{aligned} R_\mu &\propto \textstyle\sum'_{nm}\{[\boldsymbol{r}_m \times (\boldsymbol{d_m} - \boldsymbol{d}'_m)] \cdot (\boldsymbol{d}_n + \boldsymbol{d}'_n)\} \\ &= r_o \textstyle\sum'_{nm}[(\alpha_n - \alpha'_n)\hat{\boldsymbol{r}}_n + (\beta_n + \beta'_n)\widehat{\boldsymbol{\theta}}_n + (\gamma_n - \gamma'_n)\widehat{\boldsymbol{\varphi}}_n] \cdot [(\beta_m - \beta'_m)\widehat{\boldsymbol{\theta}}_m - \\ &\qquad (\gamma_m + \gamma'_m)\widehat{\boldsymbol{\varphi}}_m] \end{aligned} \tag{12}$$

From the above expression, it is clear that to have nonzero chirality R_μ, the dipoles cannot be all along $\hat{\boldsymbol{r}}_m$ and must have components along $\widehat{\boldsymbol{\theta}}_m$ and $\widehat{\boldsymbol{\varphi}}_m$. If we set α_m =

$\alpha'_m = \alpha$, *i.e.*, the dipoles tend to point either outward or inward, to have a finite R_μ, the simplest solutions are $\beta_m = \beta'_m = \beta$ and $\gamma_m = \gamma'_m = \gamma$, where $\pi < \phi'_m < 2\pi$ and

$$R_\mu \propto -4\beta\gamma \sum'_{nm} [\cos\theta_n cos\theta_m cos(\varphi_n - \varphi_m) + \sin\theta_n sin\theta_m]$$
$$= -4\beta\gamma \sum'_{nm} \sin\theta_n sin\theta_m. \quad (13)$$

As sin θ_m and sin θ_n are always positive, the dipoles along a latitude circle form a vortex-like structure (**Scheme 2B–D**). The fixed sign in β and γ is due to the slightly preferred dipolar orientations between adjacent JNPs.

For monofunctionalized AuC6 and AuMPD nanoparticles, the dipole moment associated with individual nanoparticles is anticipated to be essentially zero; so are the BE nanoparticles. Yet, for AuC6-MPD JNPs, non-zero nanoparticle dipole arises due to the asymmetric segregation of the C6 and MPD ligands, and increases with an increasing number of C6 ligands replaced with MPD on the nanoparticle surface. That is, the dipole moment increases in the order of JNP1 < JNP4 < JNP10. We will establish a quantitative relation between the MPD coverage and the nanoparticle dipole moment. If we arrange the ligands in such a way that the MPD ligands are located in the range of $\theta \in [0, \theta_o]$ (Scheme 2), the MPD coverage f is then defined as

$$f = \frac{2\pi R^2 \int_0^{\theta_o} sin\theta d\theta}{2\pi R^2 \int_0^{\pi} sin\theta d\theta} = \frac{1}{2}(1 - cos\theta_o) \quad (14)$$

where R is the radius of the nanoparticle. Thus, from the surface coverage f, we can obtain θ_o. Correspondingly, the C6 ligands will be located in the range of $\theta \in [\theta_o, \pi]$.

Now if we denote the dipole densities in the MPD region and in the C6 regions as p_M and p_C, respectively, the effective dipole moment of the nanoparticle, which is oriented along the *z*-axis, is

$$\boldsymbol{d} = 2\pi R^2 \boldsymbol{e}_z \int_0^{\pi} p(\theta) cos\theta sin\theta d\theta \tag{15}$$

where $p(\theta)$ is the dipole density as a function of θ, $p(\theta) = p_M$ for $\theta \in [0, \theta_o]$, and $p(\theta) = p_C$ for $\theta \in [\theta_o, \pi]$, with the ligands assumed to be normal to the nanoparticle surface contributing the cos θ factor in eqn (15). Therefore, we have

$$\boldsymbol{d} = 2\pi R^2 (1 - cos^2\theta_o)(p_M - p_C). \tag{16}$$

This expression indicates that at $\theta_o = 0$ or π, *i.e.*, the nanoparticle is fully covered by only one kind of ligand, $\boldsymbol{d} = 0$.

For a given dipole distribution, the Hamiltonian $H = E\delta_{mn} + V_{mn}$ can then be diagonalized and the CD spectrum can be computed, according to eqn (4). Due to the weak interactions between JNPs, we consider a largely random distribution for the dipole vectors in hollow nanoparticle ensembles, which, however, contains a small portion of a vertex pattern, as depicted above in **Scheme 2B–D**. To satisfactorily model the experimentally observed CD spectra, we consider a three-level system (two resonant energies). Since the resonant energy E appears only in the diagonal terms in the Hamiltonian, for a given dipole distribution, the eigen values δE_μ and functions Ψ_μ can be obtained by setting $E = 0$. Then the eigen values of the system are $E_\mu = E + \delta E_\mu$ and $E'_\mu = E + \delta E_\mu$, where E and E' are the two resonant energies of an isolated

nanoparticle. In addition, we include the level broadening γ and γ' for the levels associated with E and E'. Finally, the CD signal at frequency ω is calculated from

$$CD(\omega) = \frac{1}{\pi}\sum_{\mu} R_{\mu}\left[\frac{\gamma}{(\hbar\omega - E_{\mu})^2 + \gamma^2} + \frac{\gamma'}{(\hbar\omega - E'_{\mu})^2 + \gamma'^2}\right]. \quad (17)$$

Experimentally, in the self-assembly into vesicle-like, hollow nanostructures, the JNP dipoles are most likely pointed either inward or outward, akin to conventional vesicles formed by surfactant molecules (**Figure 2.2B** inset). Therefore, based on eqn (13), this leads to an effective vertex arrangement of the JNP dipoles on the surface of a hollow sphere (**Scheme 2**) and hence the appearance of PCD signals. In fact, the CD profiles of the three JNP samples can be quantitatively fitted by using eqn (17) at E = 1.25 eV, E' = 1.75 eV, γ = 0.4 eV, and γ' = 0.58 eV, as manifested by the dashed curves in **Figure 2.6B**. Furthermore, from the MPD coverage f in JNP1, JNP4, and JNP10 (**Figure 2.3**), the nanoparticle dipole moment d can also be quantified, according to eqn (14), at 0.578, 0.812, and 0.948Do, respectively, where Do is the dipole moment of a perfect JNP (*i.e.*, exactly 50% each of C6 and MPD). This is consistent with the enhanced asymmetry (dipole) of the JNPs with an increasing number of polar MPD ligands incorporated onto the nanoparticle surface.

With such remarkable chirality of the vesicle-like nanostructures of JNPs, the hollow interiors can be exploited as a nanoscale vehicle for enantioselective phase transfer of chiral molecules,[32] leading to ready separation of optical isomers.[42] We used alanine as the illustrating example. Experimentally, JNP10 nanoparticles were dispersed at a concentration of 0.15 mg/mL in $CHCl_3$ and

mixed with aqueous solutions of alanine enantiomers, and the organic nanoparticle layer was monitored by CD measurements. From **Figure 2.14**, it can be seen that JNP10 nanoparticles exhibited a PCD profile in $CHCl_3$ similar to that in H_2O before mixing with alanine (**Figures 2.6 and 2.8**) with a positive peak of +13.9 mdeg at 606 nm, suggesting that both vesicle- and reverse vesicle-like structures of the JNPs followed the same patterns of nanoparticle organization (black curve, **Scheme 2**). After mixing with L-Ala in water, CD measurements of the $CHCl_3$ layer showed virtually no change (red curve), indicating a lack of interactions between the JNP10 nanoparticles and L-Ala (peak intensity decreased only slightly to +12.9 mdeg). However, mixing with D-Ala led to a drastic change of the nanoparticle PCD response (green curve), where the CD peak actually became negative (–8.3 mdeg). It has been known that a chiral structure is more likely to interact with molecules of opposite chirality because it provides a better "groove" for the adsorption.[42] This implies that the chirality of the JNP10 nanoparticle ensembles was equivalent to that of an L enantiomer. In addition, the change of sign of the PCD signals upon interaction with D-Ala is likely due to the physical confinement of the D-Ala molecules within the nanoscale hollow interior of the JNP vesicles, such that they behaved analogously to D-Ala crystals where negative CD absorption is generally observed and may be enhanced by nanoparticle SPR.[43]

Such a unique property can be exploited for the separation of the D and L enantiomers. In fact, after mixing with a mixture of D- and L-Ala (yellow curve), the

PCD profile of the nanoparticle layer resembles that with D-Ala alone, displaying a peak intensity of −4.8 mdeg. This suggests selective interactions of the JNP ensembles with the D enantiomer but not the L counterpart.

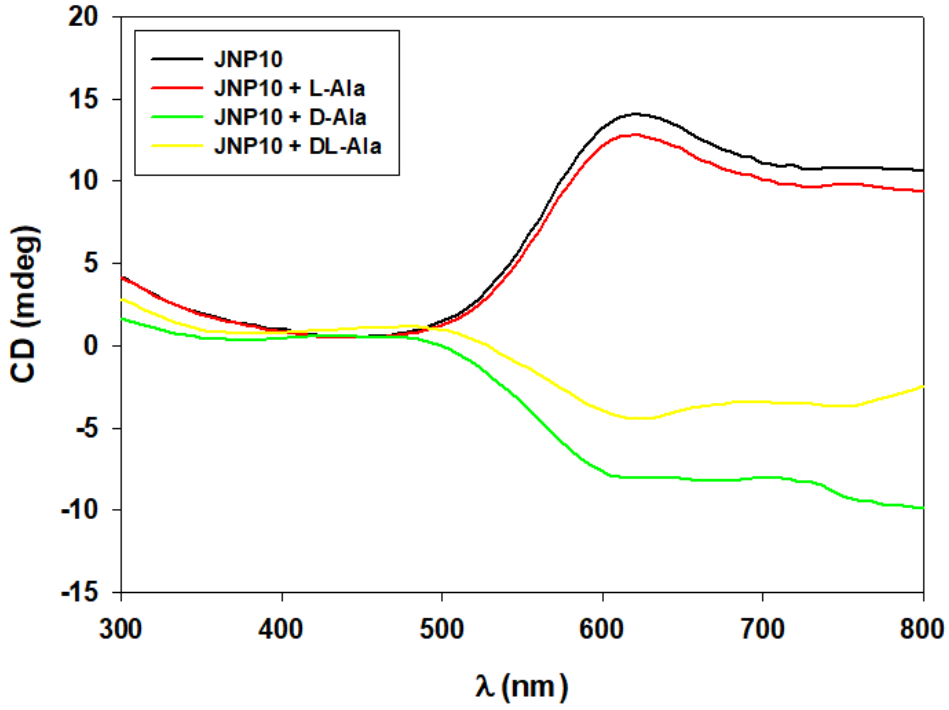

Figure 2.14 CD spectra of JNP10 nanoparticles in $CHCl_3$ before and after mixing with L-alanine, D-alanine, or D,L-alanine in water. Nanoparticle concentration 0.15 mg mL−1 and alanine concentration 0.1 M.

2.4 Conclusion

In summary, AuC6-MPD JNPs were prepared by interfacial ligand exchange reactions of AuC6 nanoparticles with MPD ligands. The resulting JNPs formed (reverse) vesicle-like organized ensembles in water and apolar organic media at sufficiently high concentrations, which exhibited apparent PCD absorption. The PCD intensity was found to increase with increasing nanoparticle concentration.

This was accounted for by the template-less self-assembly of JNP dipoles into a vesicle-like, hollow structure, where a dipole vertex was formed, as manifested in theoretical simulations based on first principles calculations. By contrast, no PCD signals were observed with individual nanoparticles or solid ensembles produced with the bulk-exchange counterparts. Remarkably, the Janus nanoparticle ensembles showed high enantioselectivity towards D-alanine, rather than the L enantiomer, a unique property that may be exploited for nanoparticle-based separation of optical isomers and biosensing.[44]

2.5 Experimental Section

Chemicals. Hydrogen tetrachloroauric acid trihydrate ($HAuCl_4 \cdot 3H_2O$, Fisher Scientific, 99%), tetra-*n*-octylammonium bromide (TOABr, Alfa Aesar, 98%), 1-hexanethiol (C6SH, Acros, 96%), sodium borohydride ($NaBH_4$, Acros, 99%), racemic 3-mercapto-1, 2-propanediol (MPD, Aldrich, 95%), L-alanine (L-Ala, Acros, 99%), D-alanine (D-Ala, Acros, +99%), and D,L-alanine (D,L-Ala, Acros, 99%) were used as received. All solvents were purchased from commercial sources at their highest purities and used without further treatment. Water was supplied by a Barnstead Nanopure water system (18.3 MΩ·cm).

Preparation of gold nanoparticles protected by C6SH (AuC6) and MPD (AuMPD) ligands. AuC6 nanoparticles were synthesized by using the Brust method.[45] In a typical reaction, 30 mL of an aqueous $HAuCl_4$ solution (0.03 M) was mixed with 20 mL of TOABr in toluene (0.20 M) under vigorous stirring

for 1 h. The orange organic phase was then collected, into which was injected 150 μL (1.05 mmol) of C6SH with a micropipette (Accumax Pro) under magnetic stirring, and the solution became colorless. The addition of 24 mL of a chilled aqueous $NaBH_4$ solution (0.43 M) into the solution led to the rapid appearance of a dark brown color, indicating the formation of gold nanoparticles. The reaction mixture was stirred for 4 h before the organic phase was collected, dried by rotary evaporation, and washed five times with methanol to remove excess C6SH, phase-transfer catalysts, and reaction byproducts. The resulting AuC6 nanoparticles exhibited an average core diameter of 2.7 ± 0.4 nm, as determined by TEM measurements (Figure S1).

AuMPD nanoparticles were prepared in a similar fashion except that an equivalent amount of MPD was used instead of C6SH.

Preparation of AuC6-MPD Janus nanoparticles (JNPs). The synthesis of AuC6-MPD Janus nanoparticles has been detailed previously.[30-32] Briefly, the AuC6 nanoparticles prepared above were dispersed in toluene and deposited onto the water surface of a Langmuir-Blodgett trough (NIMA 611D). After evaporation of the organic solvent, the nanoparticle monolayer was compressed to a desired surface pressure such that the interparticle spacing was less than twice the fully extended chain length of the C6SH ligands. A calculated amount of MPD was then injected into the water subphase using a micropipette to initiate interfacial ligand exchange reactions. The resulting particles were collected after various reaction times (i.e., 1, 4, or 10 h) so as to vary the concentration of the

MPD ligands onto the nanoparticle surface. The nanoparticles were then collected from the water surface and washed by methanol. The resulting Janus nanoparticles were referred to as JNP1, JNP4 and JNP10, respectively.

As a control experiment, ligand exchange reactions were also carried out by simply mixing both the AuC6 nanoparticles and MPD in THF for 10 h, and the resulting sample was denoted as bulk exchange (BE) nanoparticles.

Phase transfer of alanine by JNPs. In a typical experiment, JNP10 was dispersed in chloroform at a concentration of 0.15 mg/mL, and alanine (L-Ala, D-Ala, or D,L-Ala) was dissolved in water at a concentration of 10 mM. The two solutions were mixed under gentle magnetic stirring for 30 min before an aliquot of the $CHCl_3$ phase was pipetted for CD measurements.

Characterization. Transmission electron microscopy (TEM) studies were carried out with a Philips CM300 microscope operated at 300 kV, and atomic force microscopic (AFM) studies were performed with a Molecular Imaging PicoLE SPM instrument. UV-vis absorption spectra were acquired using a PerkinElmer Lambda 35 UV/Vis Spectrometer with a 1 cm quartz cuvette. FTIR measurements were carried out with a PerkinElmer Spectrum One spectrometer. Proton nuclear magnetic resonance (^{1}H NMR) measurements were conducted with a Varian Unity 500 MHz spectrometer with the samples dissolved in deuterated chloroform ($CDCl_3$). Circular dichroism (CD) measurements were carried out with a JASCO J1500 CD spectrometer using a 1 cm quartz cuvette.

Computational methods. Two models were used in the calculations, one for a small cluster where a more accurate theory was applied, and a large cluster to model the realistic Janus nanoparticle. The small cluster model contained an Au_{20} core and two ligands, i.e., one C6 and one MPD. The larger cluster model contained an Au_{147} core capped with eleven C6 and eleven MPD ligands. This model has approximately the size of the Janus particle used in the experiment.

We performed density function theory (DFT) calculations for the small cluster. The ground state geometry optimization was performed using the hybrid B3LYP functional and the 6-31G* basis set for all elements except for gold atoms where an effective core potential LANL2DZ was used (denoted as B3LYP/6-31G*-LANL2DZ). To investigate the excited electronic state, we applied linear response time-dependent DFT (TD-DFT) method at the CAM-B3LYP/6-31G*-LANL2DZ level of theory. The calculations were carried out using the Q-Chem 5.0 program package.

For the larger model system, the ground state geometry optimization was carried out employing the density functional tight-binding (DFTB) approach and the SK parameters were used as aurog-1-1 in the DFTB+ program. To investigate electronic excited states, we performed real time TD-DFTB method using the lodestar program package. Fourier transform was then used to obtain the absorption spectra.

2.6 References

(1) Kumar, J.; Thomas, K. G.; Liz-Marzan, L. M. Nanoscale chirality in metal and semiconductor nanoparticles. *Chem Commun* **2016**, *52*, 12555-12569.

(2) Ma, W.; Xu, L. G.; de Moura, A. F.; Wu, X. L.; Kuang, H.; Xu, C. L.; Kotov, N. A. Chiral Inorganic Nanostructures. *Chemical Reviews* **2017**, *117*, 8041-8093.

(3) Gao, F. L.; Sun, M. Z.; Ma, W.; Wu, X. L.; Liu, L. Q.; Kuang, H.; Xu, C. L. A Singlet Oxygen Generating Agent by Chirality-dependent Plasmonic Shell-Satellite Nanoassembly. *Advanced Materials* **2017**, *29*.

(4) Ranjbar, B.; Gill, P. Circular Dichroism Techniques: Biomolecular and Nanostructural Analyses- A Review. *Chem Biol Drug Des* **2009**, *74*, 101-120.

(5) Berova, N.; Di Bari, L.; Pescitelli, G. Application of electronic circular dichroism in configurational and conformational analysis of organic compounds. *Chem Soc Rev* **2007**, *36*, 914-931.

(6) George, J.; Thomas, K. G. Surface Plasmon Coupled Circular Dichroism of Au Nanoparticles on Peptide Nanotubes. *Journal of the American Chemical Society* **2010**, *132*, 2502-+.

(7) Shemer, G.; Krichevski, O.; Markovich, G.; Molotsky, T.; Lubitz, I.; Kotlyar, A. B. Chirality of silver nanoparticles synthesized on DNA. *J Am Chem Soc* **2006**, *128*, 11006-11007.

(8) Fan, Z. Y.; Govorov, A. O. Chiral Nanocrystals: Plasmonic Spectra and Circular Dichroism. *Nano Letters* **2012**, *12*, 3283-3289.

(9) Frank, B.; Yin, X. H.; Schaferling, M.; Zhao, J.; Hein, S. M.; Braun, P. V.; Giessen, H. Large-Area 3D Chiral Plasmonic Structures. *Acs Nano* **2013**, *7*, 6321-6329.

(10) Esposito, M.; Tasco, V.; Todisco, F.; Cuscuna, M.; Benedetti, A.; Scuderi, M.; Nicotra, G.; Passaseo, A. Programmable Extreme Chirality in the Visible by Helix-Shaped Metamaterial Platform. *Nano Lett* **2016**, *16*, 5823-5828.

(11) Esposito, M.; Tasco, V.; Todisco, F.; Cuscuna, M.; Benedetti, A.; Sanvitto, D.; Passaseo, A. Triple-helical nanowires by tomographic rotatory growth for chiral photonics. *Nat Commun* **2015**, *6*.

(12) Hidalgo, F.; Sanchez-Castillo, A.; Garzon, I. L.; Noguez, C. First-principles calculations of circular dichroism of ligand-protected gold nanoparticles. *Eur Phys J D* **2009**, *52*, 179-182.

(13) Roman-Velazquez, C. E.; Noguez, C.; Garzon, I. L. Circular dichroism simulated spectra of chiral gold nanoclusters: A dipole approximation. *Journal of Physical Chemistry B* **2003**, *107*, 12035-12038.

(14) Hidalgo, F.; Noguez, C.; de la Cruz, M. O. Metallic influence on the atomic structure and optical activity of ligand-protected nanoparticles: a comparison between Ag and Au. *Nanoscale* **2014**, *6*, 3325-3334.

(15) Sanchez-Castillo, A.; Noguez, C.; Garzon, I. L. On the origin of the optical activity displayed by chiral-ligand-protected metallic nanoclusters. *J Am Chem Soc* **2010**, *132*, 1504-1505.

(16) Schaaff, T. G.; Whetten, R. L. Giant gold-glutathione cluster compounds: Intense optical activity in metal-based transitions. *Journal of Physical Chemistry B* **2000**, *104*, 2630-2641.

(17) di Gregorio, M. C.; Ben Moshe, A.; Tirosh, E.; Galantini, L.; Markovich, G. Chiroptical Study of Plasmon-Molecule Interaction: The Case of Interaction of Glutathione with Silver Nanocubes. *Journal of Physical Chemistry C* **2015**, *119*, 17111-17116.

(18) Hou, S.; Yan, J.; Hu, Z. J.; Wu, X. C. Enhancing the plasmonic circular dichroism by entrapping chiral molecules at the core-shell interface of rod-shaped Au@Ag nanocrystals. *Chem Commun* **2016**, *52*, 2059-2062.

(19) Sun, M. Z.; Xu, L. G.; Banhg, J. H.; Kuang, H.; Alben, S.; Kotov, N. A.; Xu, C. L. Intracellular localization of nanoparticle dimers by chirality reversal. *Nat Commun* **2017**, *8*.

(20) Lan, X.; Wang, Q. Self-Assembly of Chiral Plasmonic Nanostructures. *Adv Mater* **2016**, *28*, 10499-10507.

(21) Rao, C. C.; Wang, Z. G.; Li, N.; Zhang, W.; Xu, X. C.; Ding, B. Q. Tunable optical activity of plasmonic dimers assembled by DNA origami. *Nanoscale* **2015**, *7*, 9147-9152.

(22) Fan, Z. Y.; Govorov, A. O. Plasmonic Circular Dichroism of Chiral Metal Nanoparticle Assemblies. *Nano Letters* **2010**, *10*, 2580-2587.

(23) Jung, S. H.; Jeon, J.; Kim, H.; Jaworski, J.; Jung, J. H. Chiral Arrangement of Achiral Au Nanoparticles by Supramolecular Assembly of Helical Nanofiber Templates. *J Am Chem Soc* **2014**, *136*, 6446-6452.

(24) Wang, R. Y.; Wang, H. L.; Wu, X. C.; Ji, Y. L.; Wang, P.; Qu, Y.; Chung, T. S. Chiral assembly of gold nanorods with collective plasmonic circular dichroism response. *Soft Matter* **2011**, *7*, 8370-8375.

(25) Droulias, S.; Yannopapas, V. Broad-Band Giant Circular Dichroism in Metamaterials of Twisted Chains of Metallic Nanoparticles. *Journal of Physical Chemistry C* **2013**, *117*, 1130-1135.

(26) Jarrett, J. W.; Zhao, T.; Johnson, J. S.; Liu, X. Y.; Nealey, P. F.; Vaia, R. A.; Knappenberger, K. L. Plasmon-Mediated Two-Photon Photoluminescence-Detected Circular Dichroism in Gold Nanosphere Assemblies. *J Phys Chem Lett* **2016**, *7*, 765-770.

(27) Shen, C. Q.; Lan, X.; Lu, X. X.; Ni, W. H.; Wang, Q. B. Tuning the structural asymmetries of three-dimensional gold nanorod assemblies. *Chemical Communications* **2015**, *51*, 13627-13629.

(28) Hou, S.; Zhang, H.; Yan, J.; Ji, Y. L.; Wen, T.; Liu, W. Q.; Hu, Z. J.; Wu, X. C. Plasmonic circular dichroism in side-by-side oligomers of gold nanorods: the influence of chiral molecule location and interparticle distance. *Phys Chem Chem Phys* **2015**, *17*, 8187-8193.

(29) Jin, X.; Jiang, J.; Liu, M. H. Reversible Plasmonic Circular Dichroism via Hybrid Supramolecular Gelation of Achiral Gold Nanorods. *Acs Nano* **2016**, *10*, 11179-11186.

(30) Pradhan, S.; Xu, L. P.; Chen, S. W. Janus nanoparticles by interfacial engineering. *Adv Funct Mater* **2007**, *17*, 2385-2392.

(31) Song, Y.; Klivansky, L. M.; Liu, Y.; Chen, S. W. Enhanced Stability of Janus Nanoparticles by Covalent Cross-Linking of Surface Ligands. *Langmuir* **2011**, *27*, 14581-14588.

(32) Song, Y.; Chen, S. W. Janus Nanoparticles as Versatile Phase-Transfer Reagents. *Langmuir* **2014**, *30*, 6389-6397.

(33) Song, Y.; Chen, S. W. Janus Nanoparticles: Preparation, Characterization, and Applications. *Chem-Asian J* **2014**, *9*, 418-430.

(34) Xu, Q.; Kang, X. W.; Bogomolni, R. A.; Chen, S. W. Controlled Assembly of Janus Nanoparticles. *Langmuir* **2010**, *26*, 14923-14928.

(35) Yang, Y.; Matsubara, S.; Nogami, M.; Shi, J. L.; Huang, W. M. One-dimensional self-assembly of gold nanoparticles for tunable surface plasmon resonance properties. *Nanotechnology* **2006**, *17*, 2821-2827.

(36) Ghosh, S. K.; Pal, T. Interparticle coupling effect on the surface plasmon resonance of gold nanoparticles: From theory to applications. *Chemical Reviews* **2007**, *107*, 4797-4862.

(37) Govorov, A. O.; Gun'ko, Y. K.; Slocik, J. M.; Gerard, V. A.; Fan, Z. Y.; Naik, R. R. Chiral nanoparticle assemblies: circular dichroism, plasmonic interactions, and exciton effects. *Journal of Materials Chemistry* **2011**, *21*, 16806-16818.

(38) Wang, Z. J.; Cheng, F.; Winsor, T.; Liu, Y. M. Optical chiral metamaterials: a review of the fundamentals, fabrication methods and applications. *Nanotechnology* **2016**, *27*.

(39) Ansar, S. M.; Perera, G. S.; Jiang, D. P.; Holler, R. A.; Zhang, D. M. Organothiols Self-Assembled onto Gold: Evidence for Deprotonation of the Sulfur-Bound Hydrogen and Charge Transfer from Thiolate. *Journal of Physical Chemistry C* **2013**, *117*, 8793-8798.

(40) Hostetler, M. J.; Wingate, J. E.; Zhong, C. J.; Harris, J. E.; Vachet, R. W.; Clark, M. R.; Londono, J. D.; Green, S. J.; Stokes, J. J.; Wignall, G. D.; Glish, G. L.; Porter, M. D.; Evans, N. D.; Murray, R. W. Alkanethiolate gold cluster molecules with core diameters from 1.5 to 5.2 nm: Core and monolayer properties as a function of core size. *Langmuir* **1998**, *14*, 17-30.

(41) Shlykov, A. I.; Baimuratov, A. S.; Baranov, A. V.; Fedorov, A. V.; Rukhlenko, I. D. Optically active quantum-dot molecules. *Optics Express* **2017**, *25*, 3811-3825.

(42) Gellman, A. J.; Huang, Y.; Feng, X.; Pushkarev, V. V.; Holsclaw, B.; Mhatre, B. S. Superenantioselective Chiral Surface Explosions. *J Am Chem Soc* **2013**, *135*, 19208-19214.

(43) Chen, H. Y.; Li, L.; Liu, D.; Huang, H. J.; Deng, J. P.; Yang, W. T. Optically active helical polyacetylene/Fe3O4 composite microspheres: prepared by precipitation polymerization and used for enantioselective crystallization. *Rsc Adv* **2014**, *4*, 63611-63619.

(44) Zhao, X. L.; Xu, L. G.; Sun, M. Z.; Ma, W.; Wu, X. L.; Xu, C. L.; Kuang, H. Tuning the interactions between chiral plasmonic films and living cells. *Nat Commun* **2017**, *8*.

(45) Brust, M.; Walker, M.; Bethell, D.; Schiffrin, D. J.; Whyman, R. Synthesis of Thiol-Derivatized Gold Nanoparticles in a 2-Phase Liquid-Liquid System. *J Chem Soc Chem Comm* **1994**, 801-802.

Chapter 3

Janus Nanoparticle Emulsions as Chiral Nanoreactors for Enantiomerically Selective Ligand Exchange

3.1 Abstract

Janus nanoparticles capped with a hydrophobic and hydrophilic hemisphere of mercapto ligands can self-assemble into hollow, emulsion-like nanostructures in controlled media. As the nanoparticle emulsions are chiroptically active exhibiting a plasmonic circular dichroism absorption in the visible range, they can be exploited as a unique chiral nanorector by selective encapsulation of D-enantiomer into the water phase of the water-in-oil emulsions for directional functionalization of the nanoparticles and endow the resulting nanoparticles with select chirality. This was demonstrated in the present study with gold Janus nanoparticles functionalized with (hydrophobic) hexanethiolates and (hydrophilic) 3-mercapto-1,2-propandiol, and D,L-cysteine was used as the molecular probe. Experimental results demonstrate that D-cysteine was the preferred enantiomers entrapped within the nanoparticle emulsions, where the ensuing ligand exchange reaction was initially confined to the hydrophilic face of the Janus nanoparticles. This suggests that with a deliberate control of the reaction time, chiral Janus nanoparticles could be readily prepared by ligand exchange reactions even with a racemic mixture of ligands.

3.2 Results and Discussion

Chiral metal nanoparticles represent a unique family of functional nanomaterials that has been attracting extensive interest because of their potential applications in diverse areas, such as sensing and catalysis for a specific enantiomer of interest.[1-8] The nanoparticle chiroptical properties have been observed to arise from the formation of a

chiral metal core and/or chiral organic capping ligands. The former can be achieved by using chiral templates (e.g., amino acids, DNA, etc) to direct the asymmetrical growth of the nanoparticle cores,[9-13] such that the resulting nanoparticles inherit the morphology and handedness from the chiral scaffolds. In the latter, chirality is produced by capping the nanoparticle cores with enantiomerically pure organic ligands. Yet, one may ask, is it possible to selectively functionalize nanoparticles with an enantiomer from a racemic mixture of ligands? This will significantly simplify the preparation procedure of chiroptically active nanoparticles. Such a deliberate selection of the organic capping ligands can be achieved by taking advantage of a chiral nanoreactor. In a previous study,[14] we observed that with hydrophobic (hexanethiolate, C6) ligands on one hemisphere and hydrophilic (3-mercapto-1,2-propandiol, MPD) ligands on the other, gold Janus nanoparticles (JNPC6-MPD) behaved analogously to conventional surfactant molecules and could self-assemble into hollow emulsions. Significantly, the resulting nanoparticle ensembles exhibited positive circular dichroism absorption in the visible range that corresponded to the surface plasmonic resonance (SPR) region of the ensemble structures (600 – 800 nm),[14] which was accounted for by the vortex arrangements of nanoparticle dipoles on a spherical surface, in sharp contrast to individual Janus nanoparticles that were achiral. This led to preferred encapsulation of select enantiomers into the nanoparticle emulsion cavities, such as D-alanine over L-alanine.[14]

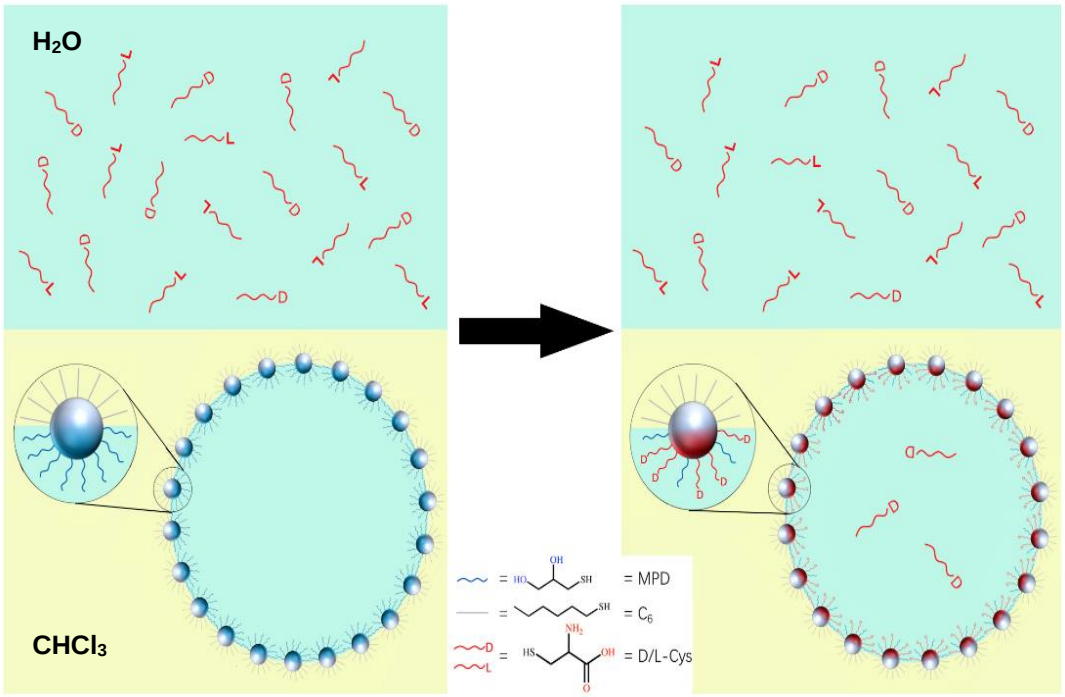

Scheme 3.1. Schematic of enantiomerically selective interfacial ligand exchange of nanoparticles by encapsulation of an optical enantiomer from a racemic mix of ligands.

Such a unique property may be exploited for controlled functionalization of nanoparticles with select enantiomers from a racemic mixture, where the nanoparticle emulsions serve as an enantiomerically selective nanoreactor. In the present study, cysteine will be used as the illustrating example. Experimentally, JNPC6-MPD (core dia. 2.7 ± 0.4 nm) were prepared by interfacial engineering based on the Langmuir method, where a monolayer of hexanethiolate-capped gold (AuC6) nanoparticles was formed on the water surface of a Langmuir-Blodgett trough and underwent ligand exchange reactions with MPD dispersed in the water subphase (details in the Experimental Section).[15] The obtained JNPC6-MPD nanoparticles were then dispersed in $CHCl_3$ at a concentration of 1 mg/mL, and mixed with an equal volume of an aqueous

solution of D,L-cysteine (Cys, concentration 10 mM), where the Janus nanoparticles underwent template-less self-assembly into water-in-oil emulsions (**Scheme 3.1**). As the Cys ligands were encapsulated within the water phase and in direct contact with the MPD hemisphere,[16] ligand exchange reaction would occur, but mostly initiated with the MPD face. The resulting particles were denoted as JNPC6-MPD/$_{DL}$Cys. FTIR measurements show a broad peak between 3500 – 3200 cm^{-1} (O-H stretch), 2950 – 2800 cm^{-1} (sp^3 C-H), 1725 cm^{-1} (C=O stretch), and 1065 cm^{-1} (C-O stretch) (**Figure 3.1**),[17] suggesting the successful incorporation of the Cys ligands onto the nanoparticle surface, and the lack of a vibrational peak at 2550 cm^{-1} indicates the absence of free thiol ligands (e.g., MPD and cysteine molecules) in the samples.

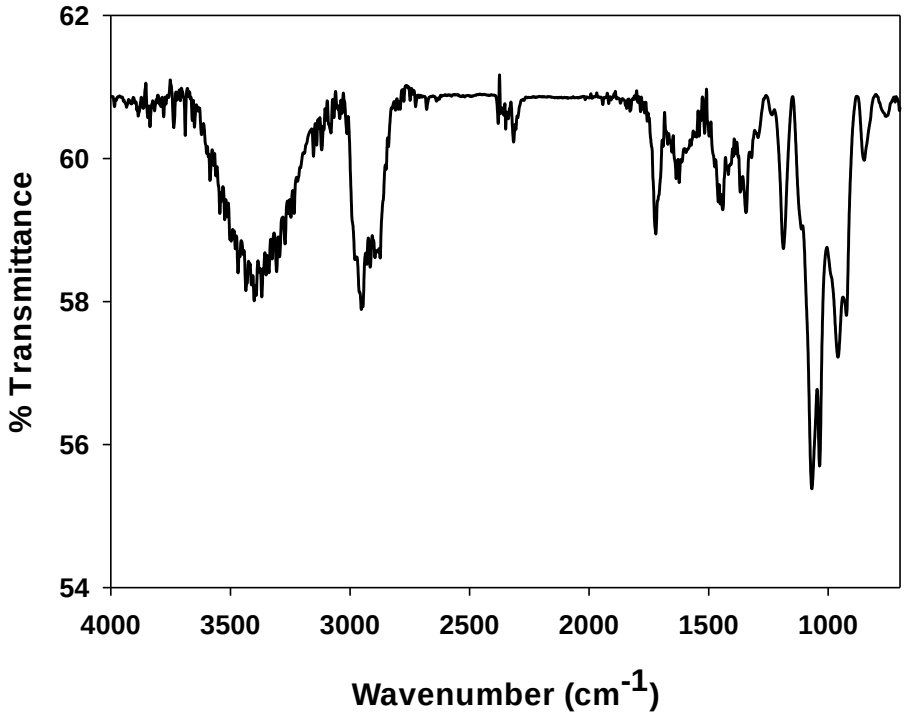

Figure 3.1. FTIR of JNPC6-MPD after ligand exchange with D,L-cysteine molecules for 24 h.

The ligand composition on the nanoparticle surface was then quantified by ^{1}H NMR measurements (**Figure 3.2**a), whereby the ligands were desorbed from the nanoparticle surface by the addition of iodine. The percent composition of each ligand (**Table 3.1**) was calculated based on the integrated peak areas of the terminal methyl protons of C6 (0.88 ppm), methylene protons of MPD (3.35 ppm), and methine protons of Cys (4.35 ppm).[17] From **Figure 3.3**, one can see that the as-prepared JNPC6-MPD nanoparticles consisted of about 52% C6 and 48% MPD ligands. That is, the hydrophobic and hydrophilic ligands each accounted for roughly half of the capping ligands on the nanoparticle surface. Within the initial four hours of mixing with D,L-Cys, one can see that the C6 ligand fraction remained virtually unchanged, whereas MPD concentration diminished rapidly to only 15.7% and concurrently Cys became detectable with the concentration increasing accordingly to 29.8%. This suggests that within this time frame, ligand exchange reaction occurred between the nanoparticles and Cys ligands, and the reaction was largely confined to the MPD hemispheres. This can be ascribed to the formation of water-in-oil reverse emulsions by the Janus nanoparticles, where Cys was encapsulated within the water phase, leading to direct contact of the MPD hemisphere with the Cys ligands (Scheme 1). These observations suggest that the Janus nanoparticle emulsions can indeed be exploited as a unique nanoreactor for directional functionalization of nanoparticles.[18] At longer reaction times, the surface concentrations of both C6 and MPD ligands can be found to diminish appreciably, suggesting extensive replacements of both types of ligands by the Cys

ligands. For instance, after mixing for 24 h, the surface concentration of the C6 ligand decreased to only 11.5%, MPD to 3.8%, whereas Cys increased to 84.7%.

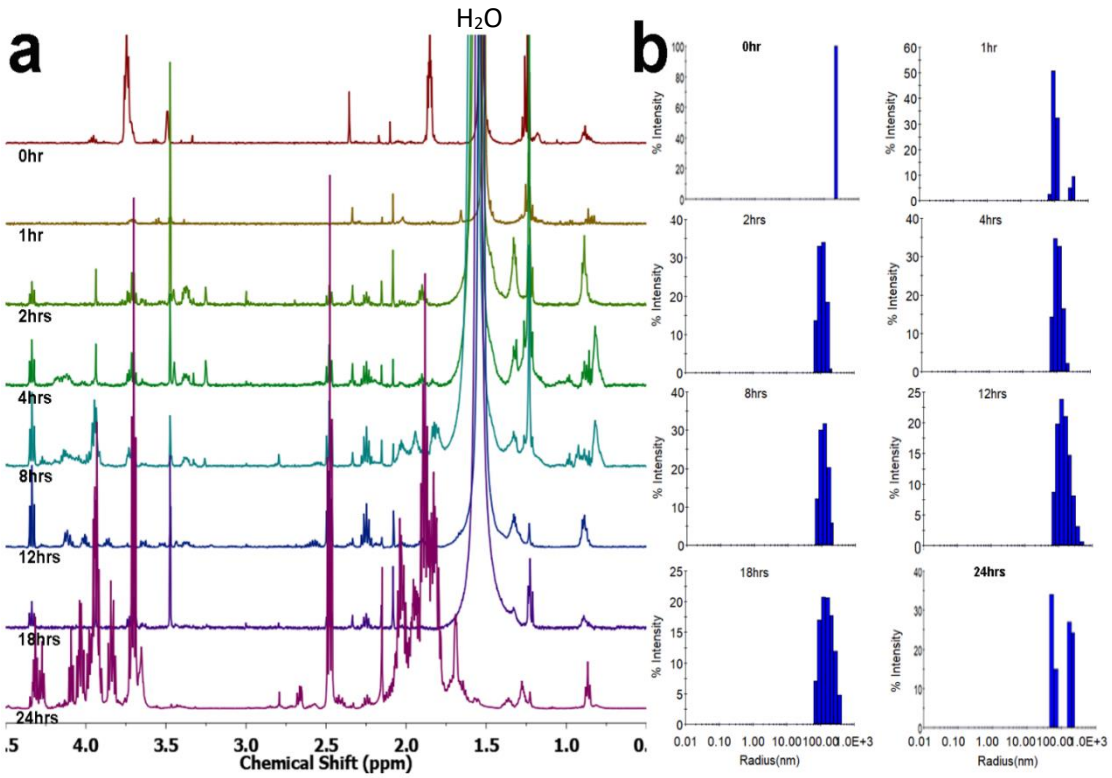

Figure 3.2. (a) NMR spectra of JNPC6-MPD in $CDCl_3$ before and after ligand exchange reaction with D,L-cysteine in water for up to 24 h. Ligands are desorbed by I_2 desorption prior to NMR measurements. b) Hydrodynamic radius from DLS measurement of JNPC6-MPD in $CHCl_3$ before and after ligand exchange reaction with D,L-cysteine in water for up to 24 h. Nanoparticle concentration 0.15 mg/mL.

Table 3.1. Ligand composition by NMR in $CDCl_3$ and averaged hydrodynamic radius (R_H) of JNPC6-MPD nanoparticles after exchange reactions with D,L-cysteine for different periods of time

Time (h)	C6 (%)	MPD (%)	Cys (%)	R_H (nm)
0	52.0	48.0	0.0	229.6 ± 1.4
1	54.1	36.1	9.8	107.4 ± 8.5
2	50.4	29.8	19.8	118.2 ± 4.8
4	54.5	15.7	29.8	117.5 ± 7.1
8	44.9	10.2	44.9	125.2 ± 3.7
12	32.5	9.3	58.1	162.8 ± 10.5
18	28.7	6.9	64.3	175.5 ± 10.2
24	11.5	3.8	84.7	170.2 ± 31.7

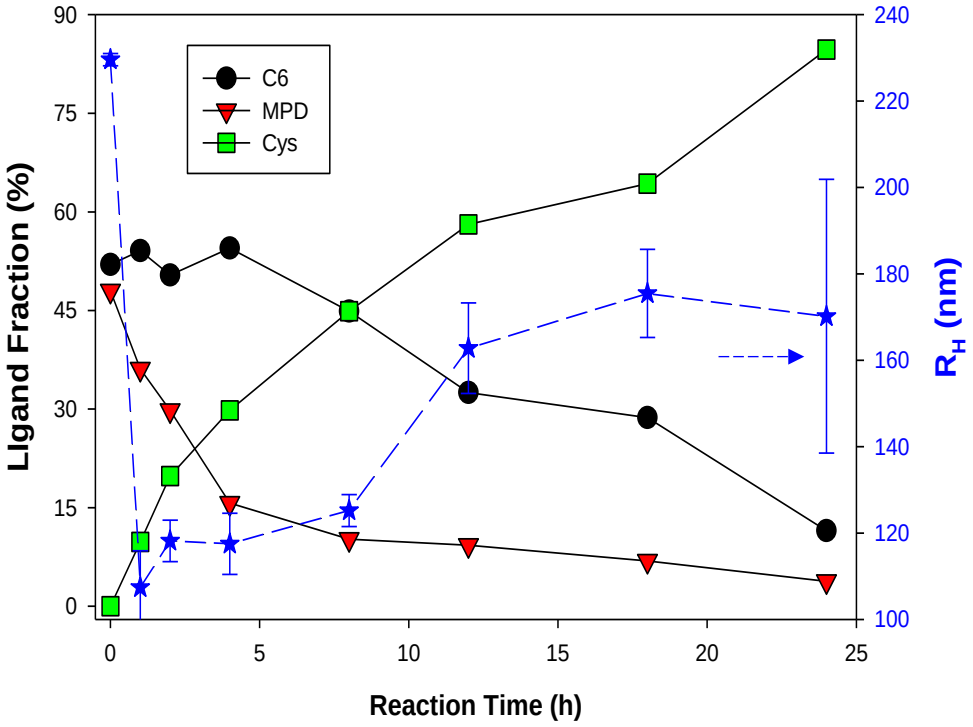

Figure 3.3. Ligand composition and average hydrodynamic radius of JNPC6-MPD nanoparticle ensembles after exchange reaction with an enantiomeric mixture of D,L-cysteine for different periods of time.

Interestingly, the nanoparticle ensemble structures remained largely intact during the initial four hours of exchange, as manifested in transmission electron microscopic (TEM) measurements. From **Figure 3.4**a, one can see that the as-prepared JNPC6-MPD nanoparticles indeed formed hollow emulsions of up to 500 nm in diameter (**Figure 3.5**), as observed previously,[14] and after four hours of exchange reactions with Cys, whereas the shape was almost retained, the size did diminish somewhat (**Figure 3.4b**). However, at even longer reaction times, the nanoparticle ensembles appeared to be dismantled (**Figure 3.4c**). This is consistent with the variation of the ligand surface concentration (**Figure 3.3**). In the first four hours of ligand exchange, the Janus characters of the nanoparticles were maintained except for a different hydrophilic ligand composition. Thus, the hollow structure of the nanoparticle emulsions was unchanged. Yet, at prolonged ligand exchange reactions with Cys, the surface capping ligands of the nanoparticles became dominated with Cys. The lack of an amphiphilic character of the nanoparticle surface rendered it difficult to maintain the emulsion arrangement. In fact, one can see that some small, compact ensembles of nanoparticles were formed instead, because of decreasing solubility of the resulting nanoparticles in $CHCl_3$.

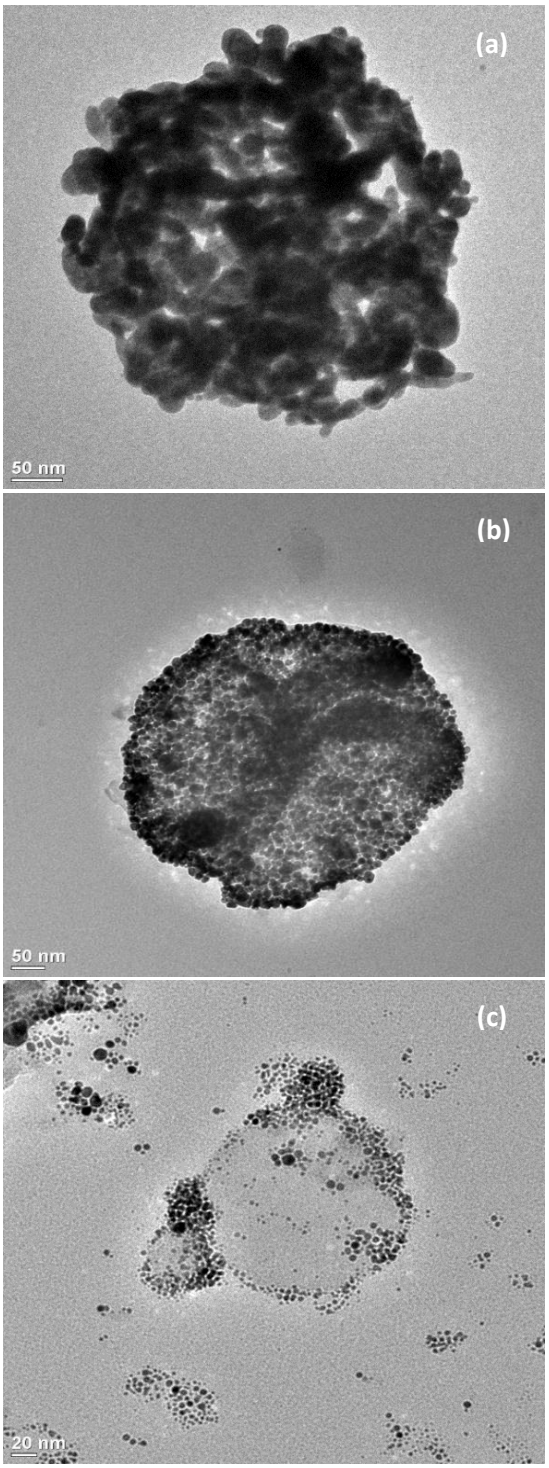

Figure 3.4. Representative TEM images of JNPC6-MPD Janus nanoparticle ensembles (a) before and after exchange reaction with Cys for (b) 4 and (c) 24 h. Nanoparticle concentration of 0.15 mg/mL in $CHCl_3$. Scale bars are (A,B) 50 nm and (C) 20 nm.

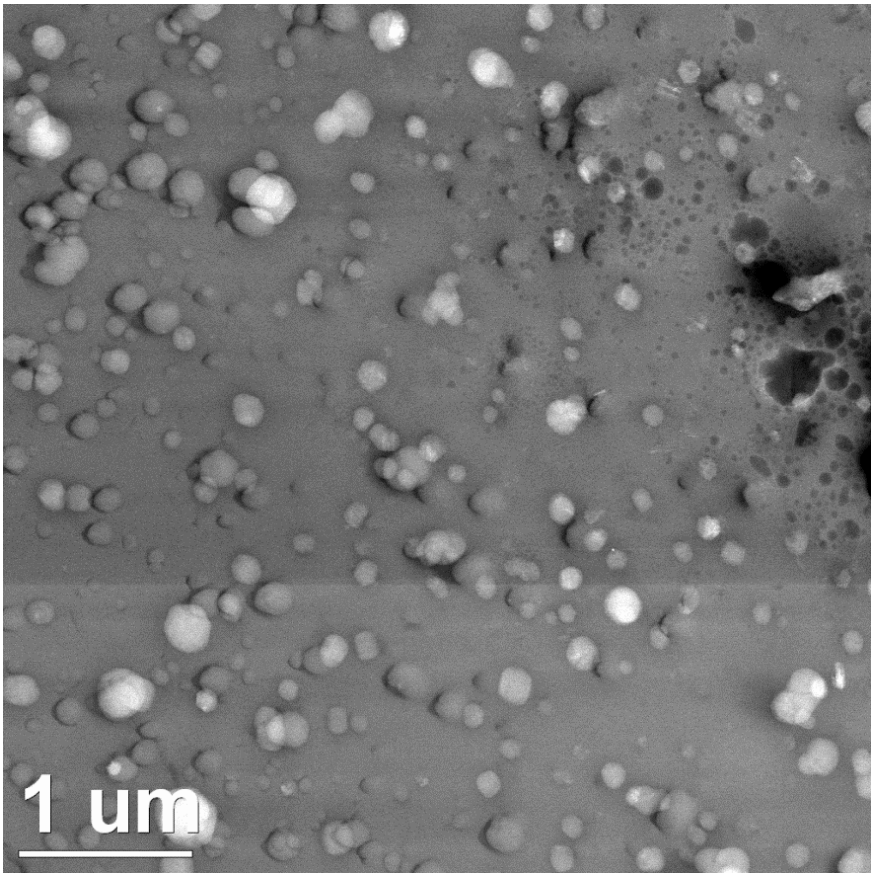

Figure 3.5. Representative TEM image of JNPC6-MPD nanoparticle ensembles.

Consistent structural insights were obtained in dynamic light scattering (DLS) measurements (**Figure 3.2b**). Figure 1 (blue dashed curve) shows the variation of the hydrodynamic radius (R_H) of the JNPC6-MPD nanoparticles in $CHCl_3$ upon mixing with Cys in water. It can be seen that prior to mixing with the Cys ligands, the JNPC6-MPD nanoparticles showed an average hydrodynamic radius of ca. 230 nm, which decreased significantly to ca. 107 nm after mixing with Cys for 1 h and remained virtually invariant for up to 4 h. This is most likely due to the partial replacement of MPD ligands on the nanoparticle surface by Cys where the strong hydrogen bonding

between Cys of neighboring nanoparticles enhanced packing within the nanoparticle ensembles.[19] In fact, one can see that the nanoparticle ensembles became less porous than the initial ones (**Figure 3.4a-b**). However, at longer reaction times, the hydrodynamic radius can be seen to actually increase slowly, although it became increasingly difficult to form nanoparticle ensembles, as revealed in TEM measurements (**Figure 3.2c**). This is likely due to the formation of Au(I)-SR polymeric complexes as a result of thiol (cysteine) etching of the gold cores (more discussion below),[20,21] as manifested by the dark grey enclosure surrounded by nanoparticles in Figure 4c.

UV-vis and circular dichroism (CD) measurements were then carried out to examine the chiroptical response of the nanoparticle ensembles during ligand exchange reactions with Cys. From **Figure 3.6**a, one can see that prior to mixing with Cys, the JNPC6-MPD nanoparticles in $CHCl_3$ exhibited a broad absorption peak centered around 600 nm, consistent with the formation of nanoparticle ensembles where dipolar coupling between neighboring nanoparticles led to a significant red-shift of the SPR absorption, as compared to that (510 nm) of individual nanoparticles.[14] Upon mixing with Cys for up to 24 h, a significant red-shift of the SPR absorption remained apparent, in good agreement with results from TEM measurements (**Figure 3.4**), where formation of ensembles/aggregates of nanoparticles can be clearly seen. In addition, after prolonged ligand exchange reaction, a new absorption peak emerged at ca. 370 nm. This likely arose from the combined contributions of interband transitions from Au $5d^{10}$ to 6sp as well as ligand-metal charge-transfer transitions of Au(I)-thiolate

polymeric complexes produced in the presence of excess thiol ligands (Cys), as observed previously.[20-22]

The CD absorption profiles varied accordingly. From **Figure 3.6b**, it can be seen that for the JNPC6-MPD nanoparticles, positive CD signals (~ 10 mdeg) appeared in the wavelength range of 550-800 nm, which was coincidental to the broad SPR absorption observed in **Figure 3.3a**. This has been ascribed to plasmonic circular dichroism (PCD) absorption and accounted for by the vortex arrangement of the nanoparticle dipoles when they self-assembled onto a spherical surface forming hollow emulsion-like nanostructures.[14] Upon mixing with Cys, this PCD absorption actually changed sign and became slightly intensified with prolonging reaction time (**Figure 3.3b** inset). In the previous study,[14] a similar transition was observed when JNPC6-MPD emulsions were mixed with D,L-alanine and the change of PCD sign was accounted for by the preferred encapsulation of D-Ala into the emulsion interior because the nanoparticle emulsions behaved analogously to an L enantiomer. This suggests that, in the present study, D-Cys was the preferred enantiomers that were entrapped within the nanoparticle emulsions, and incorporated onto the nanoparticle surface by interfacial ligand exchange reactions. From these results, one can see that with a proper control of the reaction time (e.g., 4 h within the present experimental context), chiral gold Janus nanoparticles could actually be produced due to selective encapsulation and surface functionalization with the D-Cys ligands, in contrast to JNPC6-MPD that were achiral.[14] That is, the Janus nanoparticle emulsions can be

exploited as a chiral nanoreactor for selective uptake of a certain enantiomer from a racemic mixture, leading to controlled chirality of the resulting nanoparticles.

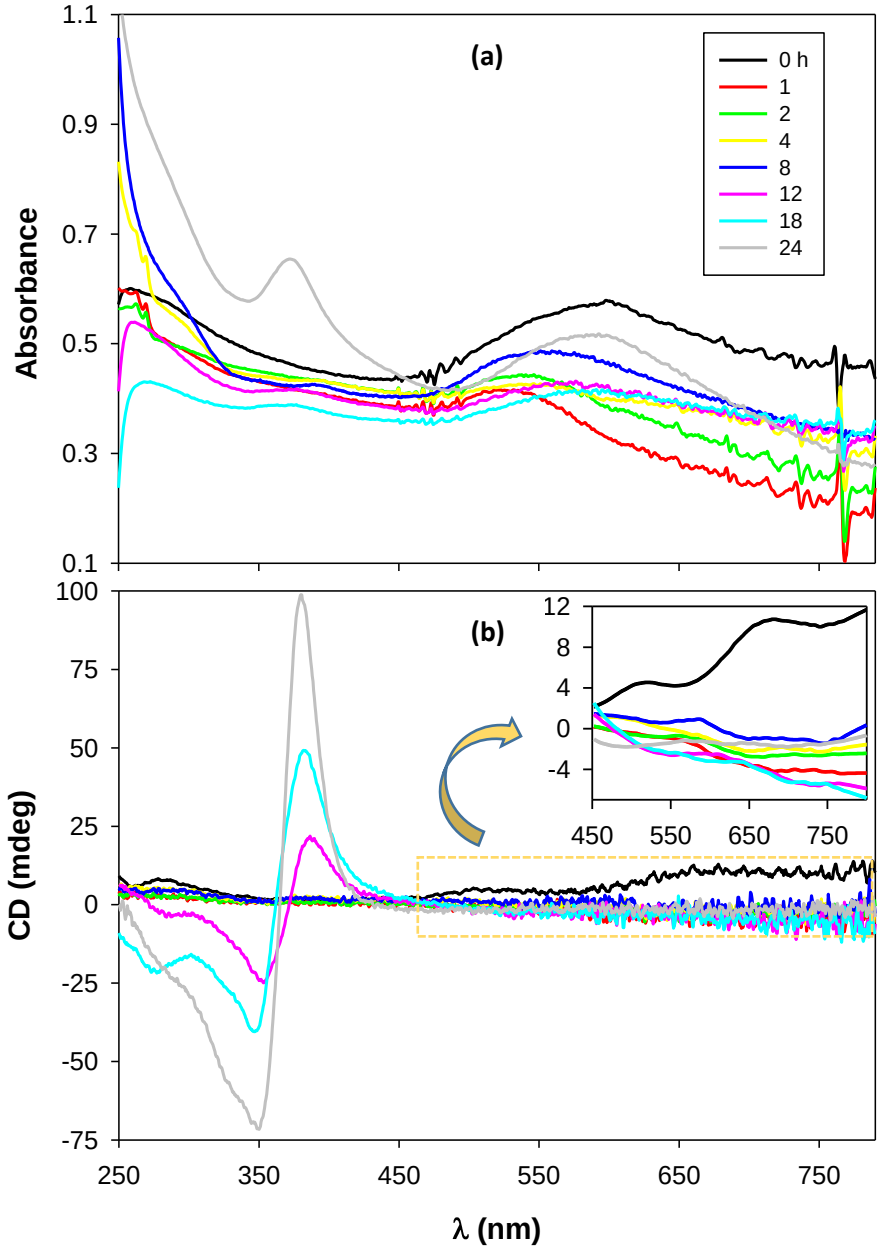

Figure 3.6. (a) UV-vis and (b) CD spectra of JNPC6-MPD nanoparticles after exchange reactions with D,L-cysteine for different periods of time. Nanoparticles concentration of 0.15 mg/mL in $CHCl_3$. Inset to panel (b) is the zoom in of the region between 450 and 800 nm.

In addition, one can see that a CD response started to appear at 300 – 400 nm with an apparent positive cotton effect after ligand exchange with Cys for 8 h, and the absorption became intensified at longer reaction times. It should be noted that this is completely different from the CD characteristics of free Cys monomers, which only appear at the far UV region ($\lambda < 250$ nm) for either enantiomers (**Figure 3.7**). A similar response has been observed previously with Au(I)-thiolate polymeric complex formed by reaction of $HAuCl_4$ with D-Cys.[20,21] This further confirms that D-Cys was indeed the preferred enantiomers that were encapsulated into the nanoparticle emulsions. The fact that this CD peak only appeared after prolonged ligand exchange reactions with Cys was due to etching of the gold nanoparticle cores by the Cys ligands producing the corresponding chiral polymeric complexes, consistent with results obtained from TEM (**Figure 3.4**) and UV-vis (**Figure 3.6a**) measurements. Consistent optical and PCD responses were observed when enantiomerically pure D-Cys ligands were used (not shown).

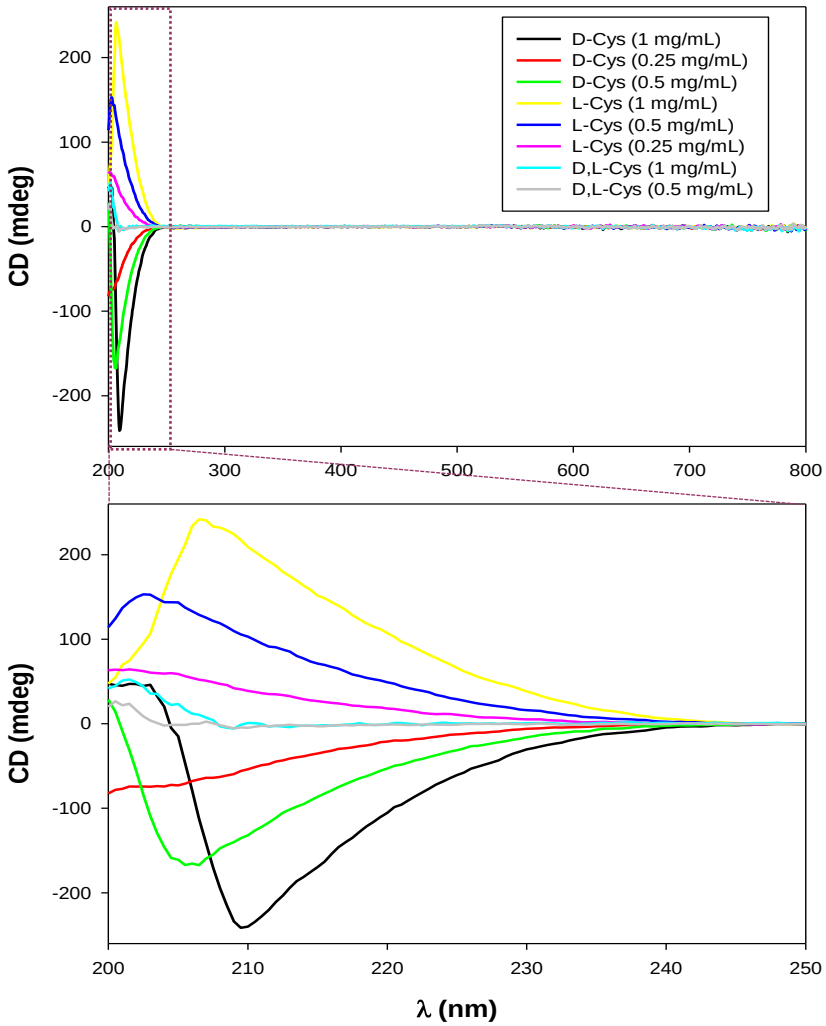

Figure 3.7. CD absorption spectra of D-Cys, L-Cys, and D,L-Cys at varied concentrations in water. The bottom panel is the zoom in of the data highlighted by the dark red box in the top panel within the range of 200 to 250 nm.

With D-Cys preferentially encapsulated by the JNPC6-MPD nanoparticle ensembles (in $CHCl_3$) and incorporated onto the nanoparticle surface, L-Cys indeed was found to be in 10.2% excess in the initially racemic mixture of D,L-Cys in water after ligand exchange reaction with JNPC6-MPD nanoparticles for 24 h (**Figure 3.8**). Of the 10.2% D-Cys that was transferred into the organic phase, ca. 6.7% was

incorporated onto the nanoparticle surface (**Figure 3.9**), and the rest (3.5%) likely in the forms of Au(I) complex and free monomers within the nanoparticle emulsions.

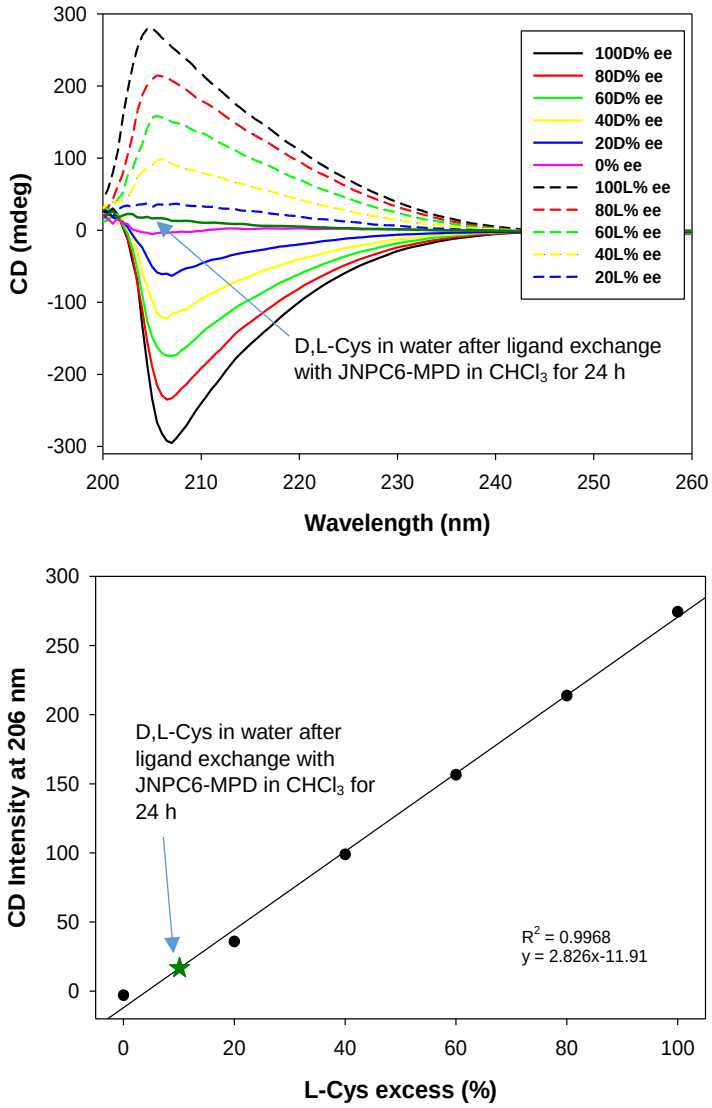

Figure 3.8. (top panel) CD spectra of cysteine aqueous solutions at the concentration of 10 mM but at different enantiomeric excess. Dark green curve is the spectrum for the cysteine solution (10 mM) after ligand exchange with JNPC6-MPD in $CHCl_3$ (1 mg/mL) for 24 h at equal volume (Figure 3.1). (bottom panel) Variation of the corresponding CD intensity at 206 nm with the percent excess of L-Cys. Circle symbols are data for the standard solutions, and dark green star is for the cysteine solution after ligand exchange with JNPC6-MPD in $CHCl_3$ for 24 h where the L-Cys excess is estimated to be ca. 10.2%.

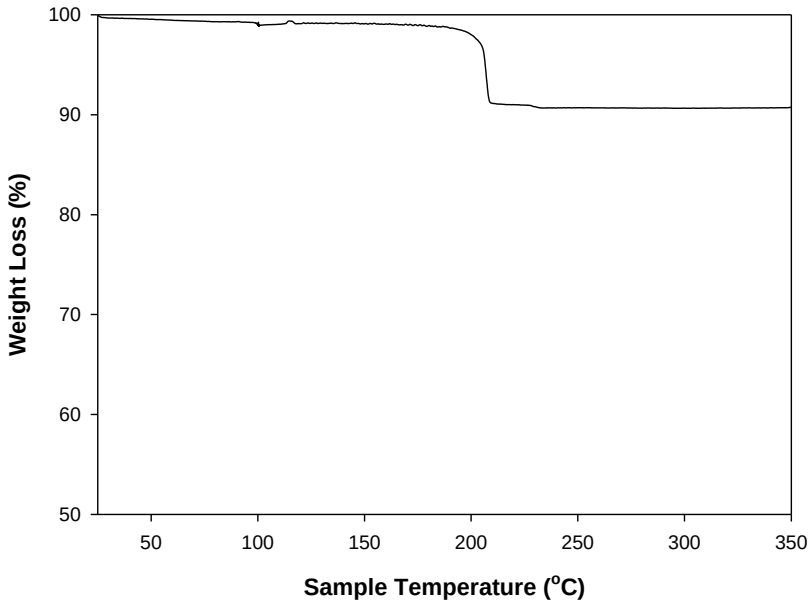

Figure 3.9. TGA curve of AuC6 nanoparticles. The C6 ligand content is estimated to be 9.4 wt%. In conjunction with results from the ^{1}H NMR measurements (Figure 3.1), the amount of D-Cys incorporated onto the nanoparticle surface after ligand exchange reaction for 24 h accounts for about 6.7% of cysteine in the original racemic mixture of D,L-cysteine in water.

In summary, in the present study we demonstrate that as Janus nanoparticle could self-assemble into hollow, emulsion-like nanostructures that exhibited apparent PCD characteristics, selective encapsulation of a certain enantiomer from a racemic mix of ligands can be readily achieved. This suggests that the nanoparticle emulsions can be exploited as a chiral nanoreactor for directional functionalization of the nanoparticle surface, leading to the formation of controlled chirality of the (individual) nanoparticles, as demonstrated in the present study with D,L-cysteine.

Significantly, it has been previously demonstrated that the chirality of mesophases of achiral monomers can be induced and manipulated by external stimuli, such as vortex agitation and chiral dopants.[23-25] Such a mechanism may also be

exploited for a more deliberate control of the chirality of the nanoparticle emulsions and hence the resulting individual nanoparticles after directional ligand exchange. This will be pursued in further studies.

3.3 Experimental Section

*Chemicals***.** Hydrogen tetrachloroauric acid trihydrate ($HAuCl_4 \cdot 3H_2O$, Fisher, 99%), tetra-n-octylammonium bromide (TOABr, Alfa Aesar, 98%), 1-hexanethiol (C6SH, Acros, 96%), sodium borohydride ($NaBH_4$, Acros, 99%), racemic 3-mercaptopropane-1,2-diol (MPD, Aldrich, 95%), D-cysteine (D-Cys, CHEM-IMPEX INT'L INC., 99.12%) and L-cysteine (L-Cys, MATHESON COLEMAN & BELL) were used as received. All solvents used were purchased from commercial sources at their highest purities and used without further treatment. Water was supplied by a Barnstead Nanopure water system (18.3 MΩ·cm).

Sample preparation. The preparation of JNPC6-MPD Janus nanoparticles (average core diameter 2.7 ± 0.4 nm) has been detailed previously.[14] For ligand exchange reaction with D,L-Cys, the as-prepared JNPC6-MPD nanoparticles were dispersed in $CHCl_3$ at a concentration of 1 mg/mL, and a cysteine aqueous solution was prepared at a concentration of 10 mM (5 mM each for D-Cys and L-Cys). The two solutions were then mixed under magnetic stirring ligand exchange reactions. An aliquot of the organic phase was removed at select time intervals for UV-vis and CD measurements. The nanoparticles were then precipitated by the addition of an excess of methanol and collected by centrifugation.

Characterization. TEM images were acquired with a FEI monochromated F20 UT Tecnai transmission electron microscope operated at 200 kV. UV-vis absorption spectra were obtained with a PerkinElmer Lambda 35 UV-vis spectrometer, and circular dichroism (CD) measurements were carried out with a JASCO J1500 CD spectrometer. FTIR measurements were performed with a PerkinElmer Spectrum One spectrometer. Proton nuclear magnetic resonance (^{1}H NMR) measurements were conducted with a Varian Unity 500MHz spectrometer, where the samples were dissolved in $CDCl_3$ and ligands were desorbed from the nanoparticle surface by the addition of a small amount of iodine. Dynamic light scattering (DLS) measurements were carried out with a Wyatt DynaPro NanoStar temperature-controlled micro-sampler at room temperature. Thermogravimetric analysis (TGA) was performed with a Perkin-Elmer Pyris 1 instrument at the heating rate of 10 °C/min under a nitrogen atmosphere.

3.4 References

(1) Kang, Y. J.; Oh, J. W.; Kim, Y. R.; Kim, J. S.; Kim, H. Chiral gold nanoparticle-based electrochemical sensor for enantioselective recognition of 3,4-dihydroxyphenylalanine. *Chem Commun* **2010**, *46*, 5665-5667.

(2) Shukla, N.; Bartel, M. A.; Gellman, A. J. Enantioselective Separation on Chiral Au Nanoparticles. *J Am Chem Soc* **2010**, *132*, 8575-8580.

(3) Yasukawa, T.; Miyamura, H.; Kobayashi, S. Chiral metal nanoparticle-catalyzed asymmetric C-C bond formation reactions. *Chemical Society Reviews* **2014**, *43*, 1450-1461.

(4) Preiss, L. C.; Werber, L.; Fischer, V.; Hanif, S.; Landfester, K.; Mastai, Y.; Munoz-Espi, R. Amino-Acid-Based Chiral Nanoparticles for Enantioselective Crystallization. *Adv Mater* **2015**, *27*, 2728-+.

(5) Fuchs, I.; Fechler, N.; Antonietti, M.; Mastai, Y. Enantioselective Nanoporous Carbon Based on Chiral Ionic Liquids. *Angew Chem Int Edit* **2016**, *55*, 408-412.

(6) Xie, F. F.; Bai, Q.; Jiang, X. M.; Yu, X. S.; Xia, Z. N.; Wei, W. L. Visual and Colorimetric High-Throughput Analysis of Chiral Carboxylic Acids Based on Enantioselective Charge Shielding of Gold Nanoparticles. *Acs Appl Mater Inter* **2018**, *10*, 11872-11879.

(7) Song, J. B.; Huang, P.; Duan, H. W.; Chen, X. Y. Plasmonic Vesicles of Amphiphilic Nanocrystals: Optically Active Multifunctional Platform for Cancer Diagnosis and Therapy. *Accounts of Chemical Research* **2015**, *48*, 2506-2515.

(8) Lee, H. Y.; Shin, S. H. R.; Drews, A. M.; Chirsan, A. M.; Lewis, S. A.; Bishop, K. J. M. Self-Assembly of Nanoparticle Amphiphiles with Adaptive Surface Chemistry. *Acs Nano* **2014**, *8*, 9979-9987.

(9) Shemer, G.; Krichevski, O.; Markovich, G.; Molotsky, T.; Lubitz, I.; Kotlyar, A. B. Chirality of silver nanoparticles synthesized on DNA. *J Am Chem Soc* **2006**, *128*, 11006-11007.

(10) Zhang, L.; Xu, C. L.; Song, G. X.; Li, B. X. Self-assembly of L-cysteine-gold nanoparticles as chiral probes for visual recognition of 3,4-dihydroxyphenylalanine enantiomers. *Rsc Adv* **2015**, *5*, 27003-27008.

(11) Wang, P. P.; Yu, S. J.; Govorov, A. O.; Ouyang, M. Cooperative expression of atomic chirality in inorganic nanostructures. *Nat Commun* **2017**, *8*.

(12) Gonzalez-Rubio, G.; Liz-Marzan, L. M. A peptide-guided twist of light. *Nature* **2018**, *556*, 313-314.

(13) Lee, H. E.; Ahn, H. Y.; Mun, J.; Lee, Y. Y.; Kim, M.; Cho, N. H.; Chang, K.; Kim, W. S.; Rho, J.; Nam, K. T. Amino-acid- and peptide-directed synthesis of chiral plasmonic gold nanoparticles. *Nature* **2018**, *556*, 360-365.

(14) Lu, J. E.; Yang, C. H.; Wang, H. B.; Yam, C. Y.; Yu, Z. G.; Chen, S. W. Plasmonic circular dichroism of vesicle-like nanostructures by the template-less self-assembly of achiral Janus nanoparticles. *Nanoscale* **2018**, *10*, 14586-14593.

(15) Pradhan, S.; Xu, L. P.; Chen, S. W. Janus nanoparticles by interfacial engineering. *Adv Funct Mater* **2007**, *17*, 2385-2392.

(16) Song, Y.; Chen, S. W. Janus Nanoparticles as Versatile Phase-Transfer Reagents. *Langmuir* **2014**, *30*, 6389-6397.

(17) Silverstein, R. M.; Bassler, G. C.; Morrill, T. C.: *Spectrometric identification of organic compounds*; 5th ed.; Wiley: New York, 1991.

(18) Pradhan, S.; Ghosh, D.; Chen, S. W. Janus Nanostructures Based on Au-TiO2 Heterodimers and Their Photocatalytic Activity in the Oxidation of Methanol. *Acs Appl Mater Inter* **2009**, *1*, 2060-2065.

(19) Gao, M.; Deng, J.; Chu, H. Y.; Tang, Y.; Wang, Z.; Zhao, Y. J.; Li, G. H. Stereoselective Stabilization of Polymeric Vitamin E Conjugate Micelles. *Biomacromolecules* **2017**, *18*, 4349-4356.

(20) Howard-Lock, H. E. Structures of gold(i) and silver(i) thiolate complexes of medicinal interest: a review and recent results. *Metal-based drugs* **1999**, *6*, 201-209.

(21) Russier-Antoine, I.; Bertorelle, F.; Kulesza, A.; Soleilhac, A.; Bensalah-Ledoux, A.; Guy, S.; Dugourd, P.; Brevet, P. F.; Antoine, R. Chiral supramolecular gold-cysteine nanoparticles: Chiroptical and nonlinear optical properties. *Prog Nat Sci-Mater* **2016**, *26*, 455-460.

(22) Qi, H.; Hegmann, T. Postsynthesis Racemization and Place Exchange Reactions. Another Step To Unravel the Origin of Chirality for Chiral Ligand-Capped Gold Nanoparticles. *J Am Chem Soc* **2008**, *130*, 14201-14206.

(23) Ribo, J. M.; Crusats, J.; Sagues, F.; Claret, J.; Rubires, R. Chiral sign induction by vortices during the formation of mesophases in stirred solutions. *Science* **2001**, *292*, 2063-2066.

(24) Shen, Z. C.; Wang, T. Y.; Liu, M. H. Macroscopic Chirality of Supramolecular Gels Formed from Achiral Tris(ethyl cinnamate) Benzene-1,3,5-tricarboxamides. *Angewandte Chemie-International Edition* **2014**, *53*, 13424-13428.

(25) Liu, M. H.; Zhang, L.; Wang, T. Y. Supramolecular Chirality in Self-Assembled Systems. *Chemical Reviews* **2015**, *115*, 7304-7397.

Chapter 4
Poly(ethylene glycol)-functionalized Janus nanoparticles and the selective interaction with alkali metal ions

4.1 Abstract

Gold Janus nanoparticles were prepared by interfacial ligand exchange, with hydrophilic poly(ethylene glycol) (PEG) ligands on one hemisphere and hydrophobic hexanethiolates one the other. Due to specific interaction of PEG with alkali metal ions, the Janus nanoparticles exhibited marked conformational changes forming organized ensembles in the presence of Na^+ and K^+, as manifested in dynamic light scattering, UV-vis absorption and transmission electron microscopic measurements, whereas no apparent variation was observed with bulk-exchange nanoparticles where the two types of capping ligands were homogeneously mixed on the nanoparticle surface or nanoparticles capped with the PEG ligands alone. The ion complexation was further probed in NMR measurements. Results from this study indicate that select doping of alkali metal ions into PEG-functionalized nanoparticles may be used for controlled assembly of the Janus nanoparticles.

4.2 Introduction

Poly(ethylene glycol) (PEG) represents a family of functional polymer materials that have found diverse applications ranging from industrial manufacturing to medicine [1]. One unique characteristic of PEG is the specific interaction with alkali metal ions, a behavior analogous to crown ethers that can lead to marked enhancement of the electrical conductivity [2-6]. In a previous study [7], it has been shown that in the absence of alkali metal ions, triphenylene derivatives containing two to four units of

ethylene oxide formed a stable discotic nematic phase (N_D) at room temperature, and underwent a unique phase transition to a stable hexagonal columnar (Col_h) phase upon the addition of alkali metal ions (e.g., Li^+ and Na^+) through ion-dipole interactions, straightening the randomly coiled and bent PEG chains. Self-assembled monolayers of PEG grown on metal substrate surfaces can also be affected by the addition of alkali metal ions [8,9]. In the absence of alkali metal ions, PEG first self-assembles into small branched dendrite structures with voids at low concentrations on a gold surface; and as the PEG concentration increases, the PEG grows along the terrace steps of gold, and finally adapts the six-fold symmetry of Au(111) [8]. Upon the addition of alkali metal ions, triblock polymers composed of polycaprolactone and poly(ethylene oxide) form multilayered planar structure, sisal-like structure and spherical aggregates upon the addition of Li^+, Na^+ and K^+, respectively [9]. The aggregation disparity is attributed to the structural difference of complex formation between the polymer chains and alkali metal ions of different radii [10], thus resulting in different self-ensembled alignment and crystallization.

In fact, depending on the size of the alkali metal ion and the degree of polymerization of the PEG chain, the interaction kinetics can vary significantly [11,12]. In contrast to early proposal of the formation of double helical structures [13], recent studies have shown that the interaction of PEG with alkali cations actually leads to the formation of local helical structures, which increases in length with increasing size of the cation [14]. For instance, cyclic PEG with six repeating units has been found to chelate alkali metal ions of Rb^+, K^+, Na^+, and Li^+ at 1:1 ratio per nano-cavity (with the highest

selectivity towards K^+), but 2:1 for Cs^+ due to its larger atomic radius [15]. Linear PEG shows a higher affinity to Li^+ for chain length shorter than 26 repeat units and higher affinity to Na^+ for chain length over 26 repeat units [14]. Notably, for cyclic PEG, water-ion bonding interaction is the major contribution to the formation of stable PEG-ion complexes, which becomes increasingly dominant with decreasing size of the alkali metal ion ($K^+ < Na^+ < Li^+$), and PEG-ion interactions play only a minor role; by contrast, for linear PEG, the primary contribution is the PEG-ion interactions, which increases as the size of the alkali metal ion decreases ($K^+ < Na^+ < Li^+$), due to the higher cohesion and stability of the PEG-ion complexes when solvated by water [16]. In fact, PEG tends to favor linear conformation for interaction with alkali metal ions in solution, without undergoes significant conformational change [17].

Note that in solution phase, the maximum size/conformation of a polymer can be described by the Flory radius, $F = \alpha n^{3/5}$, where α is the length of each repeating unit and n is the number of repeating units [18]. For PEG-protected nanoparticles in solution, the conformation of PEG on nanoparticle surfaces is in essence dictated by the ratio between the Flory radius (F) and the distance between the attachment points of PEG (D), where PEG exhibits a "mushroom" conformation at low PEG density (D > F) and "brush" conformation at high PEG density (D < F) [19].

Herein, we prepared structurally asymmetrical Janus nanoparticles with hexanethiolates on one face and PEG thiols on the other, and studied the interactions of the nanoparticles with alkali metal ions, in comparison with bulk-exchange nanoparticles where the PEG and hexanethiolate ligands were homogeneously mixed

on the nanoparticle surface. The results show that the as-prepared Janus nanoparticles were individually dispersed in water, whereas upon the addition of Na^+, formation of organized ensembles occurred due to enhanced rigidity of the PEG ligands and amphiphilicity of the nanoparticle structure, in contrast to the bulk-exchange counterparts.

4.3 Experimental Section

Chemicals. Hydrogen tetrachloroaurate trihydrate ($HAuCl_4 \cdot 3H_2O$, Fisher, 99%), tetra-*n*-octylammonium bromide (TOABr, Alfa Aesar, 98%), 1-hexanethiol (C6SH, Acros, 96%), sodium borohydride ($NaBH_4$, Acros, 99%), and poly(ethylene glycol) methyl ether thiol (PEGSH, Sigma-Aldrich, average Mn = 800) were used as received. All solvent used were purchased from commercial sources at their highest purities and used without further treatment. Ultra-pure water was supplied by a Barnstead Nanopure water system (18.3 MΩ·cm).

Preparation of hexanethiolate-protected gold (AuC6) nanoparticles. AuC6 nanoparticles were synthesized by using the Brust method [20]. Typically, 30 mL of an aqueous $HAuCl_4$ solution (0.03 M) was mixed with 20 mL of a toluene solution of TOABr (0.20 M) under vigorous stirring for one hour. The organic phase was then collected, into which 150 μL of C6SH was quickly injected using an Accumax Pro micropipette. The solution was stirred for 15 min before 24 mL of a freshly prepared, ice-chilled aqueous $NaBH_4$ solution (0.43 M) was added in a dropwise fashion. The

solution showed a dark brown color immediately upon the addition of $NaBH_4$, indicating the formation of gold nanoparticles. The reaction mixture was stirred for an additional 4 h to reduce the core-size dispersity. The organic phase was then collected and washed five times with methanol to remove excess hexanethiol, phase-transfer catalysts, and reaction byproducts. The average core size of the resulting nanoparticles was determined to be 2.7 ± 0.4 nm by transmission electron microscopy (TEM) measurements (**Figure 4.1a**) [21,22].

Preparation of PEG-SH protected gold (AuPEG) nanoparticles. AuPEG nanoparticles were prepared in a slightly different way. In brief, 30 mL of an aqueous $HAuCl_4$ solution (0.03 M) was mixed with 20 mL of a toluene solution of TOABr (0.20 M) under vigorous stirring for one hour. The toluene phase was then collected, into which was added 24 mL of a freshly prepared, chilled aqueous $NaBH_4$ solution (0.43 M) in a dropwise manner. The solution was under magnetic stirring for 8 h before the organic phase was collected and washed at least 3 times with nanopure water. An aqueous PEGSH solution (0.13 g in 15 mL) was then added into the toluene solution. After magnetic stirring for 8 h, the aqueous phase exhibited a dark brown color, signifying successful functionalization of the nanoparticles by the PEGSH ligands. The aqueous phase was collected and washed at least three times with toluene. TEM measurements showed that the average core-size of the resulting AuPEG nanoparticles was 5.6 ± 0.6 nm (**Figure 4.1b**).

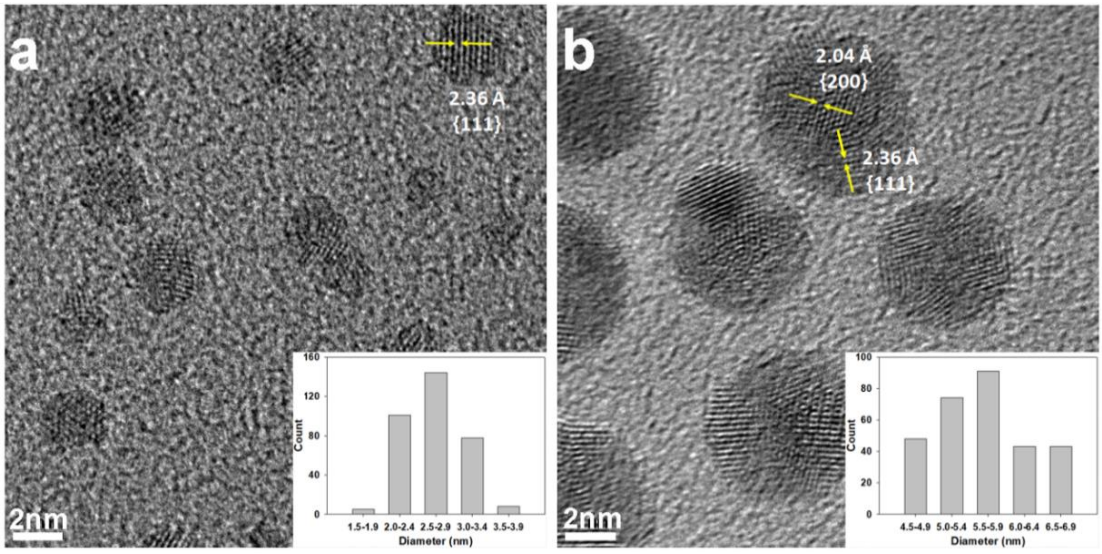

Figure 4.1. TEM images and diameter distributions for (a) AuC6 and (b) AuPEG nanoparticles.

Preparation of AuC6-PEG Janus nanoparticles. AuC6-PEG JNPs were prepared by interfacial engineering based on the Langmuir method, as detailed previously [21-23]. Briefly, AuC6 nanoparticles in toluene were deposited in a dropwise fashion onto the water surface of Langmuir-Blodgett trough (NIMA Technology, model 611D) by using a Hamilton microliter syringe. After evaporation of the organic solvent, the nanoparticle monolayer was compressed to a desired surface pressure, where the interparticle spacing was in the intermediate between one and two fully extended C6SH ligand chain lengths, in order to limit particle mobility. A calculated amount of PEGSH was then injected into the water subsurface using a micropipette to allow interfacial

ligand exchange reactions to take place. The resulting particles were collected after various reaction times (i.e., 1 h, 2 h, and 6 h) such that a different number of PEGSH ligands were incorporated onto the nanoparticle surfaces. The resulting JNPs (JNP1, JNP2 and JNP6) were purified via centrifugation and re-dispersed in chloroform.

As a control experiment, exchange reactions of the AuC6 nanoparticles with PEGSH were also carried out by mixing a calculated amount of AuC6 nanoparticles and PEGSH ligands in THF and stirred for 48 h. The solution was then dried under reduced pressure with a rotary evaporator and excessive ligands were removed by extensive rinsing with methanol. The resulting particles were denoted as bulk-exchange (BE) particles.

Characterization. The nanoparticle morphologies and sizes were studied using transmission electron microscopy (TEM, Philips CM300 at 300 kV). Contact angle measurements were carried out with a Tantec CAM-PLUS contact angle meter, where nanoparticle monolayers on the Langmuir-Blodgett trough were transferred by down-stroke deposition onto a clean glass slide, except for AuPEG that was deposited by spin-casting. At least ten independent measurements per sample were carried out with a constant water droplet volume of 5 μL for statistical analyses. UV-vis absorption measurements were conducted using a PerkinElmer Lambda 35 UV-vis Spectrometer in a 1 cm quartz cuvette. FTIR spectra were acquired with a PerkinElmer Spectrum One FTIR Spectrometer. Proton nuclear magnetic resonance measurements were performed with a Varian Unity 500 MHz spectrometer. Dynamic light scattering (DLS) measurements were carried out with a Wyatt DynaPro NanoStar temperature-

controlled micro-sampler. An aliquot (10 μL) of the particle solution (0.015 mg/mL) was introduced into a sample holder via a 20 μL micropipette. Each sample analysis consisted of 50 measurements which were averaged and reported in terms of radius normalized by percent mass.

4.4 Results and discussion

AuC6-PEG Janus nanoparticles were prepared by interfacial ligand exchange reaction of AuC6 nanoparticles with PEG-SH using Langmuir-Blodgett method for various reaction times (JNP1, JNP2 and JNP6). The resulting nanoparticles were collected using down-stroke deposition method onto cleaned glass slides to allow exposure of the PEG face of the resulting nanoparticles for contact angle measurements. The average contact angle of each sample was shown in **Figure 4.2**. The initial AuC6 nanoparticles were highly hydrophobic with an average contact angle of 102.4 ± 0.8°, whereas the AuPEG nanoparticles were mostly hydrophilic with a much lower average contact angle of 29.2 ± 1.4°. These are consistent with results obtained previously with alkanethiolate-capped gold nanoparticles and poly(ethylene oxide) [9,21-24]. For the JNP nanoparticles, the averaged contact angle values were in the intermediate between 50° and 70°, and decreased with increasing reaction time of PEG, JNP1 (64.1 ± 1.1°) > JNP2 (54.9 ± 1.0°) > JNP6 (50.7 ± 0.8°). Note that the BE nanoparticles also exhibited a comparable contact angle of 61.4 ± 0.8°.

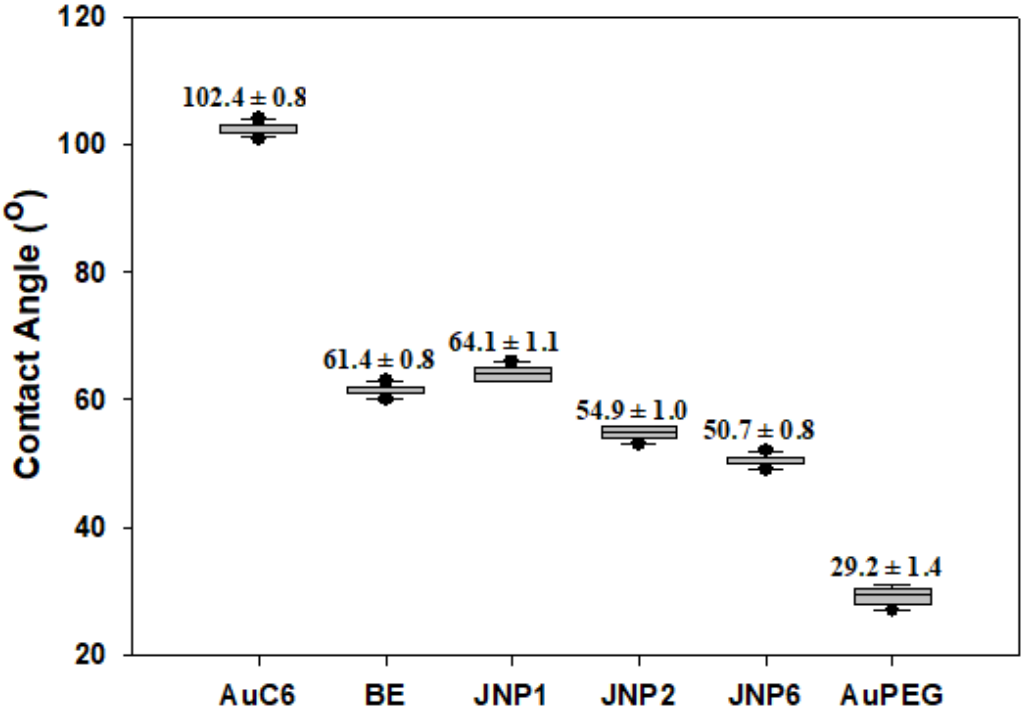

Figure 4.2. Contact angle measurements in determining hydrophilicity of samples with different PEG content.

The incorproation of PEG ligands onto the Janus nanoparticle surface was also confirmed in FTIR measurements (**Figure 4.3a**). Specifically, the sp^3 C–H vibrational stretches of the C6 ligands can be identified at 2923 cm^{-1} and that of PEG at 2868 cm^{-1} [25]. In addition, the C–O stretch of PEG appeared at 1080 cm^{-1} [26], while the absence of the S–H vibrational stretch at 2550 – 2600 cm^{-1} indicated that the samples were free of excessive PEG-SH ligands. More quantitative analysis of the ligand surface coverage was achieved by ^{1}H NMR measurements (**Figure 4.3b**). The peak at 0.88 ppm can be ascribed to the methyl protons of the C6 ligands, whereas the peak at 3.28 ppm to the terminal methyl protons of PEG due to deshielding effect from the adjecent oxygen atoms [25]. Based on the integrated peak areas of these methyl protons, the mole fraction

of PEG was estimated to be 14.5% for JNP1, 23.7% for JNP2, and 40.8% for JNP6, in comparison to 52.8% for the BE nanoparticles.

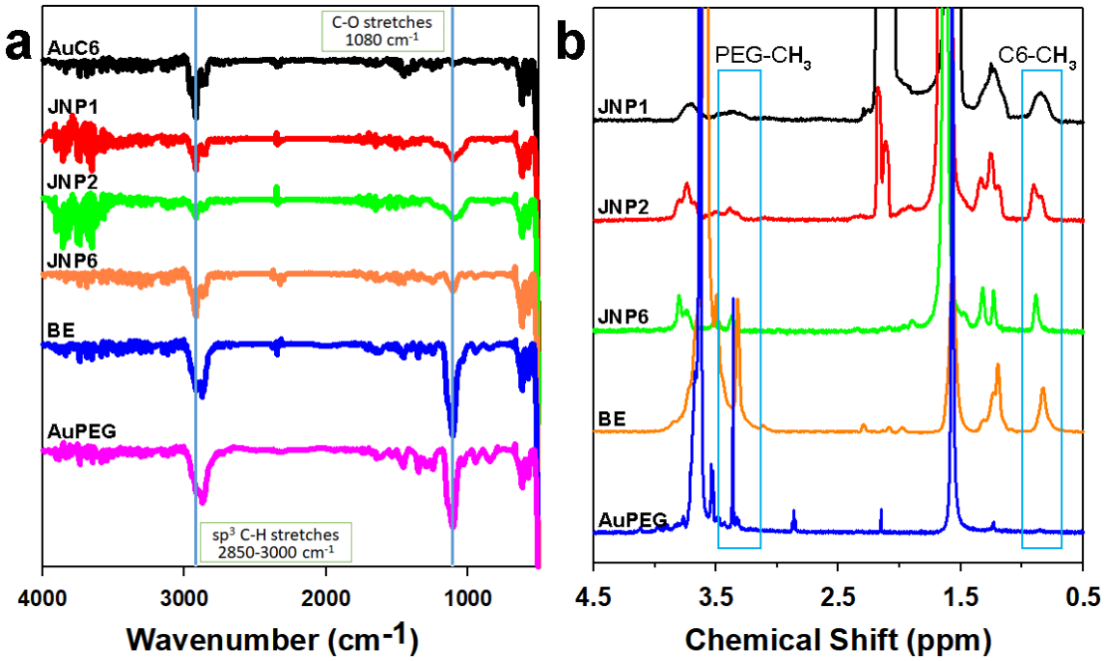

Figure 4.3. (a) FTIR spectra of various nanoparticles, and (b) ^{1}H NMR spectra in $CDCl_3$ of organic capping ligands (i.e., PEG, and C6) desorbed from the surface of various nanoparticles by iodine.

Interestingly, upon the addition of alkali metal ions, the nanoparticle structures exhibited a marked variation, as manifested in DLS measurements**.** Note that based on the Flory radius, the PEG ligands most likely adopted the brush conformation on the Janus nanoparticle surface within the PEG hemisphere, but a mushroom conformation at the PEG/C6 interface [19]. From **Figure 4.4**, it can be seen that the hydrodynamic radius (R_H) of the JNP6 nanoparticles remained virtually unchanged at around 100 nm in the presence of Li^+ and Rb^+ even at the metal ion/ethylene oxide (M^+/EO) ratio of

150, but increased markedly upon the addition of K^+, for instance, to ca. 300 nm at the K^+/EO ratio of 30 and remained largely saturated at higher K^+ concentrations. More drastic enhancement of R_H can be seen with the addition of Na^+, where R_H was about 400 nm at Na^+/EO = 30. Note that for the free PEGSH ligands, the R_H was almost unchanged (80-100 nm) even with the addition of these four alkali metal ions at M^+/EO = 150, suggesting that the markedly enhanced R_H of JNP6 cannot be accounted for by metal ion-induced conformational transitions of the PEG fragment. Rather, it is likely that the binding of select alkali metal ions led to the formation of organized assembly of the nanoparticles (*vide infra*). Such a variation of the R_H change can be attributed to the different "cloud point" effect on the PEG chain upon the addition of different alkali metal ions [27-29], which has been found to decrease in the order of $K^+ > Rb^+ > Cs^+ > Na^+ > Li^+$ [29]. The fact that R_H remains invariant upon the addition of Li^+ suggests that the PEG conformation is mostly insensitive of the PEG-Li interaction [28]; yet upon the addition of Na^+ and K^+, the significant R_H variations observed indicate drastic structural change of PEG, where the enhanced rigidity of the PEG segments facilitated the exposure of the hydrophobic C6 ligands and resulted in the self-assembly of JNP6 forming organized ensembles (Figure 4a) [21-23,30,31]. In contrast, due to the large atomic radius of Rb^+, the ions mostly interacted only with the outer portion of the PEG chain instead of diffusing into the interior, and the resulting conformational change of PEG was not sufficient to lead to self-assembly of JNP6. In fact, one can see that the BE nanoparticles, despite a similar PEG surface coverage to that of JNP6 but with ligands homogeneously mixed on the nanoparticle surface, showed no variation of the R_H even

at M^+/EO up to 150. Furthermore, JNP1, JNP2 and AuPEG showed rather consistent R_H (80-100 nm), and the radii did not change appreciably with the ion concentration increased to M^+/EO = 150. This suggests that (i) the PEG coverage on the nanoparticle surface did not impact the R_H significantly, and (ii) no organized assembly was formed for these nanoparticles, likely because low amphiphilicity of JNP1 and JNP2, and monofunctionalization of AuPEG.

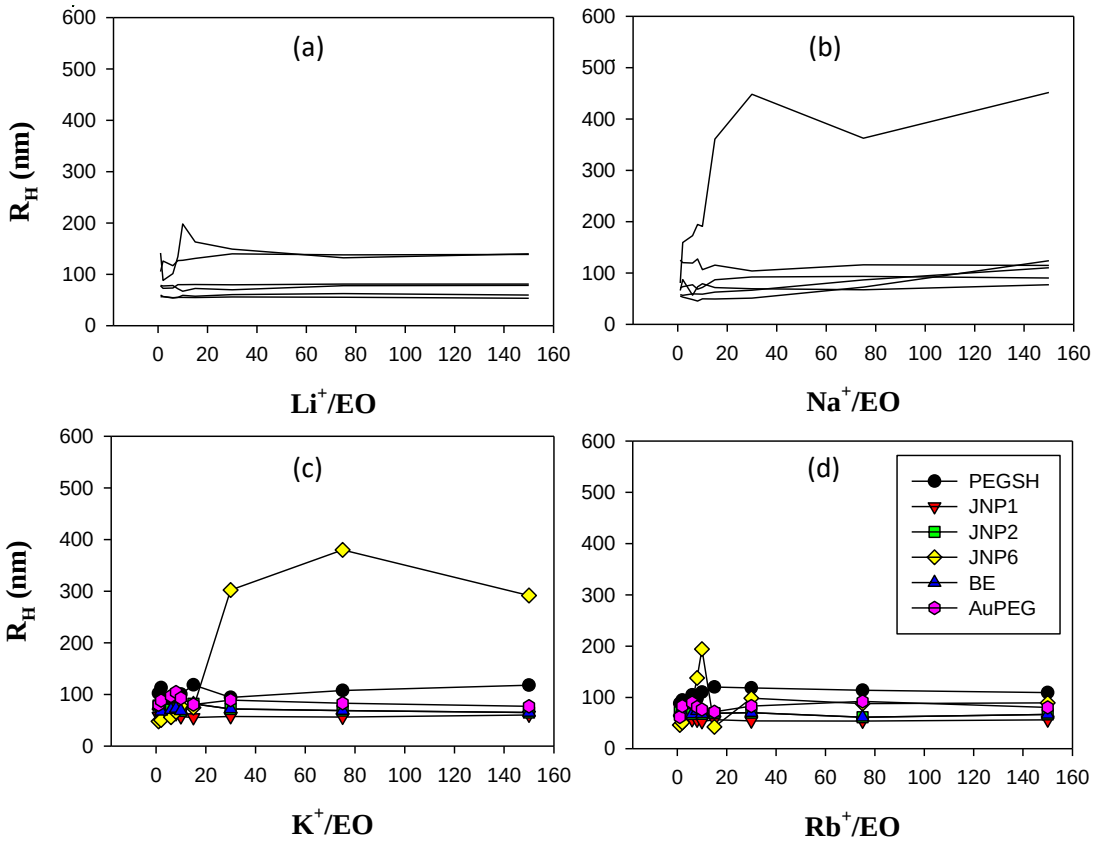

Figure 4.4. Hydrodynamic radii of PEGSH ligands and nanoparticles (0.015 mg/mL in water) upon the addition of (a) Li^+, (b) Na^+, (c) K^+, and (d) Rb^+ at different concentrations (expressed as the ratio of alkali metal ions to ethylene oxide units).

Consistent results were obtained in TEM measurements. From the TEM micrographs in **Figure 4.5**, one can see that after the addition of Na^+ at Na^+/EO = 30, JNP1 and JNP2 remained well dispersed without apparent agglomeration (panels a and b), similar to that with BE nanoparticles (panel d), whereas formation of nanoparticle ensembles (a few hundred nm across) was apparent with JNP6 nanoparticles (panel c). It should be noted that in the absence of alkali metal cations, JNP6 nanoparticles were well dispersed in water without apparent agglomeration (**Figure 4.6**). This is different from the behaviors that we observed earlier with JNPs capped with short hydrophilic ligands (e.g., 3-mercapto-1,2-propanediol), where the nanoparticles were found to self-assemble into organized ensembles even in the absence of metal ions [21,22,32]. Such a discrepancy suggests that the AuC6-PEG JNP6 nanoparticles did not exhibit amphiphilic characters in solution, most likely due to the long, flexible PEG chains that extended over the C6 hemisphere and limited the exposure of the hydrophobic C6 ligands.

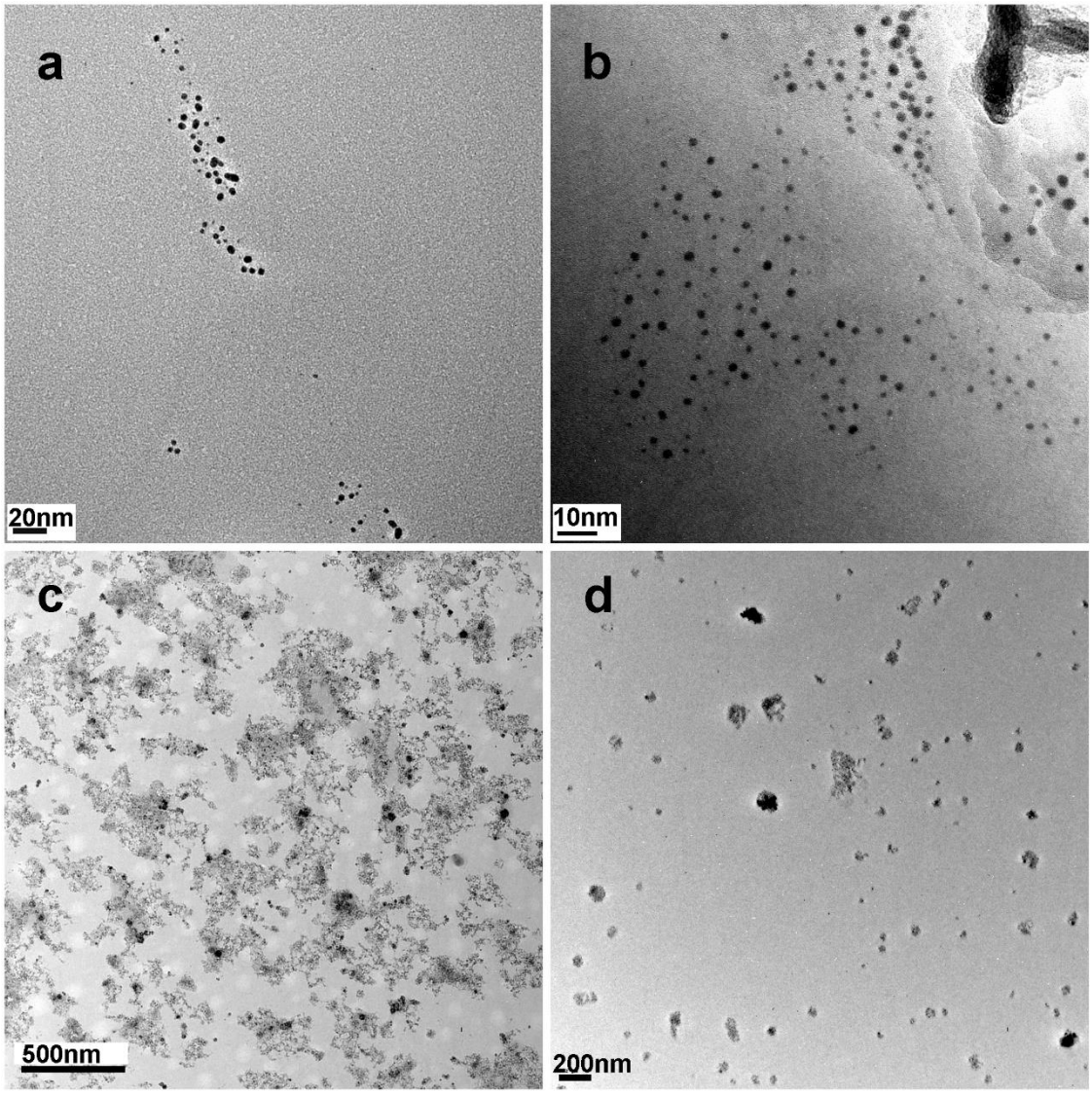

Figure 4.5. TEM images of (a) JNP1,(b) JNP2, (c) JNP6 and (d) BE upon addition of Na^+ at the Na^+/EO ratio of 30. Nanoparticle concentrations all 0.015 mg/mL in water.

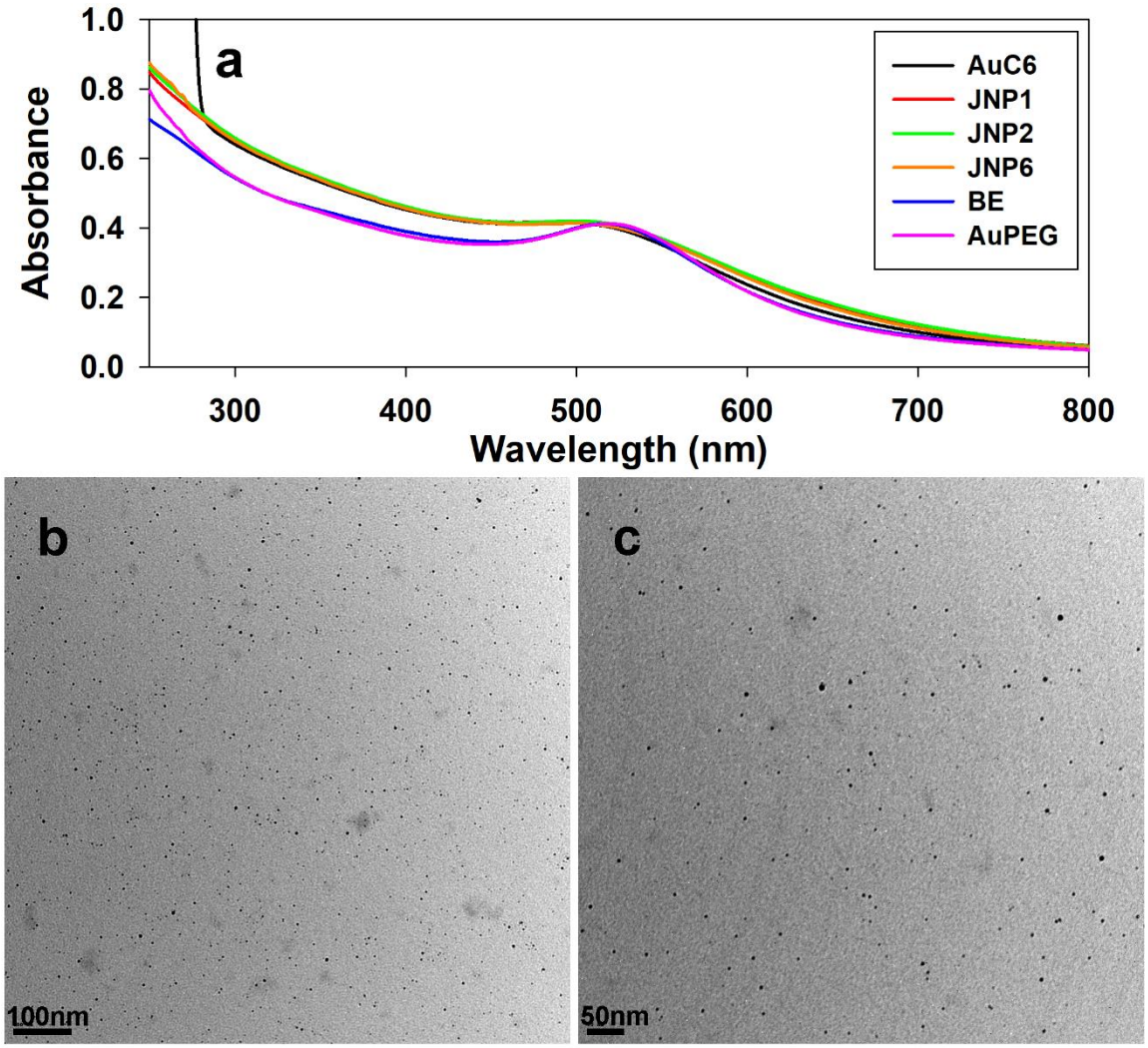

Figure 4.6. (a) UV-vis spectra of the series of nanoparticles, and TEM images of (b) JNP6 and (c) BE nanoparticles. From the TEM images, it can be seen that the nanoparticles are individually dispersed without apparent agglomeration, in good agreement with UV-vis absorption profiles.

Such structural variations are schematically depicted in **Figure 4.4a**. Because of the long chain legth of the PEG ligands in comparision to C6, the PEG ligands on as-prepared JNP6 likely adopted a mushroom conformation, especially at the PEG/C6

interface, thus rendering the nanoparticles individually dispersible in water. Upon the addition of select alkali metal ions such as Na^+, the PEG chains became structurally rigid [7], which led to exposure of the hydrophobic C6 ligands. The resulting amphiphilic characters of the nanoparticles allowed self-assembly of the nanoparticles into organized ensembles, akin to conventional surfactant molecules [21,22,32]. Lesser effects were observed with other metal ions, suggesting insignificant conformational change of the PEG ligands [28]. In fact, results from UV-vis absorption studies (**Figure 4.7b** and **4.6**) show that in the absence of alkali metal ions, the JNP6 nanoparticles exhibited a surface plasmon resonance (SPR) at ca. 520 nm, characteristic of well dispersed gold nanoparticles [33]; and upon the addition of Na^+, the SPR peak can be seen to become broadened and red-shift to 550 nm, two signatory behaviors of the formation of nanoparticle ensembles [32]. In addition, the relatively small SPR shift of JNP6 (from 520 nm to 550 nm) in comparison to that observed in the previous studies with much shorter hydrophilic ligands (> 600nm) [21,22] is also in agreement with the formation of small nanoparticle ensembles, as seen in the TEM images (**Figure 4.5c**). By sharp contrast, no apparent variation was observed for other nanoparticles in the series (i.e., JNP1, JNP2, BE, and AuPEG), suggesting the lack of ensemble formation of these samples, again, in good agreement with the TEM results (**Figure 4.5a, b, and d**).

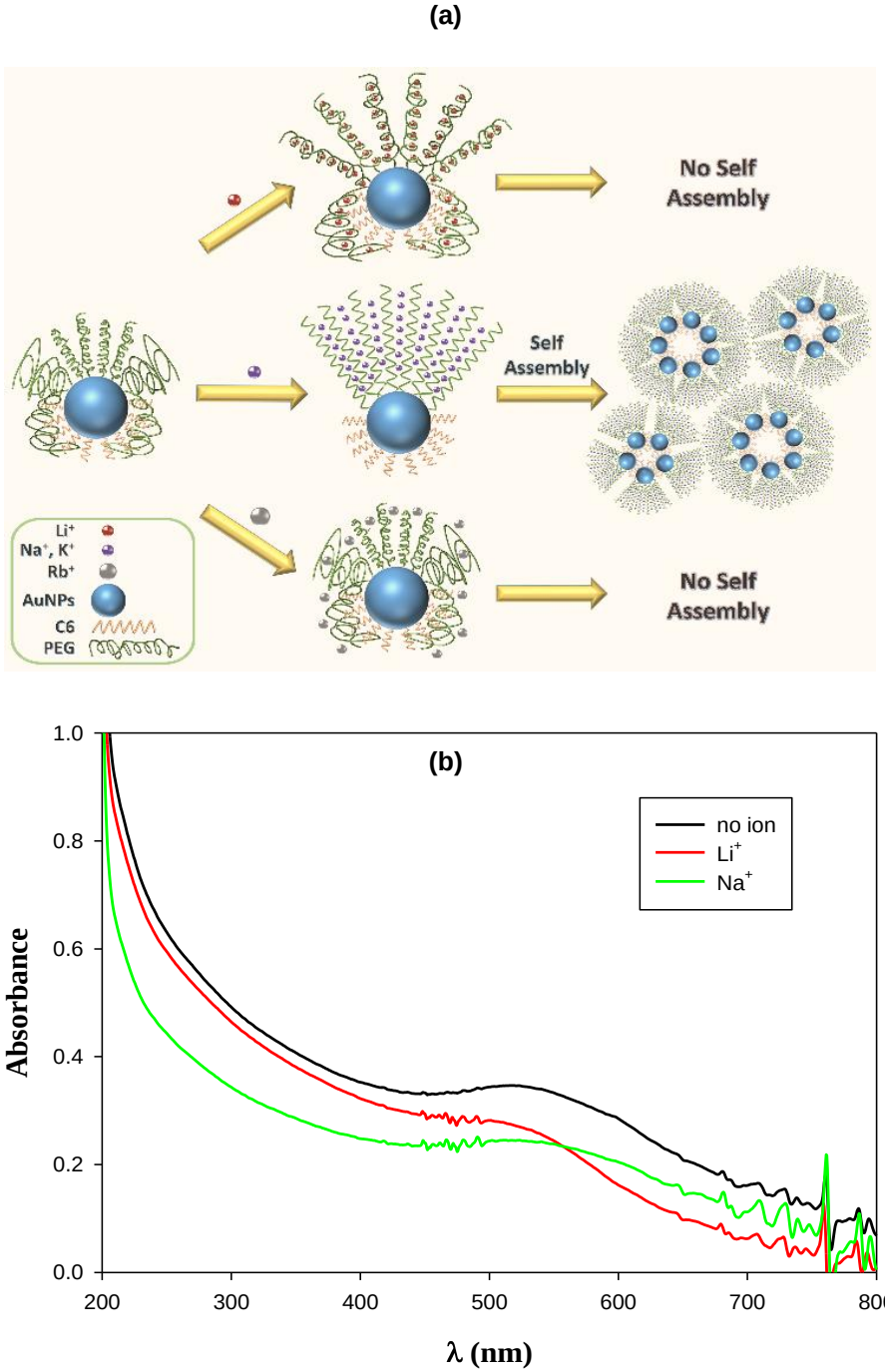

Figure 4.7. (a) Schematic of alkali metal ions induced self-assembly of PEG-functionalized Janus nanoparticles. (b) UV-vis absorption spectra of JNP6 nanoparticles in the absence and presence of Li^+ and Na^+ at the M^+/EO ratio of 30. Nanoparticle concentration 0.015 mg/mL in water.

The interactions of alkali metal ions with the PEG ligands can also be probed by the change of chemical shift and peak broadening/splitting in NMR measurements [34-38]. In general, the chemical shift indicates the interaction strength between different species, and in the present study, the interaction between PEG and alkali metal ions [39]. On the other hand, the sharpness of NMR peaks can be correlated to the coupling of neighboring protons, where enhanced dipolar coupling between neighboring protons leads to broadening and even splitting of a peak signal [34]. From **Figure 4.8a**, one can see that prior to the addition of alkali metal ions, the PEGSH ligands, AuPEG and JNP6 all show a peak at 3.55 ppm, which can be ascribed to the ethylene protons (-C**H**$_2$-C**H**$_2$-O-) of the PEG chains [40]. The appearance of a sharp singlet is most likely due to the formation of a stable distotic nematic (N_D) phase of the long polymer chains at room temperature [7] and hence chemical equivalence of the ethylene protons due to the fast proton exchance rate [34]. Interestingly, upon the addition of Li^+ and Na^+ ions the ethylene proton peak was broadened, and split into a semi-doublet, indicating chemical inequivalence of the ethylene protons that most likely arose from the formation of PEG-ion complexes. This may be ascribed to a phase transition of PEG from its stable N_D phase to hexagonal columnar (Col_h) phase [7], which lowered the chain mobility by electronic attraction between the cations and PEG [41]. Similar behaviors have been observed in previous studies with crown ethers, where upon coordination with alkali metal ions, the NMR signal of the ethylene protons (3.73 ppm) was found to split into two sets of signals (3.50/3.78 ppm for Na^+ and 3.68/3.83 ppm for Li^+) [36]. In the present

study, the chemical shift of the ethylene protons of PEGSH can be seen to move downfield to 3.66 ppm and 3.61 ppm upon the addition of Li^+ and Na^+, respectively, indicating comparable, apparent interaction between PEG and the the ions due to the formation of PEG-cation complex, where the deshielding effect lowered the electron density around the ethylene protons of adjacent carbons [39]. The slightly smaller shift for Na^+ can be correlated to the cloud point effect for the PEG ligands upon the addition of Na^+, where the PEG-Na^+ complexation was achieved by two neighboring PEG chains brought together by the cloud point effect, which lessened the deshielding effect of the PEG protons and reduced the downfield shift. In contrast, the cloud point effect on the PEGSH ligands in the presence of Li^+ is minimal (no PEG aggregation, as shown in **Figure 4.4**), so the deshielding effect on PEGSH proton is larger due to stronger interaction between the oxygen on PEGSH (most likely on the same polymer chain) and Li^+.

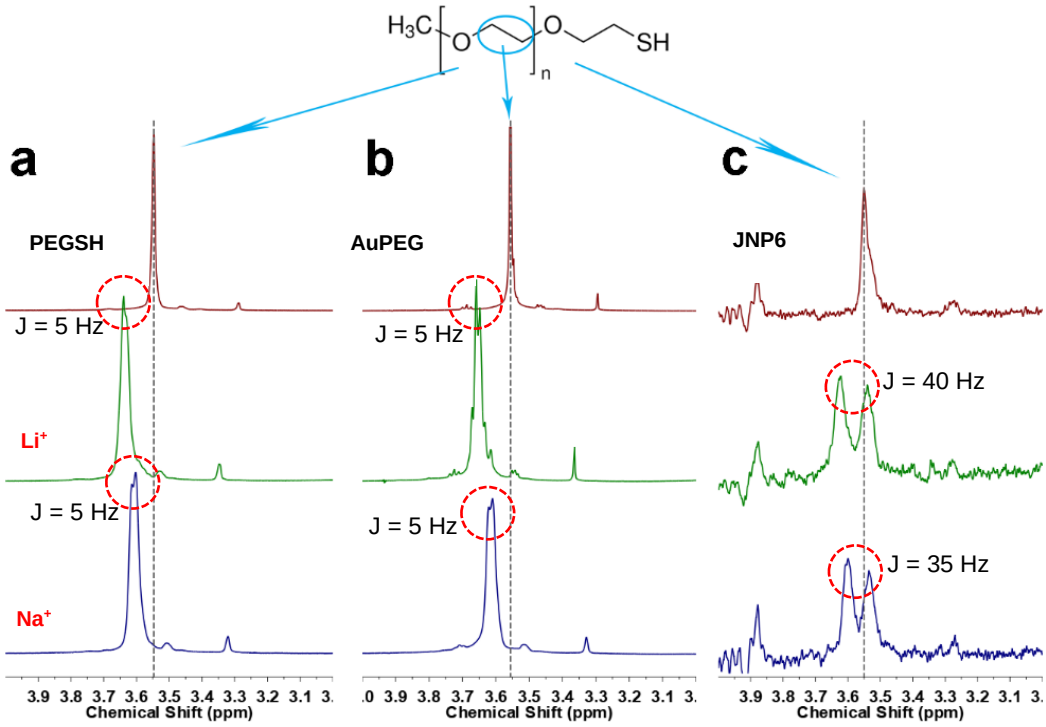

Figure 4.8. ^{1}H NMR spectra of (a) PEGSH, (b) AuPEG and (c) JNP6 in the absence (top curves) and presence of Li^+ (middle curves) and Na^+ (bottom curves) in CD_3CN at $M^+/EO = 30$.

Similar behaviors were observed with AuPEG, where the ethylene peaks were shifted to 3.64 ppm and 3.61 ppm upon the addition of Li^+ and Na^+ ions, respectively (Figure 8b), indicating similar ion binding behaviors between free PEGSH ligands and those bound onto the AuPEG nanoparticle surface. Nevertheless, one can see that the splitting of the ethylene protons for AuPEG upon the interaction with Li^+ became better defined with a coupling constant of J = 5 Hz (which is similar to that of free PEGSH ligands). This chemical inequivalence of the ethylene proton demonstrated that the specific binding of Li^+ ion to the PEG structure brought the ethylene protons closer to each other by slowing the PEG chain mobility and hence led to apparent dipolar

coupling between protons attached on the adjacent carbons [40]. By contrast, the peak splitting was slightly less significant with Na^+, likely due to the larger size of Na^+ forming larger PEG-cation complex, which results in weaker inter- / intra-molecular coupling between protons. Furthermore, the high PEG content on AuPEG might also limit the Na^+ diffusion into the interior of the PEG capping layer, thus the change of chain mobility and chemical environment for ethylene proton were not as high as for the Li^+-doped sample.

For JNP6, the spiltting was far more prounced (**Figure 4.8c**). Specifically, upon the addition of Li^+ and Na^+ ions, the ethylene proton peak splits into a broad and well-defined doublet, at 3.54/3.62 ppm and 3.53/3.60 ppm, with a coupling constant of J = 40 Hz and 35 Hz, respectively. This suggests a much enhanced incorporation of alkali metal ions forming stable PEG-cation complexes that highly reduced the PEG chain mobility, thus enhanced the differentiation of the protons on the same methylene carbon, leading to strong dipolar coupling between protons attached on the same carbon (i.e., H_a–$H_{a'}$ and H_b–$H_{b'}$ for –O-C**$H_aH_{a'}$**-C**$H_bH_{b'}$**-O-) [37,38]. Unlike the coupling between protons attached to adjacent carbons, chemical inequivalence of protons on the same carbon without a chiral center is a strong indication of the formation of an organized coordination structure with one proton interacting with the metal center while the other is not (pointing outwards in a crown-ether-like / helical structure) [34]. This different proton positioning resulted in chemical inequivalence which gave rise to the broadening of the doublet signal. The markedly greater peak broadening and splitting observed with JNP6, in comparison to AuPEG, can be attributed to the ligand

segregation on JNP6 that facilitates metal cation incorporation forming stable PEG-cation complexes, which limits the chain mobility and results in more apparent signal change.

4.5 Conclusion

In this study, AuC6-PEG Janus nanoparticles with a PEG hemisphere showed unique binding affinity to alkali metal ions. The as-prepared Janus nanoparticles were found to be individually dispersed in water, likely due to the much longer PEG ligands that adopted a mushroom conformation, especially at the PEG/C6 ligand interface. Upon the addition of select alkali metal ions (e.g., Na^+), the formation of PEG-cation complex led to enhanced rigidity of the PEG ligand chains, and hence exposure of the hydrophobic C6 hemisphere. The resulting amphiphilic characters rendered the nanoparticles to self-assemble into organized ensembles, as manifested in DLS and TEM measurements and further confirmed by NMR measurements. These unique properties may be exploited for select chemical doping of PEG-functionalized nanoparticles, controlled assembly of the nanoparticles, as well as chemical sensing of alkali metal ions.

4.6 References

(1) Suk, J. S.; Xu, Q. G.; Kim, N.; Hanes, J.; Ensign, L. M. PEGylation as a strategy for improving nanoparticle-based drug and gene delivery. *Adv Drug Deliver Rev* **2016**, *99*, 28-51.

(2) Xue, Z. G.; He, D.; Xie, X. L. Poly(ethylene oxide)-based electrolytes for lithium-ion batteries. *J Mater Chem A* **2015**, *3*, 19218-19253.

(3) Stephan, A. M. Review on gel polymer electrolytes for lithium batteries. *Eur Polym J* **2006**, *42*, 21-42.

(4) Zhang, C. H.; Gamble, S.; Ainsworth, D.; Slawin, A. M. Z.; Andreev, Y. G.; Bruce, P. G. Alkali metal crystalline polymer electrolytes. *Nat Mater* **2009**, *8*, 580-584.

(5) Li, H.; Ma, X. T.; Shi, J. L.; Yao, Z. K.; Zhu, B. K.; Zhu, L. P. Preparation and properties of poly(ethylene oxide) gel filled polypropylene separators and their corresponding gel polymer electrolytes for Li-ion batteries. *Electrochim Acta* **2011**, *56*, 2641-2647.

(6) Saikia, D.; Wu, H. Y.; Pan, Y. C.; Lin, C. P.; Huang, K. P.; Chen, K. N.; Fey, G. T. K.; Kao, H. M. Highly conductive and electrochemically stable plasticized blend polymer electrolytes based on PVdF-HFP and triblock copolymer PPG-PEG-PPG diamine for Li-ion batteries. *J Power Sources* **2011**, *196*, 2826-2834.

(7) Kohmoto, S.; Mori, E.; Kishikawa, K. Room-temperature discotic nematic liquid crystals over a wide temperature range: Alkali-metal-ion-induced phase transition from discotic nematic to columnar phases. *J Am Chem Soc* **2007**, *129*, 13364-+.

(8) Rundqvist, J.; Hoh, J. H.; Haviland, D. B. Poly(ethylene glycol) self-assembled monolayer island growth. *Langmuir* **2005**, *21*, 2981-2987.

(9) Fan, J. B.; Long, F.; Liang, Z. W.; Aldred, M. P.; Zhu, M. Q. Hierarchical mesostructures of biodegradable triblock copolymers via evaporation-induced self-assembly directed by alkali metal ions. *Colloid Polym Sci* **2012**, *290*, 1637-1646.

(10) Inokuchi, Y.; Boyarkin, O. V.; Kusaka, R.; Haino, T.; Ebata, T.; Rizzo, T. R. UV and IR Spectroscopic Studies of Cold Alkali Metal Ion-Crown Ether Complexes in the Gas Phase. *J Am Chem Soc* **2011**, *133*, 12256-12263.

(11) Hamilton, G. R. C.; Sahoo, S. K.; Kamila, S.; Singh, N.; Kaur, N.; Hyland, B. W.; Callan, J. F. Optical probes for the detection of protons, and alkali and alkaline earth metal cations. *Chem Soc Rev* **2015**, *44*, 4415-4432.

(12) Cai, Z. Z.; Do, L. H. Customizing Polyolefin Morphology by Selective Pairing of Alkali Ions with Nickel Phenoxyimine-Polyethylene Glycol Catalysts. *Organometallics* **2017**, *36*, 4691-4698.

(13) Parker, J. M.; Wright, P. V.; Lee, C. C. A Double Helical Model for Some Alkali-Metal Ion-Poly(Ethylene Oxide) Complexes. *Polymer* **1981**, *22*, 1305-1307.

(14) Shimada, K.; Matsuyama, S.; Saito, T.; Kinugasa, S.; Nagahata, R.; Kawabata, S. Conformational effects on cationization of poly(ethylene glycol) by alkali metal ions in matrix-assisted laser desorption/ionization time-of-flight mass spectrometry. *Int J Mass Spectrom* **2005**, *247*, 85-92.

(15) Terashima, T.; Kawabe, M.; Miyabara, Y.; Yoda, H.; Sawamoto, M. Polymeric pseudo-crown ether for cation recognition via cation template-assisted cyclopolymerization. *Nat Commun* **2013**, *4*.

(16) Poudel, L.; Podgornik, R.; Ching, W. Y. The Hydration Effect and Selectivity of Alkali Metal Ions on Poly(ethylene glycol) Models in Cyclic and Linear Topology. *J Phys Chem A* **2017**, *121*, 4721-4731.

(17) Chai, L.; Goldberg, R.; Kampft, N.; Klein, J. Selective adsorption of poly(ethylene oxide) onto a charged surface mediated by alkali metal ions. *Langmuir* **2008**, *24*, 1570-1576.

(18) de Gennes, P. G. Polymers at an interface; a simplified view. *Advances in Colloid and Interface Science* **1987**, *27*, 189-209.

(19) Jokerst, J. V.; Lobovkina, T.; Zare, R. N.; Gambhir, S. S. Nanoparticle PEGylation for imaging and therapy. *Nanomedicine-Uk* **2011**, *6*, 715-728.

(20) Brust, M.; Walker, M.; Bethell, D.; Schiffrin, D. J.; Whyman, R. Synthesis of Thiol-Derivatized Gold Nanoparticles in a 2-Phase Liquid-Liquid System. *J Chem Soc Chem Comm* **1994**, 801-802.

(21) Lu, J. E.; Yang, C. H.; Wang, H. B.; Yam, C. Y.; Yu, Z. G.; Chen, S. W. Plasmonic circular dichroism of vesicle-like nanostructures by the template-less self-assembly of achiral Janus nanoparticles. *Nanoscale* **2018**, *10*, 14586-14593.

(22) Lu, J. E.; Peng, Y.; Chen, S. W. Janus Nanoparticle Emulsions as Chiral Nanoreactors for Enantiomerically Selective Ligand Exchange. *Part Part Syst Char* **2019**, 1800564.

(23) Pradhan, S.; Xu, L. P.; Chen, S. W. Janus nanoparticles by interfacial engineering. *Adv Funct Mater* **2007**, *17*, 2385-2392.

(24) Song, Y.; Liu, K.; Chen, S. W. AgAu Bimetallic Janus Nanoparticles and Their Electrocatalytic Activity for Oxygen Reduction in Alkaline Media. *Langmuir* **2012**, *28*, 17143-17152.

(25) Silverstein, R. M.: *Spectrometric Identification of Organic Compounds*; Seventh ed.; John Wiley & Sons, Inc., 2005; Vol. 1. pp. 72-126.

(26) Chieng, B. W.; Ibrahim, N. A.; Yunus, W. M. Z. W.; Hussein, M. Z. Poly(lactic acid)/Poly(ethylene glycol) Polymer Nanocomposites: Effects of Graphene Nanoplatelets. *Polymers-Basel* **2014**, *6*, 93-104.

(27) Florin, E.; Kjellander, R.; Eriksson, J. C. Salt effects on the cloud point of the poly(ethylene oxide)+ water system. *Journal of the Chemical Society, Faraday Transactions 1: Physical Chemistry in Condensed Phases* **1984**, *80*, 2889-2910.

(28) Masuda, Y.; Nakanishi, T. Ion-specific swelling behavior of poly(ethylene oxide) gel and the correlation to the intrinsic viscosity of the polymer in salt solutions. *Colloid Polym Sci* **2002**, *280*, 547-553.

(29) Ren, C.-l.; Tian, W.-d.; Szleifer, I.; Ma, Y.-q. Specific Salt Effects on Poly(ethylene oxide) Electrolyte Solutions. *Macromolecules* **2011**, *44*, 1719-1727.

(30) Xu, Q.; Kang, X. W.; Bogomolni, R. A.; Chen, S. W. Controlled Assembly of Janus Nanoparticles. *Langmuir* **2010**, *26*, 14923-14928.

(31) Song, Y.; Chen, S. W. Janus Nanoparticles: Preparation, Characterization, and Applications. *Chem-Asian J* **2014**, *9*, 418-430.

(32) Song, Y.; Chen, S. W. Janus Nanoparticles as Versatile Phase-Transfer Reagents. *Langmuir* **2014**, *30*, 6389-6397.

(33) Creighton, J. A.; Eadon, D. G. Ultraviolet Visible Absorption-Spectra of the Colloidal Metallic Elements. *Journal of the Chemical Society-Faraday Transactions* **1991**, *87*, 3881-3891.

(34) Flodstrom, K.; Wennerstrom, H.; Alfredsson, V. Mechanism of mesoporous silica formation. A time-resolved NMR and TEM study of silica-block copolymer aggregation. *Langmuir* **2004**, *20*, 680-688.

(35) Tiritiris, I.; Schleid, T.; Muller, K. Solid-state NMR studies on ionic closo-dodecaborates. *Appl Magn Reson* **2007**, *32*, 459-481.

(36) Brachvogel, R. C.; Maid, H.; von Delius, M. NMR Studies on Li+, Na+ and K+ Complexes of Orthoester Cryptand o-Me-2-1.1.1. *Int J Mol Sci* **2015**, *16*, 20641-20656.

(37) Yang, L. Y.; Fu, X. B.; Chen, T. Q.; Pan, L. K.; Ji, P.; Yao, Y. F.; Chen, Q. Ionic Conductivity of beta-Cyclodextrin-Polyethylene-Oxide/Alkali-Metal-Salt Complex. *Chem-Eur J* **2015**, *21*, 6346-6349.

(38) Lee, Y. J.; Ho, T. H.; Lai, C. C.; Chiu, S. H. Size effects in the alkali metal ion-templated formation of oligo(ethylene glycol)-containing [2]catenanes. *Org Biomol Chem* **2016**, *14*, 1153-1160.

(39) Wang, D. M.; Aso, Y.; Ohara, H.; Tanaka, T. Synthesis and Characterization of Alkali Metal Ion-Binding Copolymers Bearing Dibenzo-24-crown-8 Ether Moieties. *Polymers (Basel)* **2018**, *10*.

(40) Silverstein, R. M.; Webster, F. X.; Kiemle, D. J. Spectrometric Identification of Organic Compounds. **2005**, 502.

(41) Irandoust, M.; Daraei, H.; Rostamian, R. Proton NMR probing of stoichiometry and thermodynamic data for the complexation of Na+ and Li+ ions with 15-Crown-5 in acetonitrile-nitrobenzene mixtures. *Polyhedron* **2011**, *30*, 1207-1212.

Chapter 5
Chirally Active Janus $Cu_{1.75}S$-Au Hybrid Nanostructure and its Origin of Chirality

5.1 Abstract

Nanostructures with chiral core structure is interesting due to their high enantiomeric selectivity depending on their chirality. Janus $Cu_{1.75}S$-Au nanostructure was synthesized using Langmuir-Blodgett method at room temperature through ion exchange of gold atoms onto $Cu_{1.75}S$ nanoparticles. Positive chiroptical response arose around 600 nm closed to gold SPR absorption region, whereas the $Cu_{1.75}S$ nanoparticles shown no chiroptical response. TEM images shows deposition of gold on one side of the copper sulfide, forming Janus hybrid structure. Upon etching away the $Cu_{1.75}S$, the deposited gold nanostructure shown weak positive chiroptical response at the same region, indicating chiral origin was due to the asymmetric deposition of gold atoms. In addition, the chiroptical signal of asymmetric gold nanostructure was enhanced upon the formation of $Cu_{1.75}S$-Au hybrid nanostructure.

5.2 Introduction

Chiral nanostructures have been studied extensively in the past few decades due to it unique chiroptical response upon interaction of circularly polarized light (CPL), which can be applied in potential applications such as catalysis, sensing and optical devices [1-5]. In typical, chiroptical response of a nanostructure arises at the surface plasmon resonance (SPR) absorption of the structure [6,7]. Thus, noble metal nanostructures were studied extensively due to their strong SPR absorption in the visible range (400 – 800 nm), which can be simply detected by UV-vis spectroscopy and circular dichroism (CD)

spectroscopy. For example, some areas of interest in studying nanoparticle chirality are: a) achiral core protected by chiral ligands, b) achiral core and ligand interact with chiral molecules, c) individual nanoparticles with chiral core and d) achiral nanoparticles assembled into chiral structures [8].

Among all the chiral nanoparticle systems, nanoparticles with chiral core surface is interesting because they show exceptional enantiomeric selectivity of synthesizing product towards one of the two enantiomers by facilitating adsorption for starting material with specific chirality [3]. In general, the preparation of chiral nanostructures requires the presence of enantiomerically pure chiral molecules as guiding reagent for the growth of chiral nanomorphology [9,10], which implies that the activity of chiral nanostructure can be influenced by the chiral molecules. Thus, most studies on chiroptical response solely coming from the chiral morphology of nanostructures were done using theoretical calculations, where others studied nanostructures that were prepared by top-down methods such as laser lithography and chemical deposition of achiral nanoparticles [11].

In addition, chiroptical response can be originated by having multiple components in a system or having chiral arrangement of individual components in a system. For example, bi-metallic dimer structures show chiroptical response at both SPR absorption regions of metal nanoparticles upon interaction with chiral molecules [12], where other studies show chiroptical response originates from chiral arrangements of identical achiral nanostructures made with different materials [13]. In general, nanoparticles with zero- or one-dimensional structure (e.g. spherical and rod) have a surface electron

distribution symmetry [7]. Upon deposition of a different element on one side of the nanoparticle surface, the symmetry of surface electron distribution will be broken; thus, chiroptical response can be generated. Previously, Yao et. al synthesized glutathione protected Au-Pd bimetallic nanocluster and yield chiroptical response between 300 – 500 nm, where the Au-Pd (1-1) sample yield the strongest response with an intense CD minima at 340 nm and a maxima at 460 nm [14]. The chiroptical response was then confirmed using magnetic circular dichroism spectroscopy (MCD) to be real, and the origin of the response was attributed to the electronic transitions. However, the origin of resulting a positive cotton was not fully explained.

Copper as a common abundant noble metal with relatively low cost, its derivative copper sulfide nanodisks (Cu_xS, $1 < x < 2$) had been studied extensively for its preparation and potential applications in the past few decades, due to its unique semi-conducting properties and non-toxic chemical nature [15]. Depending on the copper and sulfur ratio within the structure, the lattice and chemical property of the resulting copper sulfide can be very different [16]. In typical, copper sulfide nanodisks have a longitude localized surface Plasmon resonance (LSPR) absorption peak in the near infrared (NIR) region, between 1000 – 1400 nm. This absorption peak is highly depended on the copper to sulfur ratio, and it is also known as the free hole densities within the structure [17]. This highly tunable NIR absorption peak has very unique optical properties and can be applied to various sensing and biomedical applications [15,18]. Furthermore, hybrid nanostructures of M-Cu_xS (M = Au, Ru, Pt) had been prepared in the past through phase segregation of elements with addition of sulfur source at high

temperatures ranging from 130°C to 250°C [19-21]. Such hybrid nanostructures shown good catalytic activities towards methanol oxidation [22] and hydrogen evolution [23]; however, the chiroptical properties of such hybrid nanostructures had not been studied before.

Within this study, Cu_xS will be used as the starting material for the room temperature deposition of gold atoms using Langmuir-Blodgett (LB) method. Then, the chiral origin of Janus Cu_xS-Au hybrid nanostructure will be studied by measuring the chirality of individual Cu_xS and Au components by CD spectroscopy.

5.3 Experimental

Chemicals. Copper (II) acetate monohydrate (CuOAc, Alfa Aesar, 98+%), trioctylphosphine oxide (TOPO, STREM CHEMICALS, 99%), hydrogen tetrachloroauric acid trihydrate ($HAuCl_4 \cdot 3H_2O$, Fisher, 99%), 1-octadecene (ODE, Merck KGaA, 91%), 1-dodecanethiol (DDT, Aldrich, 98%), trioctylphosphine (TOP, STREM cheicals, 97+%), D-alanine (D-ala, ACROS, 99+%), L-alanine (L-ala, ACROS, 99%), DL-alanine (DL-ala, ACROS, 99%), D-cysteine (D-cys, CHEM-IMPEX INT'L INC., 99.12%), and L-cysteine (L-cys, MATHESON COLEMAN & BELL) were used as received. All solvents used were purchased from commercial sources at their highest purities and used without further treatment. Water was supplied by a Barnstead Nanopure water system (18.3 MΩ·cm).

Synthesis of $Cu_{1.75}S$ Nanocrystals. Preparation of $Cu_{1.75}S$ Nanocrystals were done by mixing CuOAc (0.0488g, 0.244mmol), TOPO (1.00g, 2.59mmol) and ODE (30mL, 93.9mmol) in a three-neck round bottom flask [24]. The mixture was then degassed under nitrogen bubbling for 30 minutes. The mixture was then heated to 160^{o}C under stirring in an oil bath, followed by a quick injection of DDT (1mL, 4.17mmol). The mixture was then heated to 185^{o}C for 3.5 hours. The resulting product was purified by precipitating in methanol followed by centrifugation and re-dispersing in toluene.

Synthesis of Janus $Cu_{1.75}S$-Au nanocrystals (JNP). Janus $Cu_{1.75}S$-Au nanocrystals were prepared by interfacial engineering using Langmuir-Blodgett (LB) method. In typical, the $Cu_{1.75}S$ nanocrystals dispersed in toluene were deposited onto water surface of LB-trough. After evaporation of toluene, $Cu_{1.75}S$ nanocrystals were compressed to desired surface pressure forming monolayer with interparticle spacing between one to two fully extended chain-length of DDT ligands. A calculated amount of $HAuCl_4$ aqueous solution (0.1M) was then injected into the water phase for interfacial ion exchange reaction. The resulting Janus nanoparticles were then collected, purified and re-disperse in chloroform. As a control experiment, ion exchange reaction was also carried out by simply mixing the $Cu_{1.75}S$ nanocrystals (in chloroform) and $HAuCl_4$ (in water), which denoted as bulk exchange (BE) nanoparticles.

Etching of JNP sample. The selective etching process of copper sulfide was carried out using a previous reported method using TOP [25]. In typical, the dried JNP was suspended in toluene at a concentration of 1 mg / mL and transferred into a glove box. In the glove box, a calculated amount of TOP was then added to the mixture, and the

vial was withdrawn from the glove box. The mixture was allowed to expose to air for 10 minutes, then resealed and stirred overnight. The resulting particles were purified by centrifugation in methanol for three times to remove excess TOP, and re-dispersed in $CHCl_3$.

Characterization. Transmission electron microscopy (TEM) images were taken with the 200kV FEI monochromated F20 UT Tecnai to study the morphology of nanoparticles. Scanning transmission electron microscopy (STEM) studies were carried out to study the chemical composing of Janus nanoparticles, using a modified FEI Titan with double aberration correctors operated at 300kV using. STEM images were recorded with high angle annular darkfield (HAADF) detector with a convergence angle of 30 mrad, with a spatial resolution of 0.05 nm. Atomic force microscopic (AFM) studies were performed with a Molecular Imaging PicoLE SPM instrument. X-ray spectroscopic data was collected using a Rigaku SmartLab X-ray diffractometer. X-ray photoelectron spectroscopy (XPS) measurements were carried out by the K-alpha plus XPS PHI 5400 at Lawrence Berkeley National Laboratory. UV-vis absorption spectra were acquired using a PerkinElmer Lambda 35 UV/VIS Spectrometer. NIR spectroscopy measurements were carried out using Ocean Optics NIR256-2.5 spectrometer equipped with halogen light source (HL-2000-FHSA, Mikropack). Nuclear magnetic resonance (NMR, Bruker 500 MHz) studies were carried out to quantify ligand percentage composition on nanoparticle surface. Fourier-transformed infrared (FTIR) measurements were carried out with a PerkinElmer, Spectrum One spectrometer. Dynamic light scattering (DLS) measurements were carried out with a

Wyatt DynaPro NanoStar temperature-controlled micro-sampler. CD measurements were carried out with a JASCO J1500 CD spectrometer.

5.4 Results and Discussion

The as prepared $Cu_{1.75}S$ nanocrystal has a height of 3.5 nm by AFM (**Fig. 5.1a**) and core diameter of 7.2 ± 0.5 nm by TEM (**Fig. 5.1b**). AFM topography shows a relatively flat surface of $Cu_{1.75}S$, and the fact that the particle height is about one half of its core diameter indicates possible formation of nanodisk structure. HR-TEM reveals a lattice spacing of 1.95Å, corresponding to the $Cu_{1.75}S$ lattice plane of (0160) (**Fig. 5.1c**). Previously, the preparation for hybrid structure of M-Cu_xS (where M can be gold [19,26], ruthenium [20], and platinum [21]) were done by phase segregation of elements at high temperature. In this study, deposition of gold onto $Cu_{1.75}S$ forming Janus structure was accomplished using LB method at room temperature. In comparison to the flat surface of $Cu_{1.75}S$, the Janus $Cu_{1.75}S$-Au reveals an uneven surface by AFM topography surface, where the total height of Cu_xS about 4 nm (**Fig. 5.1d**). TEM images show that the average core diameter of Janus $Cu_{1.75}S$-Au increased to 8.8 ± 0.8 nm (**Fig. 5.1e**), which confirms the growth of gold prefers to be on the side of nanostructure, which also lead to the uneven surface topography shown in AFM study. HAADF-STEM studies were carried to further study the structural composition information of Janus $Cu_{1.75}S$-Au nanoparticles. At such high angles, the scattering of electrons becomes incoherent, which Bragg scattering can be neglected. Thus, the intensity of image contrast is mainly

contributed from individual atom scattering. Since the scattering cross section of each atom is directly related to its atomic number, the contrast of image is dependence of the atomic number of the element, which leading to the strong dependence of chemical composition of the specimen (Z-contrast). And the intensity dependence is approximately $Z^{3/2}$ [27]. The HAADF-STEM image of $Cu_{1.75}S$-Au show elements brighter and dimmer contrast. In this case, the heavier element (Au) has brighter contrast, while the lighter elements ($Cu_{1.75}S$) have dimmer contrast (Fig. 1f). In addition, lattice spacing of 1.95Å and 2.35Å correspond to lattice planes of (0160) for $Cu_{1.75}S$ and (111) for gold, indicating the deposition of gold does not change the original structure of $Cu_{1.75}S$.

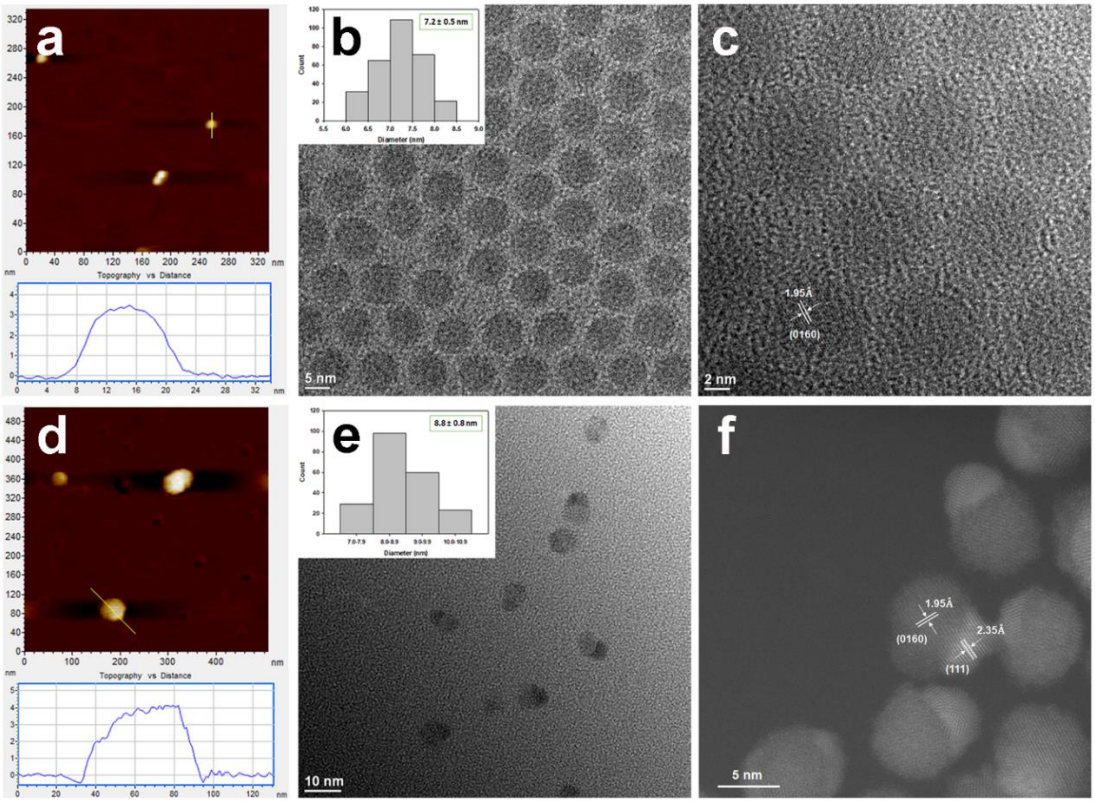

Figure 5.1. AFM topography of $Cu_{1.75}S$ (a) and JNP (d) with line scan at the bottom, TEM of $Cu_{1.75}S$ (b) and JNP (e) with diameter distribution (inset) and HR-TEM of $Cu_{1.75}S$ (c) and HAADF-STEM image of JNP (f).

XRD studies were carried out to study the overall chemical composition of each sample (**Fig. 5.2**). XRD pattern reveals that the as prepared product with a monoclinic structure of $Cu_{1.75}S$ (or Cu_7S_4, JCPDS No. 23-0958), with lattice constant of a =53.79Å, b = 30.90Å and c = 13.36Å, with $\alpha = \beta = \gamma = 90^o$. The diffraction peaks at $2\theta = 26.6^o$, 29.7^o, 31.2^o, 34.2^o, 46.8^o and 48.9^o are corresponding to the lattice planes of (1600), (804), (1821), (2001), (0160) and (886), respectively. The relatively broad peak patterns are attributed to the small crystalline size of $Cu_{1.75}S$ [28]. Upon deposition of gold onto

$Cu_{1.75}S$ using LB method, three new diffraction peaks arose at 2θ = 38.2°, 44.4° and 64.6°. These diffraction peaks reveal cubic gold structure with space group of Fm-3m (JCPDS No. 01-089-3697), and correspond to lattice planes of (111), (200) and (220), respectively. The lattice constant for such structure is a = b = c = 1.08Å, with α = β = γ = 90°. In addition, the diffraction peak profile of $Cu_{1.75}S$ remains unchanged, confirming that the deposition of gold onto the surface of $Cu_{1.75}S$ does not change the lattice structure of $Cu_{1.75}S$.

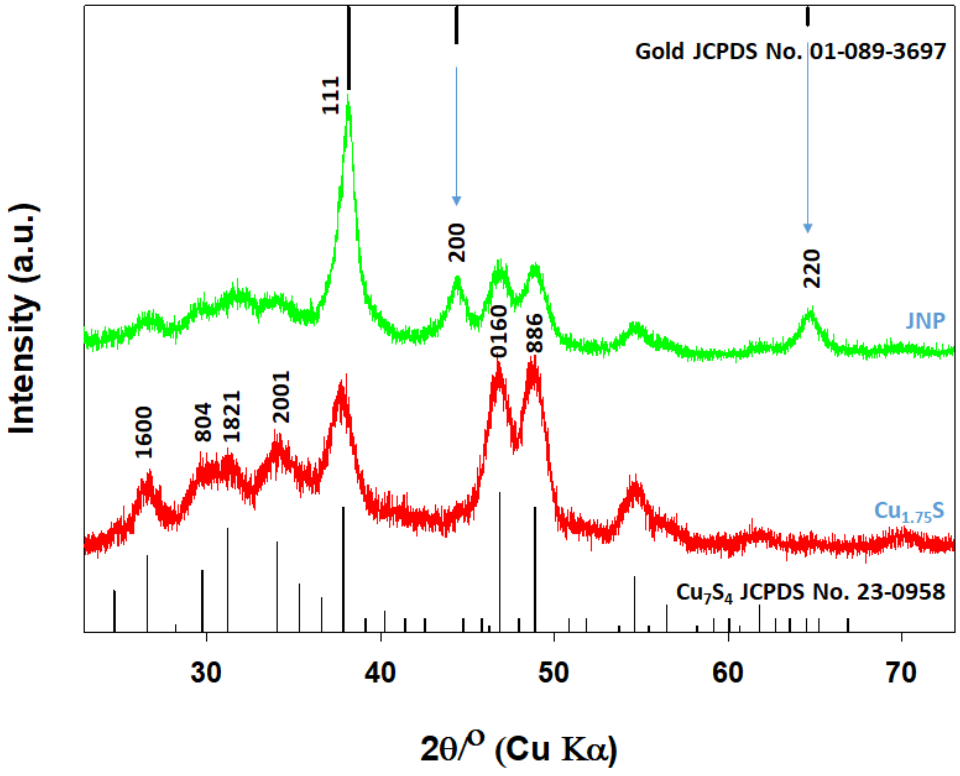

Figure 5.2. X-ray diffraction patterns of $Cu_{1.75}S$ (red) and JNP (green).

XPS analyses were carried out to study the surface composition of each sample (**Fig. 5.3**). For the as-prepared $Cu_{1.75}S$ sample, the binding energy of Cu2p is 953.2eV and 933.2eV, corresponding to oxidation state between Cu(I) and Cu(II) [29], while S2p3 has binding energy of 162.4eV and 161.4eV, corresponding to the S $2p_{1/2}$ and S $2p_{3/2}$ peaks [30]. Upon formation of Au-Cu alloys, both the binding energy of copper and gold will be lowered as the composition of gold increased [31]. For Janus $Cu_{1.75}S$-Au, the Cu $2p_{1/2}$ and Cu $2p_{3/2}$ peaks shifted to 953.1eV and 933.1eV, indicating reduction of copper atoms on the surface of JNP. In addition, the binding energy for Au 4f peaks were at 87.4eV and 83.8eV, while Au^0 binding energy is 84.0eV, can be attributed to the electron transfer from the semiconducting $Cu_{1.75}S$ to gold. In comparison, the binding energy of S $2p_{1/2}$ and S $2p_{3/2}$ peaks shifted to 163.2eV and 161.8eV, indicating oxidation of sulfur atoms on the surface of $Cu_{1.75}S$ initiates the attachment of gold onto $Cu_{1.75}S$, thus forming Janus nanostructure [32].

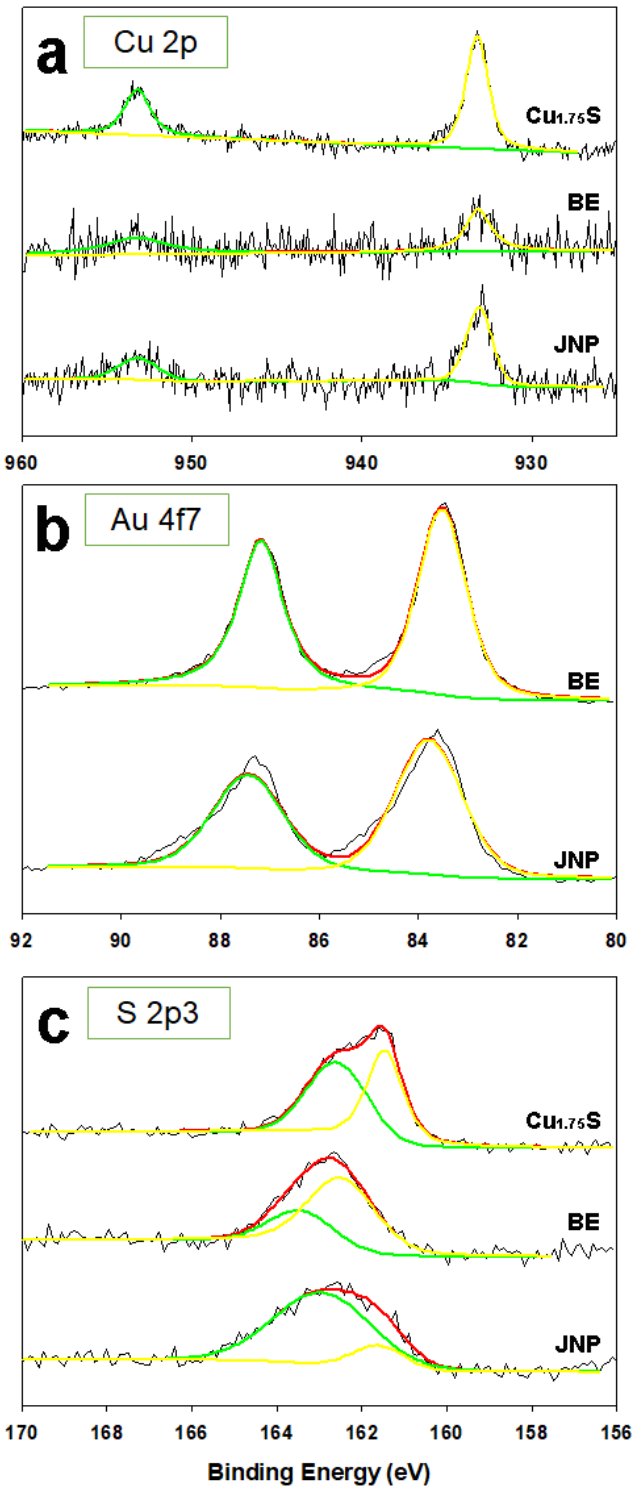

Figure 5.3. XPS measurements of $Cu_{1.75}S$, BE and JNP.

Optical property of $Cu_{1.75}S$ was carried out using UV-vis and NIR spectroscopy (**Fig. 5.4**). The exponential decade from 300 – 500 nm in the UV-vis spectrum indicates the small diameter of $Cu_{1.75}S$ (**Fig. 5.4a**) [24]. The JNP sample shows similar UV-vis absorption profile in comparison to $Cu_{1.75}S$. In contrast, a new shoulder peak at 300 nm arose for BE sample, along with an SPR absorption peak at 550 nm. The shoulder peak at 300 nm indicates the increase in nanoparticle diameter, in comparison to the exponential decade for the as-prepared $Cu_{1.75}S$. The SPR peak at 550 nm indicates the high composition of gold deposited onto the structure, thus leading to the appearance of gold SPR absorption. Note that there is no gold SPR absorption peak around 520 nm for JNP sample, possibly due to the amount of gold deposited onto $Cu_{1.75}S$ surface is too low for UV-vis detection. The inset image displays the color of each sample – the as prepared $Cu_{1.75}S$ displays a dark brown color, indicating small particle size. The JNP sample displays a lighter brown color, indicating the increased of particle diameter due to deposition of gold. In contrast, BE sample displays a purple-ish color, indicating aggregation of the BE sample, most likely due to the large amount of gold deposited onto the $Cu_{1.75}S$ structure. The increased of nanostructure diameters thus lowering their dispersity in solution. SEM images (**Fig. 5.5**) of JNP sample shows mostly individual nanoparticles, whereas BE sample shows aggregates of 200 – 400 nm in diameter. The large aggregations in BE sample increased the coupling of neighboring nanoparticles, thus red-shifts the gold SPR absorption to 550 nm in comparison to spherical gold nanoparticle SPR absorption around 520 nm (**Fig. 5.6**).

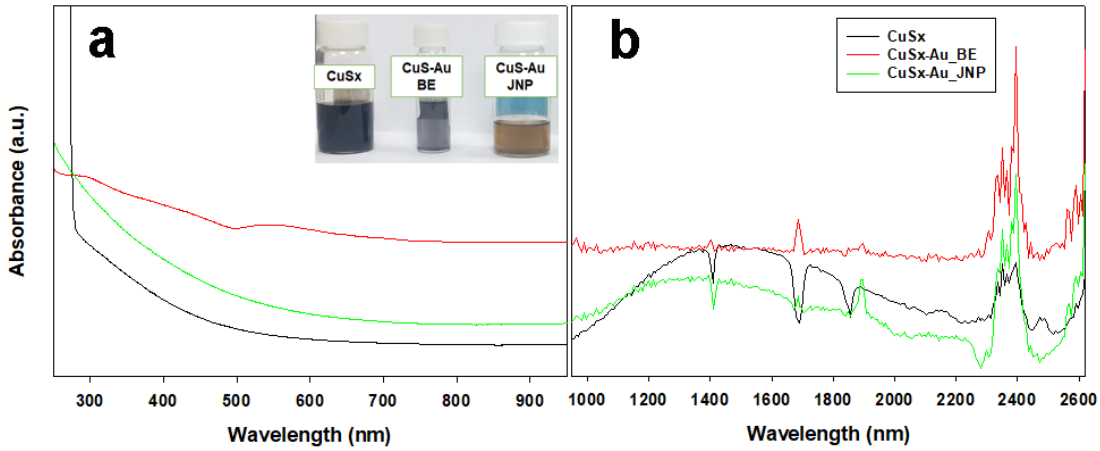

Figure 5.4. UV-vis (a), NIR (b) and CD (c) spectrum of $Cu_{1.75}S$ (black), BE (red) and JNP (green) in $CHCl_3$.

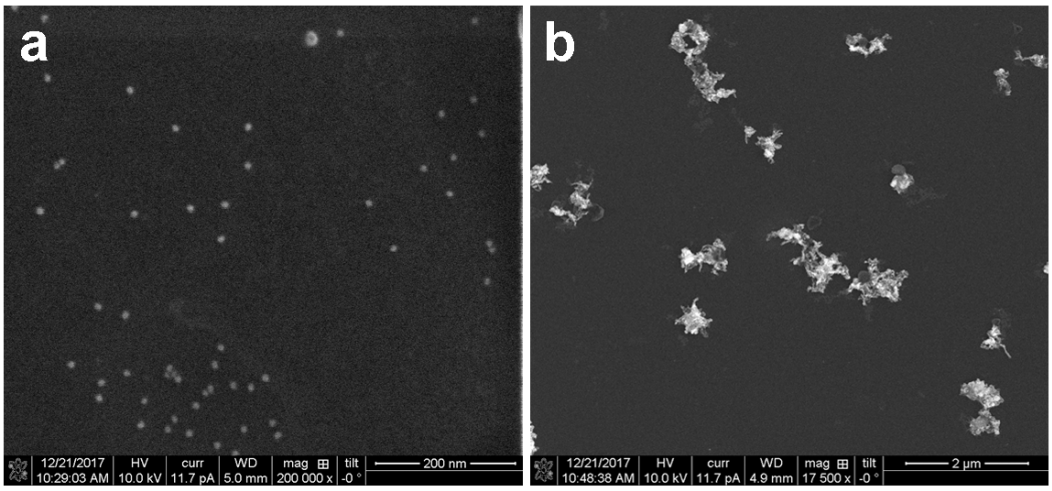

Figure 5.5. SEM image of JNP (a) and BE (b) in chloroform.

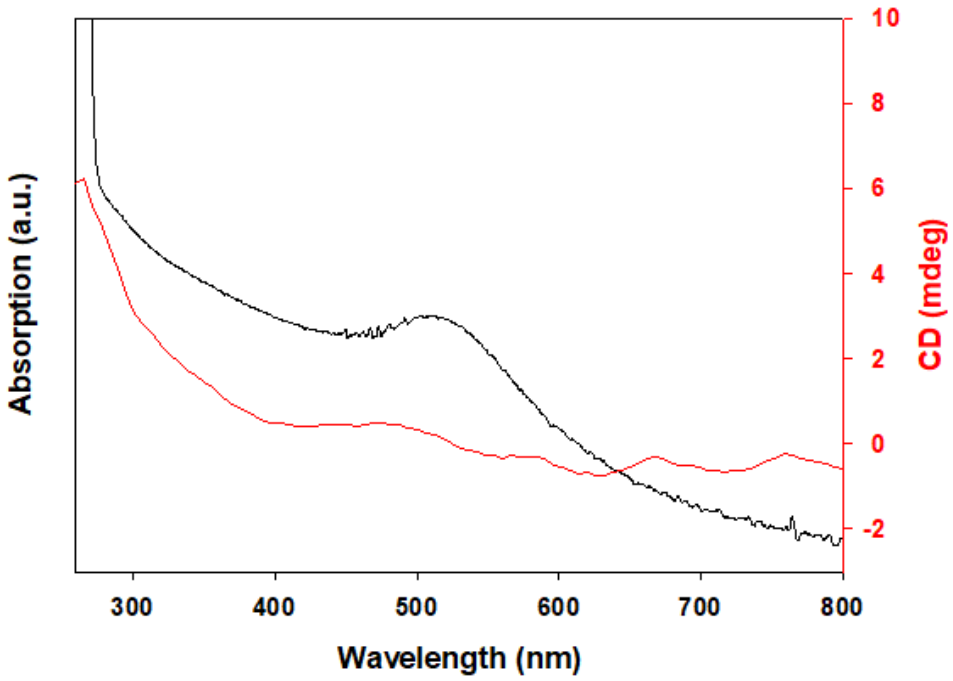

Figure 5.6. UV-vis absorption of AuC6 (black) and its corresponding CD spectrum (red) in $CHCl_3$.

The hydrodynamic radius for the above samples in $CHCl_3$ were carried to study the nanoparticle assembly property in solution phase (**Fig. 5.7**). DLS measurements reveal that the averaged hydrodynamic radius of the as-prepared $Cu_{1.75}S$ is 10.6 nm, indicating high dispersity of $Cu_{1.75}S$ in $CHCl_3$. After interfacial ion exchange reaction, the averaged hydrodynamic radius of JNP increased to 18.1 nm, indicating the increase of nanoparticle diameter due to deposition of gold, but the nanoparticles are still highly dispersed. In contrast, the BE sample shows an averaged hydrodynamic radius of 142.5 nm, indicating aggregation of nanoparticles. The hydrodynamic radius of each sample is in agreement with the UV-vis and TEM measurements.

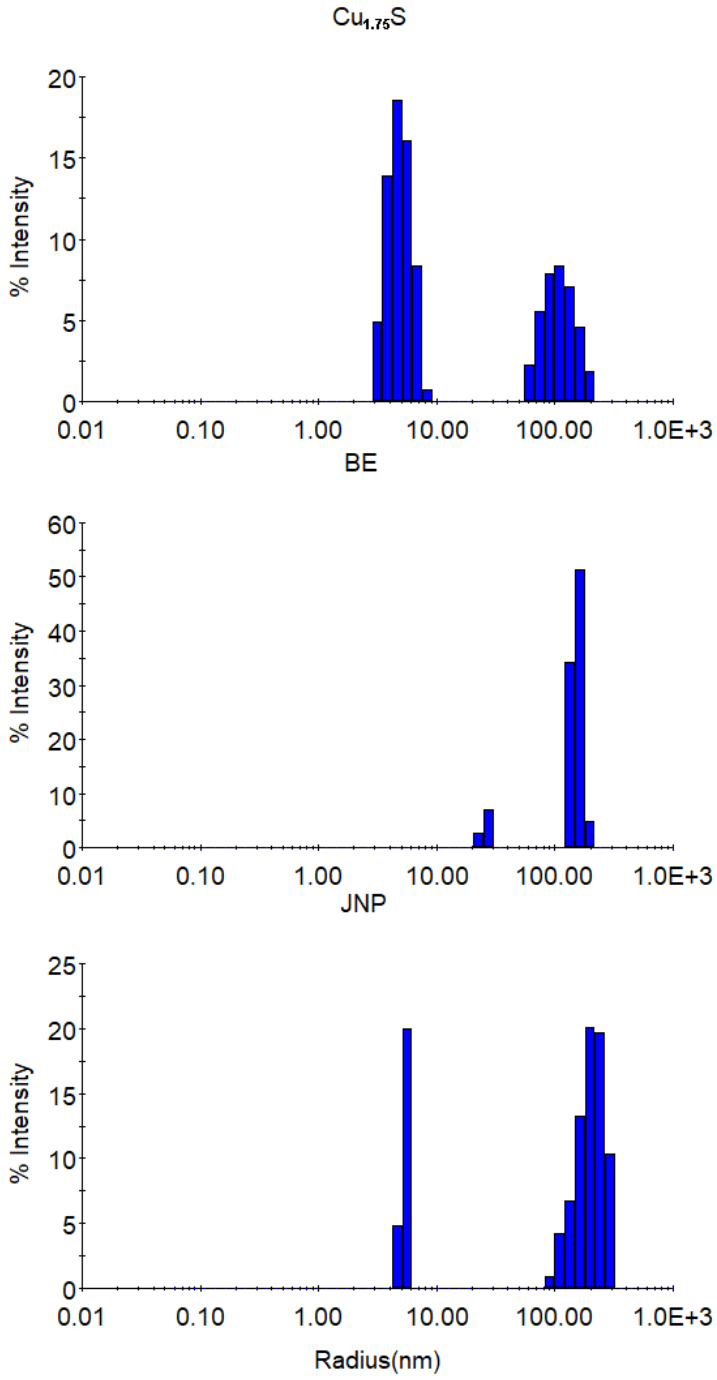

Figure 5.7. DLS measurements of $Cu_{1.75}S$, BE and JNP in $CHCl_3$.

NIR spectra show that the as prepared $Cu_{1.75}S$ nanocrystal exhibit a broad absorption peak at 1410 nm, which is attributed to the in-plane longitudinal LSPR absorption mode (**Fig. 5.4b**) [17]. This absorption peak can be correlated to the free hole density within the structure, where the intensity of this absorption peak decreases and red-shifts due to the decreased number of free carrier density within the structure caused by the increased number of Cu ions as the Cu to S ratio increases from $Cu_{1.1}S$ to Cu_2S. The JNP sample exhibited an LSPR absorption peak at 1300 nm, blue shifted from 1410 nm where $Cu_{1.75}S$ absorbs. This blue shift of absorption peak for the $Cu_{1.75}S$-Au hybrid material can be attributed to the change in the overall nanoparticle composition and aspect ratio change of the nanoparticle, which is consistent with previous finding with a blue shift of λ_{max} for 100 nm [26]. For the BE sample, the disappearance of LSPR absorption in the NIR region can be due to either the aggregation of nanoparticles or the surface property changed by the large amount of gold deposition.

Chirality of nanoparticles can be originated from either its chiral metallic core or upon interaction with chiral ligands on its surface [8]. Upon deposition of gold onto the one side of $Cu_{1.75}S$ nanostructure, the surface electronic distribution of JNP becomes uneven, thus broken the symmetry of the original structure. In studying the chirality upon formation of $Cu_{1.75}S$-Au hybrid structure, CD measurements were carried out in $CHCl_3$ (**Fig. 5.4c**). Both $Cu_{1.75}S$ and BE samples do not show any PCD signal, while JNP shows a positive PCD signal at 600 nm, despite there is no SPR absorption shown in the UV-vis spectrum due to the low concentration of gold presented in the overall structure. Previous studies shown that concentration may cause shifting of CD peak

position and the symmetry of cotton effect (e.g. only showing positive / negative response or uneven positive / negative response) due to inter-particle interactions in solution [33]. DLS measurement shows a hydrodynamic radius of JNP for 18.1 nm, indicating JNP sample is highly disperse in chloroform, meaning the red-shift of CD signal was not attributed to aggregation of JNP or the coupling of neighboring nanoparticles. In addition, the fact that the chiral response is at 600nm mainly attributed to the structure of deposited gold is more like a semi-sphere, instead of spherical nanoparticle. Figure 5.6 displays UV-vis absorption profile of spherical AuC6 and its corresponding CD spectrum, indicating no chiroptical response of spherical gold nanoparticles at its SPR absorption region. Since the LSPR absorption of nanoparticle is heavily depended on its shape, the aspect ratio of 1.66 ± 0.29 nm for deposited gold may red-shift its LSPR absorption peak to 600 nm.

Previously, chiral studies using nanoparticle dimers with two different components show chiroptical response arise in SPR absorption region of both materials [13]. In contrast, the JNP sample synthesized in this study only show chiroptical response in the gold SPR absorption region. In studying the origin of chiroptical response in JNP, the JNP sample was then modify through a selective etching process to remove copper sulfide from the gold component following a previous established method [25]. TEM image of etched JNP sample (**Fig. 5.8a**) shows a triangular cone-like structure with lattice spacing of 2.35 Å, indicating gold (111) facet was isolated from the copper sulfide component. In order to compare the optical profile and chiroptical response of the two samples with the same amount of gold component, the samples were prepared

at the concentration of 0.15 mg / mL un-etched nanoparticles. In comparison to the broad absorption profile of JNP samples throughout the visible region (**Fig. 5.8b**, black), the etched sample shows a very weak absorption peak around 600 nm (red). CD response (**Fig. 5.8c**) shows etched sample has weak chiroptical response around 600 nm (red), due to the asymmetrical shape of the etched gold nanostructure. However, in comparison to the chiroptical response of JNP sample (black), the chiroptical response shown in the etched sample is much weaker. This is a strong indication of the Janus structure can enhance the chiroptical response due to the uneven electronic distribution between the segregated copper sulfide and gold components.

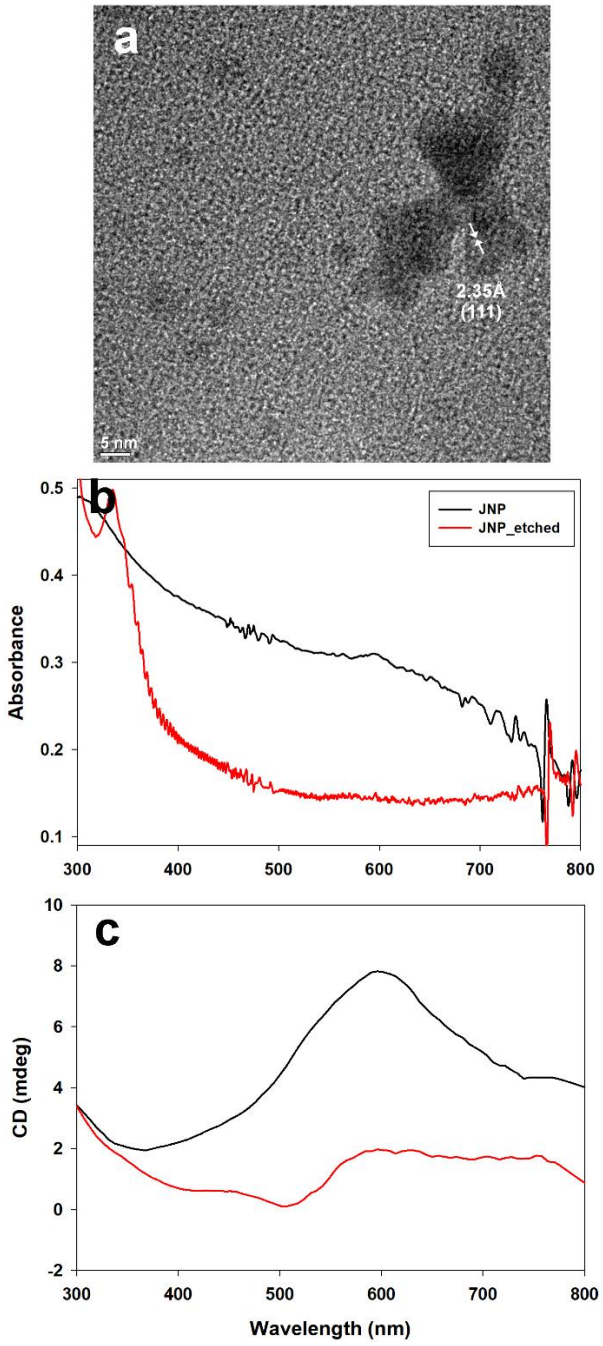

Figure 5.8. TEM image of etched JNP (a), and the UV-vis (b) and CD (c) absorption spectra of JNP (black) and etched JNP (red) sample at the concentration of 0.15 mg / mL (before etching concentration) in $CHCl_3$.

5.5 Conclusion

Janus $Cu_{1.75}S$-Au hybrid nanostructures were synthesized using LB method at room temperature. A positive chiroptical response of JNP sample was arose between 600 – 800 nm, within the SPR absorption region of copper and gold. In comparison to the bulk exchange nanoparticles and as-prepared $Cu_{1.75}S$ showing no chiroptical response, the chiroptical response can be originated either from the Janus structure or the chiral deposition of gold atoms. Thus, by chemical etching of $Cu_{1.75}S$, the remaining gold nanostructure showed weak positive chiroptical response further confirms that the origin of chirality for the Janus hybrid was coming from the asymmetrical deposition of Au atoms. In addition, the formation of such hybrid structure increased the uneven distribution of electrons within the structure; thus, enhanced the chiroptical response of the asymmetrically grew gold nanostructure.

5.6 References

(1) Valev, V. K.; Baumberg, J. J.; Sibilia, C.; Verbiest, T. Chirality and Chiroptical Effects in Plasmonic Nanostructures: Fundamentals, Recent Progress, and Outlook. *Adv Mater* **2013**, *25*, 2517-2534.

(2) Polavarapu, L.; Perez-Juste, J.; Xu, Q. H.; Liz-Marzan, L. M. Optical sensing of biological, chemical and ionic species through aggregation of plasmonic nanoparticles. *J Mater Chem C* **2014**, *2*, 7460-7476.

(3) Wattanakit, C.; Saint Come, Y. B.; Lapeyre, V.; Bopp, P. A.; Heim, M.; Yadnum, S.; Nokbin, S.; Warakulwit, C.; Limtrakul, J.; Kuhn, A. Enantioselective recognition at mesoporous chiral metal surfaces. *Nat Commun* **2014**, *5*.

(4) Zhu, F.; Li, X. Y.; Li, Y. C.; Yan, M.; Liu, S. Q. Enantioselective Circular Dichroism Sensing of Cysteine and Glutathione with Gold Nanorods. *Anal Chem* **2015**, *87*, 357-361.

(5) Wei, J. J.; Guo, Y. J.; Li, J. Z.; Yuan, M. K.; Long, T. F.; Liu, Z. D. Optically Active Ultrafine Au-Ag Alloy Nanoparticles Used for Colorimetric Chiral Recognition and Circular Dichroism Sensing of Enantiomers. *Anal Chem* **2017**, *89*, 9781-9787.

(6) Ghosh, S. K.; Pal, T. Interparticle coupling effect on the surface plasmon resonance of gold nanoparticles: from theory to applications. *Chem Rev* **2007**, *107*, 4797-4862.

(7) Noguez, C. Surface Plasmons on Metal Nanoparticles: The Influence of Shape and Physical Environment. *J Phys Chem C* **2007**, *111*, 3806-3819.

(8) Ma, W.; Xu, L. G.; de Moura, A. F.; Wu, X. L.; Kuang, H.; Xu, C. L.; Kotov, N. A. Chiral Inorganic Nanostructures. *Chemical Reviews* **2017**, *117*, 8041-8093.

(9) Wang, P. P.; Yu, S. J.; Govorov, A. O.; Ouyang, M. Cooperative expression of atomic chirality in inorganic nanostructures. *Nat Commun* **2017**, *8*, 14312.

(10) Lee, H. E.; Ahn, H. Y.; Mun, J.; Lee, Y. Y.; Kim, M.; Cho, N. H.; Chang, K.; Kim, W. S.; Rho, J.; Nam, K. T. Amino-acid- and peptide-directed synthesis of chiral plasmonic gold nanoparticles. *Nature* **2018**, *556*, 360-365.

(11) Mark, A. G.; Gibbs, J. G.; Lee, T.-C.; Fischer, P. Hybrid nanocolloids with programmed three-dimensional shape and material composition. *Nature Materials* **2013**, *12*, 802.

(12) Govorov, A. O. Plasmon-Induced Circular Dichroism of a Chiral Molecule in the Vicinity of Metal Nanocrystals. Application to Various Geometries. *The Journal of Physical Chemistry C* **2011**, *115*, 7914-7923.

(13) Besteiro, L. V.; Zhang, H.; Plain, J.; Markovich, G.; Wang, Z. M.; Govorov, A. O. Aluminum Nanoparticles with Hot Spots for Plasmon-Induced Circular Dichroism of Chiral Molecules in the UV Spectral Interval. *Adv Opt Mater* **2017**, *5*.

(14) Yao, H.; Kobayashi, R. Chiral monolayer-protected Au-Pd bimetallic nanoclusters: Effect of palladium doping on their chiroptical responses. *J Colloid Interf Sci* **2014**, *419*, 1-8.

(15) Sun, S. D.; Li, P. J.; Liang, S. H.; Yang, Z. M. Diversified copper sulfide (Cu2-xS) micro-/nanostructures: a comprehensive review on synthesis, modifications and applications. *Nanoscale* **2017**, *9*, 11357-11404.

(16) Morales-Garcia, A.; Soares, A. L.; Dos Santos, E. C.; de Abreu, H. A.; Duarte, H. A. First-Principles Calculations and Electron Density Topological Analysis of Covellite (CuS). *J Phys Chem A* **2014**, *118*, 5823-5831.

(17) Xie, Y.; Riedinger, A.; Prato, M.; Casu, A.; Genovese, A.; Guardia, P.; Sottini, S.; Sangregorio, C.; Miszta, K.; Ghosh, S.; Pellegrino, T.; Manna, L. Copper Sulfide Nanocrystals with Tunable Composition by Reduction of Covellite Nanocrystals with Cu+ Ions. *Journal of the American Chemical Society* **2013**, *135*, 17630-17637.

(18) Goel, S.; Chen, F.; Cai, W. B. Synthesis and Biomedical Applications of Copper Sulfide Nanoparticles: From Sensors to Theranostics. *Small* **2014**, *10*, 631-645.

(19) Motl, N. E.; Bondi, J. F.; Schaak, R. E. Synthesis of Colloidal Au-Cu2S Heterodimers via Chemically Triggered Phase Segregation of AuCu Nanoparticles. *Chem Mater* **2012**, *24*, 1552-1554.

(20) Vinokurov, K.; Macdonald, J. E.; Banin, U. Structures and Mechanisms in the Growth of Hybrid Ru-Cu2S Nanoparticles: From Cages to Nanonets. *Chem Mater* **2012**, *24*, 1822-1827.

(21) Ding, X. G.; Zou, Y.; Ye, F.; Yang, J.; Jiang, J. Pt-CuS heterodimers by sulfidation of CuPt alloy nanoparticles and their selective catalytic activity toward methanol oxidation. *J Mater Chem A* **2013**, *1*, 11880-11886.

(22) Li, Y. J.; Ding, W. C.; Li, M. R.; Xia, H. B.; Wang, D. Y.; Tao, X. T. Synthesis of core-shell Au-Pt nanodendrites with high catalytic performance via overgrowth of platinum on in situ gold nanoparticles. *J Mater Chem A* **2015**, *3*, 368-376.

(23) Basu, M.; Nazir, R.; Fageria, P.; Pande, S. Construction of CuS/Au Heterostructure through a Simple Photoreduction Route for Enhanced Electrochemical Hydrogen Evolution and Photocatalysis. *Sci Rep-Uk* **2016**, *6*.

(24) Wang, Y.; Hu, Y. X.; Zhang, Q.; Ge, J. P.; Lu, Z. D.; Hou, Y. B.; Yin, Y. D. One-Pot Synthesis and Optical Property of Copper(I) Sulfide Nanodisks. *Inorg Chem* **2010**, *49*, 6601-6608.

(25) Nelson, A.; Ha, D.-H.; Robinson, R. D. Selective Etching of Copper Sulfide Nanoparticles and Heterostructures through Sulfur Abstraction: Phase Transformations and Optical Properties. *Chemistry of Materials* **2016**, *28*, 8530-8541.

(26) Ding, X.; Liow, C. H.; Zhang, M.; Huang, R.; Li, C.; Shen, H.; Liu, M.; Zou, Y.; Gao, N.; Zhang, Z.; Li, Y.; Wang, Q.; Li, S.; Jiang, J. Surface Plasmon Resonance Enhanced Light Absorption and Photothermal Therapy in the Second Near-Infrared Window. *Journal of the American Chemical Society* **2014**, *136*, 15684-15693.

(27) Kubel, C.; Voigt, A.; Schoenmakers, R.; Otten, M.; Su, D.; Lee, T. C.; Carlsson, A.; Bradley, J. Recent advances in electron tomography: TEM and HAADF-STEM tomography for materials science and semiconductor applications. *Microsc Microanal* **2005**, *11*, 378-400.

(28) Tang, A. W.; Qu, S. C.; Li, K.; Hou, Y. B.; Teng, F.; Cao, J.; Wang, Y. S.; Wang, Z. G. One-pot synthesis and self-assembly of colloidal copper(I) sulfide nanocrystals. *Nanotechnology* **2010**, *21*.

(29) Krylova, V.; Andrulevicius, M. Optical, XPS and XRD Studies of Semiconducting Copper Sulfide Layers on a Polyamide Film. *Int J Photoenergy* **2009**.

(30) Ye, M. D.; Wen, X. R.; Zhang, N.; Guo, W. X.; Liu, X. Y.; Lin, C. J. In situ growth of CuS and Cu1.8S nanosheet arrays as efficient counter electrodes for quantum dot-sensitized solar cells. *J Mater Chem A* **2015**, *3*, 9595-9600.

(31) Liu, M. Y.; Zhou, W.; Wang, T.; Wang, D. F.; Liu, L. Q.; Ye, J. H. High performance Au-Cu alloy for enhanced visible-light water splitting driven by coinage metals. *Chem Commun* **2016**, *52*, 4694-4697.

(32) Liu, Y.; Liu, M. X.; Swihart, M. T. Reversible Crystal Phase Interconversion between Covellite CuS and High Chalcocite Cu2S Nanocrystals. *Chem Mater* **2017**, *29*, 4783-4791.

(33) Castiglioni, E.; Abbate, S.; Longhi, G.; Gangemi, R. Wavelength shifts in solid-state circular dichroism spectra: a possible explanation. *Chirality* **2007**, *19*, 491-496.